WISSENSCHAFTLICHE ARBEITEN DER FACHRICHTUNG
GEODÄSIE UND GEOINFORMATIK DER LEIBNIZ UNIVERSITÄT HANNOVER
ISSN 0174-1454

Nr. 307

M.Sc. Muhamad Nasir A. ALRAJHI

A Semi-Automated Procedure for Orthophoto Generation from High Resolution Satellite Imagery

HANNOVER 2013

WISSENSCHAFTLICHE ARBEITEN DER FACHRICHTUNG
GEODÄSIE UND GEOINFORMATIK DER LEIBNIZ UNIVERSITÄT HANNOVER
ISSN 0174-1454

Nr. 307

M.Sc. Muhamad Nasir A. ALRAJHI

A Semi-Automated Procedure for Orthophoto Generation from High Resolution Satellite Imagery

Von der Fakultät für Bauingenieurwesen und Geodäsie
der Gottfried Wilhelm Leibniz Universität Hannover
zur Erlangung des Grades

DOKTOR-INGENIEUR (Dr.-Ing.)

genehmigte Dissertation
von

M.Sc. Muhamad Nasir A. ALRAJHI

geboren am 08.12.1961 in Riyadh, Kingdom of Saudi Arabia

HANNOVER 2013

Vorsitzender der Prüfungskommission: Univ.- Prof. Dr.-Ing. Winrich Voß

Referent: Univ.-Prof. Dr.-Ing. habil. Christian Heipke
Korreferenten: Univ.-Prof. Dr.-Ing. habil. Monika Sester
Prof. Dr. Mushtaq Hussain, California State University, Fresno, USA

Tag der Promotion: 24. Mai 2013

Abstract:

The General Directorate of Surveying and Mapping (GDSM), under the Ministry of Municipal and Rural Affairs (MOMRA) is responsible for the production, maintenance and delivery of accurate geospatial data for all the metropolitan cities, towns and rural settlements in the Kingdom of Saudi Arabia. In order to support all planning and development activities at the national, regional and local municipality level, GDSM maintains digital geodatabases that support the production of conventional line and Orthophoto maps at scales ranging from 1:1,000 to 1:20,000.

The key role that the geospatial information plays in the planning and the development processes essentially demands currency of the information. The fast pace of urbanization is continually resulting in rapid development of physical infrastructure, high rate of growth and fast changes in urban and rural areas. This poses a major challenge to GDSM in maintaining currency in the geospatial data. The current procedures used for awarding and implementing the contracts for the acquisition of new aerial imagery and control it by carrying out new geodetic field surveys and the subsequent photogrammetric data processing and mapping covers a long time cycle of 3 or more years. Consequently, the availability of recently acquired High Resolution Satellite Imagery (HRSI) presents an attractive alternative image data resource for rapidly responding to updated geospatial data needs.

It is well known that a satellite image when orthoprojected using the vendor-provided Rational Polynomial Function (RPC) data often displays X- and Y-coordinate biases of several pixels, even when corrected for terrain. Therefore, a large number of ground surveyed control points are required to achieve a pixel-level georeferencing accuracy. The collection of control data in the field and the measurement of the control points in the satellite images takes time, requires skilled labour and is costly. The primary objective of this research, therefore, is to use existing image and data base information instead of traditional ground control for the orthoprojection process in order to automate and speed up as much as possible the whole process.

The existing 50-cm GSD aerial orthophoto database has been selected to serve as control data for georeferencing of a large set of HRSI that included 50-cm GSD (ground sampling distance) GeoEye-1, 1-m GSD IKONOS-2 and 2.5-m GSD SPOT-5 images. The test satellite imagery covers three different test areas representing urban, agricultural and rural landscape. Based on a series of practical experiments, the ability for automated matching of aerial and satellite images by using the Speeded-Up Robust Features (SURF) algorithm has been demonstrated. The practical results from matching with SURF validate the ability for multi-scale, multi-sensor and multi-season matching of aerial and satellite images. The matched tie points are then used to transform the satellite orthoimage to the aerial orthoimage through a 2D Affine coordinate transformation. The GeoEye-1 and the IKONOS-2 imagery, when georeferenced through SURF-based matching and transformed, meets the MOMRA Map Accuracy Standards for 1:10,000 scale. However, a similarly processed SPOT-5 image does not meet the standards for 1:10,000 scale mapping.

This research has led to the development of a simple and efficient tool for the georeferencing of HRSI of 50-cm to 1-m GSD that can be used for updating map information that meets MOMRA accuracy standards for 1:10,000 scale mapping. The process completely eliminates the need for any ground control as well as image measurements by a skilled operator. About 5 to 7 satellite images can routinely be processed on a workstation in a single day; a rate well-suited for a map production organization. The implementation of this tool in MOMRA practice will greatly enhance its ability to quickly respond to urgent needs for updated map data.

Keywords: Orthophotos, Satellite Imagery, HRSI, Automated image matching

Zusammenfassung:

Das General Directorate of Surveying and Mapping (GDSM) als Teil des Ministeriums für Municipal and Rural Affairs (MOMRA) ist für die Produktion, Pflege und Bereitstellung von genauen Geodaten für alle Metropolregionen, Städte und ländlichen Siedlungen des Königreichs Saudi Arabien zuständig. Damit alle Planungen und Entwicklungsaktivitäten auf nationalen, regionalen und allen lokalen Stadtbereichen unterstützt werden können, unterhält das GDSM digitale Geodatenbasen, die die Produktion konventioneller Vektordaten und Orthobildkarten in den Maßstäben 1:1.000 bis 1:20.000 ermöglichen.

Die Schlüsselrolle die die räumlichen Information in den Planungs- und Entwicklungsprozessen spielt, wirkt sich wesentlich auf die erforderliche Aktualität der Daten aus. Die enorme Verstädterung führt zu einer schnellen Entwicklung der Infrastruktur, einem hohen Wachstum sowie rapiden Änderungen im urbanen und ländlichen Bereich. Die derzeitigen Verfahren zur Vergabe und den Abschluss von Verträgen für neue Bildflüge und die dazugehörigen Passpunktbestimmungen mit ihren örtlichen Vermessungen, sowie die photogrammetrische Auswertung und Kartenerstellung nehmen drei Jahre und mehr in Anspruch. Die Verfügbarkeit aktueller hochauflösender Satellitenbilder stellt eine attraktive Alternative für eine schnelle, erforderliche Fortführung der Geodaten dar.

Orthobilder aus Satellitenbildern, die nur auf der direkten Sensororientierung basieren, die als rationale Polynomkoeffizienten zusammen mit den Bilddaten geliefert werden, können Abweichungen von vielen Pixeln aufweisen. Deswegen sind etliche Passpunkte erforderlich um eine Genauigkeit im Pixelbereich zu erreichen. Die örtliche Bestimmung von Passpunkten ist zeitaufwändig. Das Hauptziel dieser Untersuchungen besteht darin, vorhandene Orthobilder und Basisinformationen anstelle traditioneller Passpunktbestimmungen für die Erstellung aktueller Orthobilder zu verwenden, um den ganzen Prozess durch Automatisierung zu beschleunigen.

Vorhandene Orthobilder mit 50cm Objektpixelgröße (englisch ground sampling distance (GSD)) wurden als Georeferenzinformation für hochauflösende Satellitenbilder von GeoEye-1 mit 50cm GSD, IKONOS mit 1m GSD und SPOT-5 mit 2,5m GSD genutzt. Die verwendeten Testbilder erfassen städtische, landwirtschaftliche und ländliche Bereiche. Basierend auf einer Reihe praktischer Untersuchungen wurde die Eignung des „Speeded-Up Robust Features (SURF)“ Algorithmus zur automatischen Zuordnung von Luft- und Satellitenbildern gezeigt. Die praktischen Ergebnisse der Bildzuordnung mit SURF wurden mit unterschiedlichen Maßstäben und verschiedenen Sensorbildern aus voneinander abweichenden Jahreszeiten überprüft. Die zugeordneten Verknüpfungspunkte wurden benutzt, um die orthorektifizierten Satellitenbilder mittels zweidimensionaler Affintransformation auf die Luftbild-Orthobilder zu beziehen. Die so mittels SURF georeferenzierten GeoEye-1 und IKONOS-Bilder erfüllen die Genauigkeitsstandards von MOMRA für den Maßstab 1:10 000. Dagegen konnten mit den niedriger aufgelösten SPOT-5 Bildern diese Genauigkeitsanforderungen nicht erfüllt werden.

Die Untersuchungen haben zu einem einfachen und effizienten Verfahren für die Georeferenzierung hochaufgelöster Satellitenbilder mit 50cm und 1m GSD geführt, das für die Fortführung der Karteninformationen benutzt werden kann und die Genauigkeitsanforderungen von MOMRA für den Maßstab 1:10 000 erfüllt. Dieses Verfahren ersetzt vollständig die örtliche Passpunktbestimmung und die manuelle Bildmessung durch erfahrene Auswerter. Etwa 5 bis 7 Satellitenbilder können so innerhalb eines Tages orientiert werden, was für die Kartenproduktion zufriedenstellend ist. Die Implementierung des Verfahrens bei MOMRA wird die Möglichkeit zur schnellen Reaktion auf Anforderungen zu aktuellen Kartendaten erheblich verbessern.

Stichworte: Orthophotos , Satellitendaten, hochauflösenden Satellitendaten ,Bildzuordnung

Table of contents:

Chapter 1. Motivation and Objectives

Up-to-date geospatial data play a dynamic key role in decision making, planning and development. Lack of current information on maps has always troubled users. The most essential need is to provide timely supplements to maps to keep the data up-to-date. Rapid development of infrastructure, high rate of growth and fast changes in urban and rural areas are the major challenge to maintain currency in the large volume of the national geospatial information base, which poses a challenge to explore alternative solutions for economical, accurate and rapid procedures for map updating.

1.1 Introduction

The Kingdom of Saudi Arabia covers an area of approximately 2 million km^2, within this area there are 220 municipalities with about 6 million land parcels. Different agencies like the Military Surveying Department, the Ministry of Municipal and Rural Affairs (MOMRA) and the Saudi Geological Survey are responsible for producing the geospatial information. MOMRA has the official mandate for large scale urban mapping and is committed to provide precise, accurate, up-to-date and standardized geospatial data to the users. In fulfilling this mandate, the most challenging task is to provide kingdom wide up-to-date spatial information of rapidly growing urban and rural areas. As a case study the Kingdom of Saudi Arabia presents an ideal example which can provide enough study material to analyze and develop general map updating procedures, which can be used globally.

1.1.1 Topographic Mapping in KSA

The Kingdom of Saudi Arabia has been covered by small and large scale topographic mapping using photogrammetric procedures. In 1950 the Ministry of Petroleum initiated topographic mapping of the entire kingdom at the 1:50,000 scale. Unlike classical triangulation, the geodetic reference at that time was established by traverses using newly introduced electronic distance measurement technology. The resulting network of 700 monumented geodetic stations was adequate to meet the required accuracy for national mapping at the scale of 1: 50,000, but is not suited for mapping at larger scales needed for urbanized and settlement areas.

In 1960 the responsibility of preparing 1: 50,000 scale map sheets were transferred to the Military Surveying Department of the Ministry of Defense and Aviation. This department is also responsible for local 1:25,000 and smaller scale mapping, while the Saudi Geological Survey has been assigned the mandate for geological map production. The large scale urban mapping effort was assigned to MOMRA for which it had to develop a new Geodetic Network that could satisfy large scale mapping requirements. This resulted in the establishment of a modern GPS based geodetic reference frame that forms the MOMRA Geodetic Datum 2000 (MGD-2000).The MGD-2000 is based on ITRF-2000, Epoch 2004.0 and uses the GRS80 Ellipsoid. In step with the establishment of the new Geodetic Datum, the older vertical datum established for 1:50,000 scale mapping was also strengthened through additional differential leveling resulting in the MOMRA Vertical Datum2008 (MVD-2008).This currently provides a more accurate estimate for geoidal heights than Geoid 2008 for most of the mapped coverage of the Kingdom of Saudi Arabia.

1.1.2 Large Scale Topographic Mapping

Latest photogrammetric technologies have been implemented to meet kingdom wide mapping requirements and to maintain the large scale topographic map database. By a series of aerial survey projects, up to 25,000 km^2 of the settled areas of the country have been covered by 1:5,500 scale aerial photographs, and up to 300,000 km^2 area has been covered by 1:45,000 scale aerial photographs. A large part of the mountainous area has been covered with 1:22,500 scale

aerial photography. Using current photogrammetric technology and methods, high quality topographic maps at 1:1,000, 1:2,500, 1:10,000 and 1:20,000 scales have been produced (Alrajhi and Hawarey, 2008). Figure 1-1 to Figure 1-4 shows representative samples of photogrammetric mapping at different scales. Figure 1-5 shows the current map coverage with related statistics provided in Table 1-1. For reference, the Map Accuracy Standards currently followed in MOMRA are also given in Table 1-2. Currently; more than 365 features are being captured using soft copy stereo data compilation procedures. Such aerial survey, line mapping and geodatabase compilation projects take from 2 to 3 years to complete, and in the meanwhile, significant changes in the urban infrastructure are taking place. The usual impact of such rapidly occurring changes is that although the geodata are spatially precise and accurate, they often do not reflect the current status of land on the map.

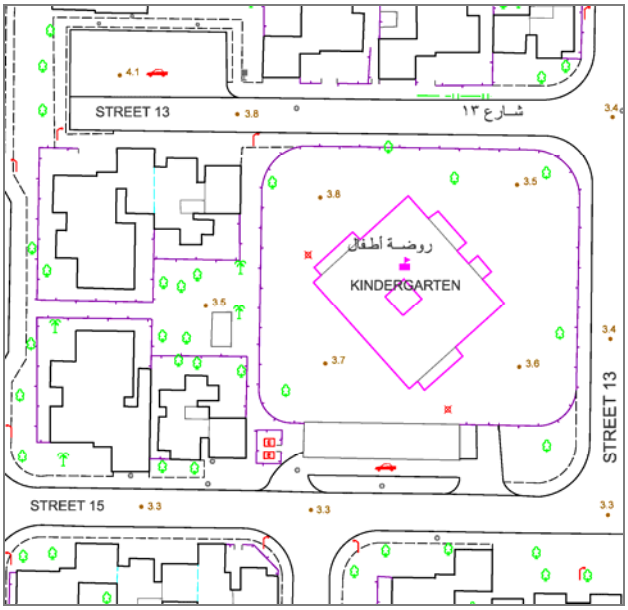

Figure 1-1: 1:1,000 Scale Map

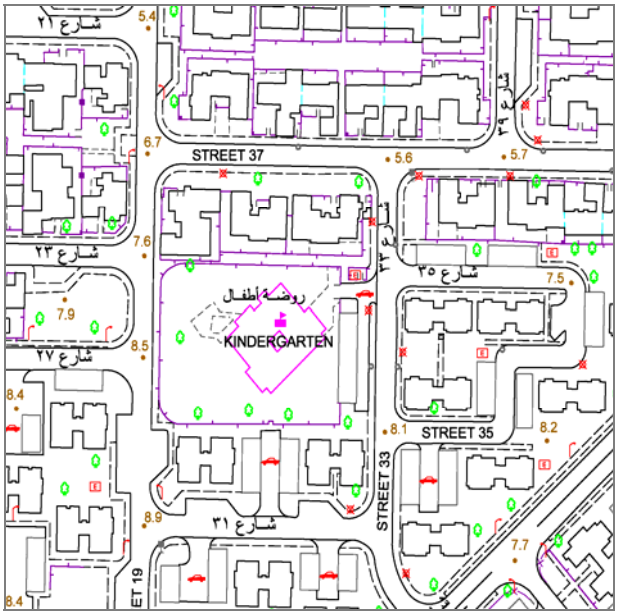

Figure 1-2: 1:2,500 Scale Map

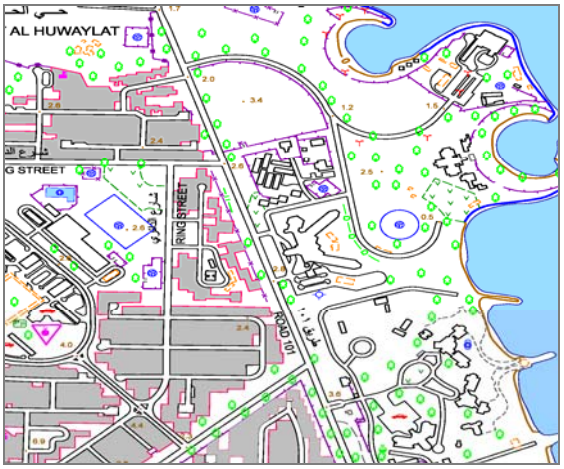

Figure 1-3: 1:10,000 Scale Map

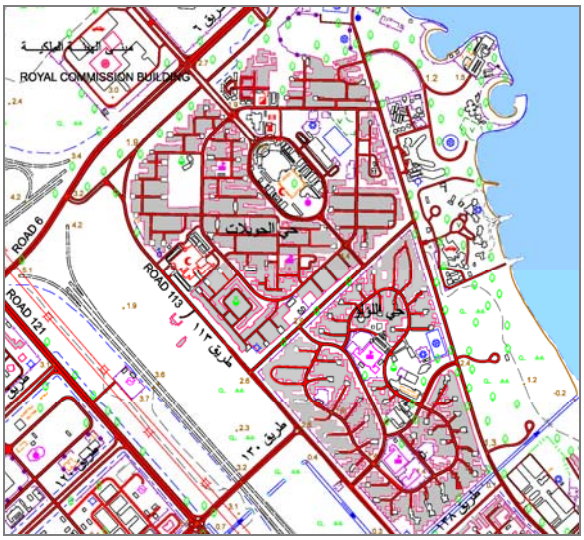

Figure 1-4: 1:20,000 Scale Map

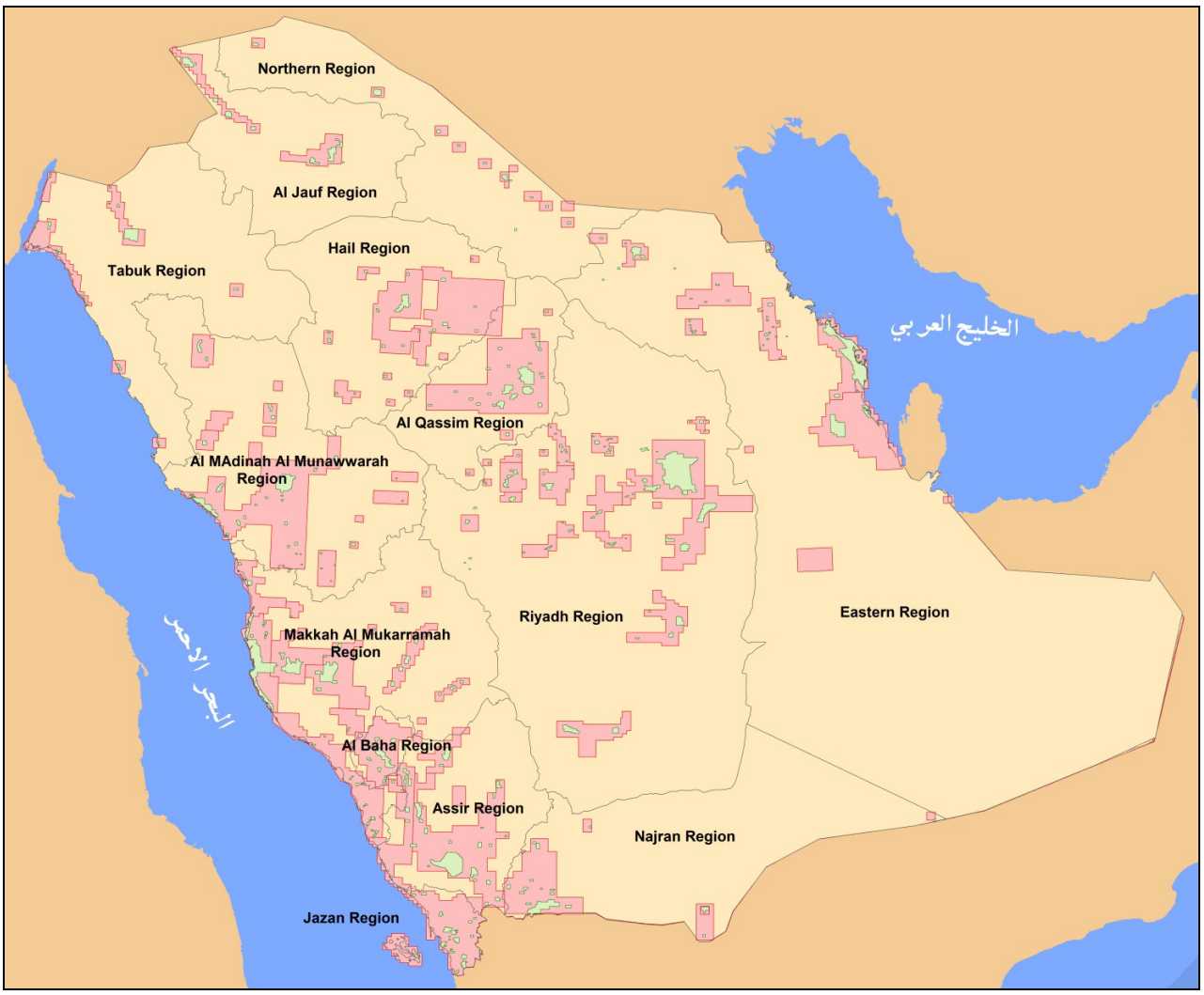

Figure 1-5: Large Scale Mapping Coverage in the Kingdom

1:5,500 scale Aerial Photography Coverage (1:1,000 and 1:2,500 scale mapping)

1:45,000 scale Aerial Photography Coverage (1:10,000 and 1:20,000 scale mapping)

Aerial Photography		**Orthophoto Generation**		**3D Mapping and Geodatabase**	
Scale	**Area** [km^2]	**Scale**	**Area** [km^2]	**Scale**	**Area** [km^2]
1:5,500	40,000	1:1,000	22,000	1:1,000	24,000
		1:2,500	25,000	1:2,500	25,000
1:22,500	8,000	1:5,000	8,000	-	-
1:45,000	320,000	1:10,000	175,000	1:10,000	241,000
		1:20,000	300,000	1:20,000	307,000

Table 1-1: Spatial data statistics for large scale mapping series

Map Scale for Photogrammetric Data Compilation	Positional Error (m)		Height Error (m) (1-σ level)
	Northing (1-σ level)	Easting (1-σ level)	
1:1,000	0.15	0.15	0.30
1:2,500	0.35	0.35	0.50
1:5,000	0.60	0.60	0.75
1:10,000	1.25	1.25	1.50
1:20,000	2.50	2.50	3.00

Table 1-2: MOMRA Map Accuracy Standards

1.2 Defining the Problem

1.2.1 Need of Rapid Map Updating

Growth in population, rapid industrialization and migration from remote areas to cities cause the urban areas to grow at a much faster rate than the corresponding growth in population. This is the main cause of the urban sprawl illustrated in Figure 1-6 to Figure 1-10.

Figure 1-6:Temporal data depicting change (2007 orthophoto left; 2012 satellite image, right)

Rapid changes are constantly going on in utilities, structures, building and transportation facilities which need to be reflected in the map database. Therefore, the existing large scale topographic base maps at the different scales 1:1,000, 1:2,500, 1:10,000 and 1:20,000 need to be frequently updated. The current procedure for awarding and implementing the contracts for the acquisition of new aerial imagery and controlling it through new geodetic surveys and subsequent photogrammetric data processing and map compilation covers a long time cycle of three or more years. This approach is both very slow and costly for frequent revision in map database while new changes are constantly going on. Consequently, alternative technologies must be explored.

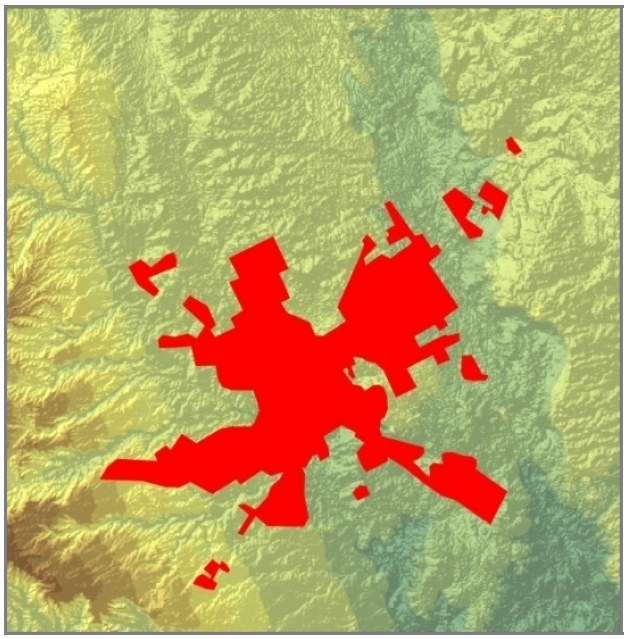

Figure 1-7: Riyadh 1980 (400 km2)

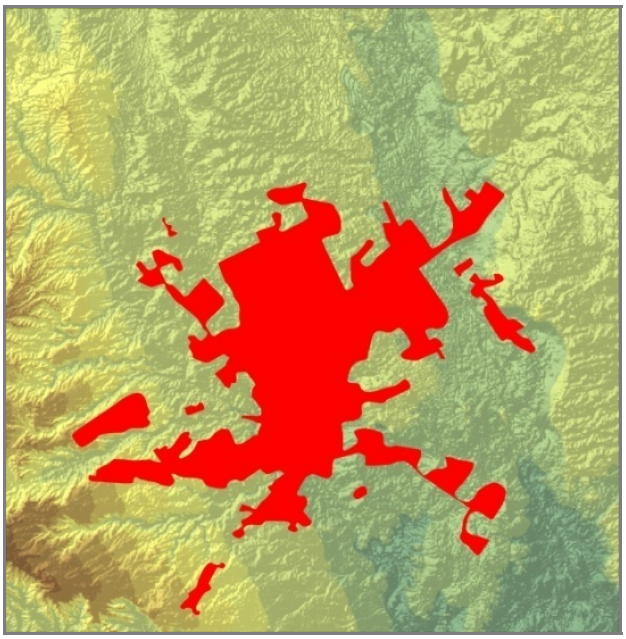

Figure 1-8: Riyadh 1990 (650 km^2)

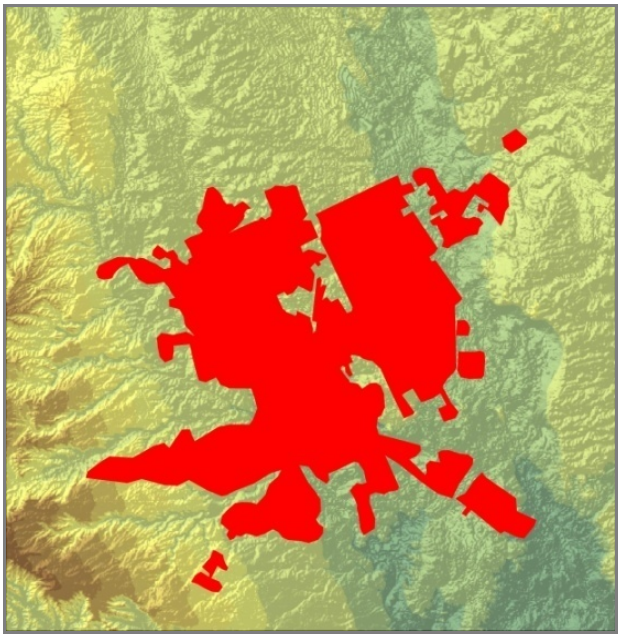

Figure 1-9: Riyadh 2000 (725 km^2)

Figure 1-10: Riyadh 2010 (1,000 km^2)

1.2.2 Need for Cadastral Parcel Fabric

A parcel fabric must be prepared before initiating cadastral surveys of any area. Precisely geopositioned cadastral base maps, such as the one illustrated in Figure 1-11 having the detailed information about the cadastral units, their graphical representation, their neighborhood information, their unique identification codes and their associated attributes are required for pre-survey planning and associated works, which can then serve as the foundation for establishing a Kingdom wide cadastral system. However, production of preliminary parcel maps through conventional photogrammetric methods would require several decades which is not practical.

Figure 1-11: Cadastral Basemap

1.3 Alternate Solutions for the problem

If the existing topographic maps of an area are more than a decade old and updated large scale maps are needed for engineering planning and design, the most logical choice would be to carry out new photogrammetric mapping of the area based on new aerial imagery. However, if the existing topographic maps are not very old and only about 10 to 15 percent of the features have changed, then it would be uneconomical, and also time consuming, to map the entire area through new aerial imagery coverage. In such a case, an alternate methodology that allows the incorporation of only the changes to the existing map database would be faster and, consequently, more economical. With this in mind, the following alternatives may be considered.

1.3.1 GNSS Based Terrestrial Mapping

Terrestrial surveying using the conventional plane surveying principles has been the usual approach to perform engineering surveys where the extent of the area to be surveyed is small such as a land subdivision. The advent of the Global Navigation Satellite System (GNSS) surveying techniques has eliminated the significant constraint for the line-of-sight requirement in land surveying. Consequently, the GNSS surveying procedures have now almost completely replaced the tacheometric procedures that were common in the past. Due to the establishment of a nationwide Continuously Operating Reference Stations (CORS) network, often supplemented with Local Area CORS Networks, Real-Time Kinematic (RTK) GNSS surveying is now very widely being used.

Even though the RTK methodology can yield 5-cm level positioning accuracy, the cost of conducting field surveys becomes exorbitantly expensive, especially since even the largest scale engineering mapping at scale 1:500 needs a positioning accuracy only at the 10 to 15 cm level. In addition, the RTK methodology is well suited for use in open areas but in highly urbanized areas, tall buildings create the so-called “urban canyons” that often cause a loss of satellite signals resulting in uncertainty in observed data. Moreover, the usual high density of urban traffic often causes multipath effects; though the carrier phase multipath effect is not serious for mapping accuracies, it may result in loss of weak GNSS signals (Misra and Enge, 2001).

Based on the above considerations, the use of GNSS based terrestrial field surveys to revise and update existing large scale maps is not considered as an economically viable alternative for Saudi Arabia.

1.3.2 Satellite Image Based Mapping

The primary interest was the multi user oriented geological and environmental observation when NASA launched the first multispectral scanner, ERTS-1 (later renamed Landsat-1) in 1972 to image the Earth's surface. The earliest images from ERTS-1 allowed geologists to better understand the geomorphology of the landform through a single image, which could not previously be achieved by aerial photography. More significantly, the Landsat series demonstrated to the world the capability and benefits of repeat coverage imagery from space-borne sensors of benefit to many earth observation disciplines, such as agriculture, forestry, hydrology, land cover, climatology and coastal studies.

Almost 15 years after the launch of Landsat-1, some European governments launched the first SPOT satellite. The SPOT missions were a milestone for earth imaging due to SPOT's unique tilting sensor and cross-track stereoscopic capability. This improved the temporal resolution by allowing more frequent revisit rates which are often required for monitoring land change. While the SPOT sensors today, such as SPOT-5, provide a ground resolution to the order of 2.5 – 10 m, this and similar medium-resolution satellite imagery (MRSI), such as IRS-1C/D and ALOS/PRISM, remain predominantly reserved for classification and thematic mapping used in environmental applications. In terms of cartographic applications, small-scale wide area mapping is feasible at 1:20,000 to 1:25,000 scales; however, there may be inadequate identification of features necessary at such topographic scales. SPOT-5 satellite imagery is reported to be suitable for updating topographic maps at 1:25,000 scale (Tung, 2005).

Continuous advances in satellite sensor technology over the last decade have resulted in meter and sub-meter ground resolution now being commercially obtainable (Dowman et al., 2012). This opens up greater possibilities for mapping at resolutions previously dominated by aerial photography. In 1999, Space Imaging (later GeoEye, now belonging to Digital Globe) launched IKONOS-2, providing civil users with 1-m GSD satellite imagery. Since then several other sensors capable of high resolution imagery have been launched with continuing improvements in sensor technology. Amongst these both GeoEye-1 and DigitalGlobe's WorldView-2 provide 0.5 meter or better GSD imagery, and CNES' Pléiades' two satellites are designed to capture 0.7-m GSD imagery. Pléiades 1A and 1B were launched in December 2011 and 2012, respectively, and have started to provide data.

With the increasing mapping potential of the space-borne imaging sensors, it became customary to regard satellite imagery with GSD from 1-m to 5-m as the High Resolution satellite Imagery (HRSI).With continuing improvement in image resolution, the satellite imagery with sub-meter GSD is sometimes differentiated as Very High resolution satellite Imagery (VHRSI). No such distinction is made in this research study and all satellite imagery with GSD of 5 meter or smaller is labeled as HRSI. The advantage of HRSI over medium-resolution imagery is that more emphasis can be placed on exploiting spatial and contextual attributes with greater usage for metric applications rather than thematic mapping. Shape and texture are better preserved which allows greater recognition, identification and measurement of ground features, as objects are represented over multiple pixels rather than a single pixel. This valuable characteristic enhances the likelihood of highly accurate spatial information products such as image mapping, feature extraction and terrain modeling (Holland et al., 2006; Li and Batchavarova, 2008).

The capability currently provided by different HRSI sensors offers a very promising alternative for large scale map updating. The characteristics and features of some of the HRSI sensors that make them particularly suited for mapping are discussed in the following Chapter.

1.4 Research Needs and Objectives

The primary objective of this research is to devise a methodology for rapid mapping from recent satellite imagery. This is to be achieved by minimizing the need for field surveys for the establishment of control points for orthorectification. Instead, it is proposed to extract such control information from the existing database of aerial orthoimagery. Typically a recent satellite imagery scene may be partially covered with aerial orthoimagery of different spatial resolution derived from aerial photography at different scales. In addition this research aims at finding an optimal solution for mapping from the satellite imagery under these heterogeneous conditions in order to update and/or extend the existing map database or to compile a parcel map.

1.4.1 Need for Additional Research

Based on the review of the current literature, the following conclusions can be drawn.

a) The feasibility of topographic mapping using currently available HRSI has already been clearly demonstrated (Gianinetto, 2008; Holland et al., 2006; Li et al., 2008).
b) Based on a thorough review of the current literature, chapter 3 describes the state-of-the-art methodology and the models used for mapping from HRSI. Evidently, the basic challenge of sensor orientation of HRSI has largely been solved in previous research(Di et al., 2003, Tao et al., 2002; Toutin and Cheng, 2003; Yang, 2000). However, despite successfully demonstrating the geopositioning potential of HRSI using various rigorous and non-rigorous sensor orientation models, the validation of these models has mainly been confined to isolated point positioning. There are no comprehensive accuracy evaluations on the generation of HRSI map products especially at large mapping scales. Consequently, there still exists a need for a systematic and a comprehensive evaluation of the procedures that must be used for processing HRSI in order to routinely and consistently achieve the map accuracy standards in a production environment existing in MOMRA.
c) It has clearly been shown (Eisenbeiss et al., 2004; Fraser and Yamakawa, 2004; Gordecki and Dial, 2003) that GCPs are essentially needed to supplement the vendor provided RPCs during HRSI processing to achieve sub-meter positional accuracy required for mapping at large scales from HRSI. There are some isolated studies (Fraser et al. 2001, Fraser et al. 2002) that attempt to establish some correlation between the number of GCPs and the resulting map accuracy. However, other than the general conclusion that increasing the number of GCPs improves the accuracy, no definitive metric is yet available that relates the number of GCPs and the positional accuracy of the GCPs with the resulting map accuracy. For a map production environment, the number, spatial distribution and the accuracy of the GCPs has to be more clearly specified.
d) There is a wide recognition that the identification of the GCPs on the imagery, from aerial or space platforms, is the most arduous and time consuming step in the georeferencing of imagery. Consequently, some efforts have already been reported for the automated orientation of aerial imagery on database information (e.g. OEEPE Report 36, 1999). However, only one of the three researchers reported success (Läbe, University of Bonn, 1999) in using AMOR (Automatic Model-based Orientation) for processing the aerial imagery test data. Others (Karjalainen and Kuittinen, Finnish Geodetic Institute; Jedryczka, Olsztyn University; Pedersen, Alborg University) reported the use of semi-automated interactive solutions. Consequently, there is a definitive need for seeking additional approaches for automated georeferencing of HRSI.
e) Even though HRSI may be useful for many mapping applications, this research study is restricted to georeferencing, because otherwise the scope of the study would be too large and become unfocussed. The primary aim is to explore semi-automated approach for enhanced mapping productivity.

1.4.2 Adaptation to Needs in Saudi Arabia

Any research findings that are related to the mathematical modeling of the relation between satellite image and the imaged object space are universally applicable without any regard to the geographic location of the imaged scene. Therefore, all the commonly used RPC-based and other geometric models will be fully adaptable for use in this study for processing HRSI covering test areas in Saudi Arabia. However, due to the diversity in the landform and cultural settlement patterns in Saudi Arabia, some of the research findings reported for example, in Germany or Australia, may not be fully applicable to Saudi Arabia. The major differences may be in the ability for image identification and image matching in rural scenes due to lack of texture in desert-like terrain. This will be investigated in this study especially by finding appropriate solutions for semi-automated georeferencing of HRSI.

1.4.3 Semi-Automatic Procedure

Commercial software packages such as Inpho OrthoMaster are available for the orthoprojection of HRSI based on vendor-provided RPC and existing DTM data. They provide very efficient means for HRSI georeferencing through batch processing. Therefore, the proposed methodology represents an effort to automate those additional labour-intensive processes that are needed to optimize the georeferencing accuracy. Accordingly, the proposed methodology is regarded as a "semi-automatic procedure".

1.4.4 Feasibility for Automation for Production

The two distinct processes mainly involved in mapping from HRSI are:

a) The georeferencing of the HRSI to meet the mapping standards.

b) The extraction of cultural features from georeferenced HRSI.

As stated earlier, this study is focused entirely on the first process, viz. the georeferencing of the HRSI to an appropriate level in order to meet the accuracy standard for the intended map scale. Consequently, the first question this research study will seek an answer for is:

Q1: What is the largest scale for mapping from HRSI of 0.5 meter GSD? Also, what is the largest scale for mapping from HRSI of 2.5 meter GSD?

When discussing scale in the context of digital imagery, it should be clear that the relation should really be established between GSD and scale of map output. In this context the choice of HRSI of 0.5 meter and 2.5 meter GSD has been made to cover the most commonly used existing MOMRA mapping scales ranging from 1:1,000 to 1:10,000. It has been generally reported that a "sufficient number" of GCPs are required during processing of HRSI to enhance its georeferencing accuracy (Eisenbeiss et al., 2004). Map production from HRSI as a routine operation essentially requires standardized specifications for the accuracy, number and spatial distribution of GCPs to meet map accuracy standards at different scales. Therefore, in seeking answer to Q1 above, a related question to be explored is:

Q2: What should be the accuracy, number and spatial distribution of GCPs for the largest scale for mapping from HRSI of 0.5 meter GSD? What should be the accuracy, number and spatial distribution of GCPs for the largest scale for mapping from HRSI of 2.5 meter GSD?

The answers to the above Q1 and Q2 will establish the potential for map production or map updating using HRSI. This should lead to the next consideration for enhanced productivity in generating maps from HRSI. The productivity can be greatly increased if the interactive operation of identifying the large number of GCPs on the HRSI can be automated. Accordingly, significant effort in this study will be involved in exploring ways to automate the HRSI georeferencing process. The approach used for georeferencing satellite imagery is briefly described below.

Method for Automated Georeferencing

MOMRA currently has a well-established procedure for the orthoprojection of satellite imagery based on vendor-provided RPC data combined with existing DTM database by using Inpho OrthoMaster software. Although this task can be carried out very efficiently through batch processing, the georeferencing of the resulting orthorectified satellite images is usually coarse and needs to be refined through ground control. Since the MOMRA geodatabase maintains a seamless digital Orthophoto coverage at 1:10,000 scale with 50-cm GSD that has been derived from aerial photography at 1:45,000 scale, it is proposed to use such aerial orthophotos to serve as control. The digital Orthophoto image overlapping the orthorectified HRSI will be used directly for image matching and use the match tie points to transform the HRSI image coordinates to the Orthophoto image coordinates through 2D coordinate transformation solution. Since there are likely to be many false or poorly matched tie points, the coordinate transformation will most likely be an iterative process to be run after culling the rejected match points. This case will require answers to the following questions:

Q3: What image matching approach will be optimal for use?

Q4: What 2D transformation model will be most effectively applicable?

Q5: What should be the rejection threshold(s) for poorly matched points?

It is likely that each one of the above 5 questions may have been investigated either individually or in some combination by researchers in the past. Most often such research has been carried out in an academic environment where the effort is mostly focused on proving concepts. In sharp contrast, the special contribution by the author of this study is aimed at seeking answers collectively for the above 5questions posed, so as to optimally design a semi-automated process for the georeferencing of HRSI for use in a routine production environment. Such a practice-oriented effort has not so far been reported.

Even after successfully achieving the above research objective, the extraction of map features will continue to be done manually in order to update the existing map database.

1.5 Thesis organisation

The remaining thesis chapters are organized as follows:

Chapter 2 describes the various satellite systems that currently generate commercially available imagery with brief introduction about space scanners. This information is then summarized in a table of currently operational satellite systems.

Chapter 3 discusses in depth the various mathematical models that can be used for mapping from HRSI.

Chapter 4 describes the areas chosen for this research study. The HRSI coverage available for the study areas and used for testing and evaluation is also described.

Chapter 5 discusses the methodology used for mapping of the study areas using selected HRSI coverage. It also includes the rationale and the design of experiments to be carried out to address the questions posed in Section 1.4.4. Some additional research effort and the possibilities for map production work flows are also described.

Chapter 6 discusses the results obtained from various experiments and carries out an analysis of the data resulting from various experiments to draw conclusions.

Chapter 7 summarizes the thesis conclusions and includes some recommendations and prospects for future effort.

Chapter 2. High Resolution Satellite Imagery

Even though imagery acquired from sensors mounted on a satellite has been available since 1972, the interest in the use of this imagery has increased steadily with the progressive increase in the satellite imagery resolution. Currently, a large number of satellite systems carrying high resolution optical sensors are operational. This has resulted in a widespread use of satellite imagery for the photogrammetric generation of geospatial data. This Chapter describes the satellite imaging systems that offer high potential for topographic mapping. The first part deals with the basic concepts of space sensors. This is followed by the second part that provides examples of high resolution satellite imaging systems.

2.1 Basics of Space sensors

Space sensors can be classified into two distinct classes (Petrie1999)

- film cameras that generate images in the form of photographic films; and
- scanners that employ photo-diodes or solid-state CCD detectors to generate images directly in the form of digital data.

Today, most of the sensors are pushbroom scanners so here we are mainly discussing this scanning geometry. We begin, however, with opto-mechanical scanners.

2.1.1 Early scanning principle

The basic scanning principle illustrated in Figure 2-1shows that all scanner images are built up sequentially line by-line using the platform motion over the ground. This results in a continuous strip image of the imaged scene. Optical-mechanical scanning of each new line was used in early scanners such as the MSS and TM devices used in the Landsat series.

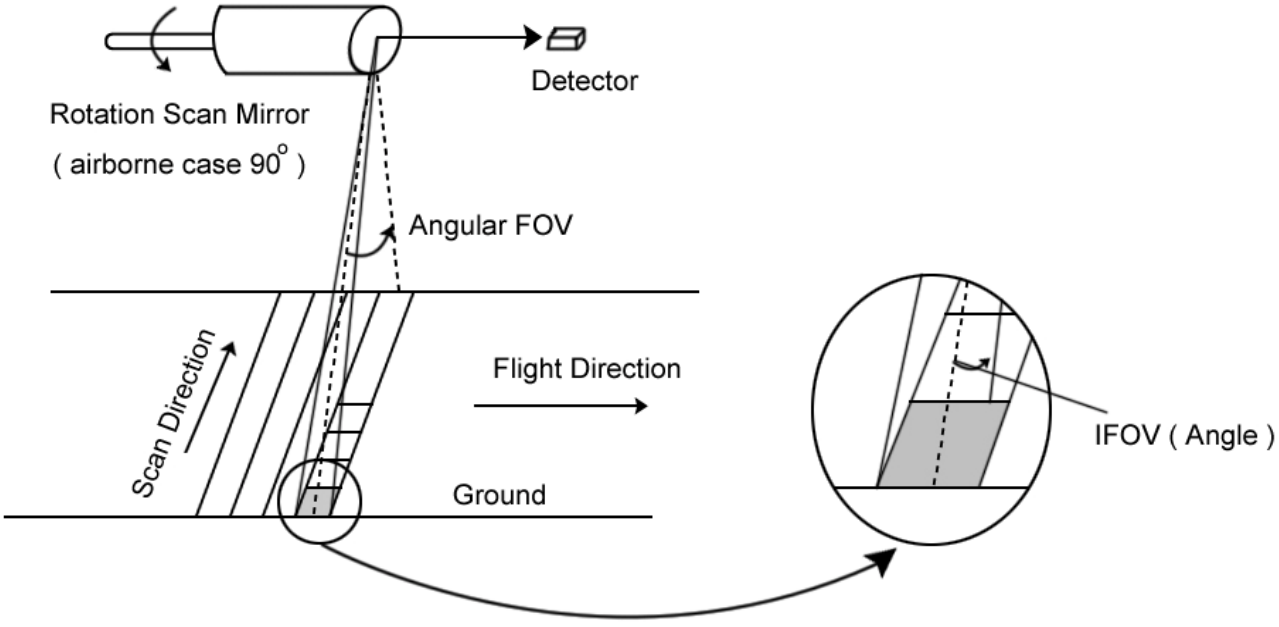

Figure 2-1 Early Scanning Principal (after Sabins, Jr., F.F., Remote Sensing: Principles and Interpretation)

2.1.2 CCD line scanners

The first CCD line scanner used was the German MOMS flown on Space Shuttle in 1983 as an experimental system. The first operational use was in the French SPOT-1 satellite launched in 1986. Now a days most scanners are "push broom" arrays in which a complete line is recorded at a time i.e. all detectors in a linear array CCD (Charge Coupled Detectors) record in parallel. Each line has its own exterior orientation (3D position and 3D attitude in space) but in short time intervals the translational and rotational changes (velocities) can be considered to be almost constant and rather small (with the exception of the forward motion of the space craft). This principle is illustrated in Figure 2-2 and Figure 2-3.

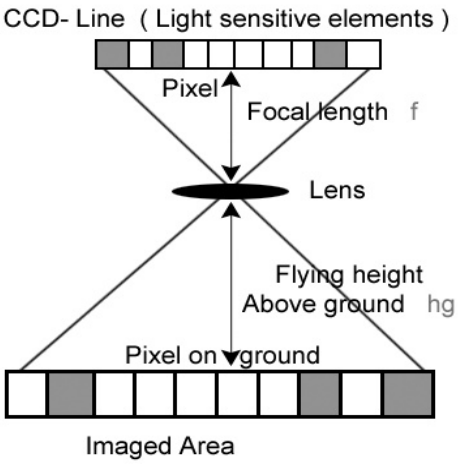

Figure 2-2: CCD Linear Array

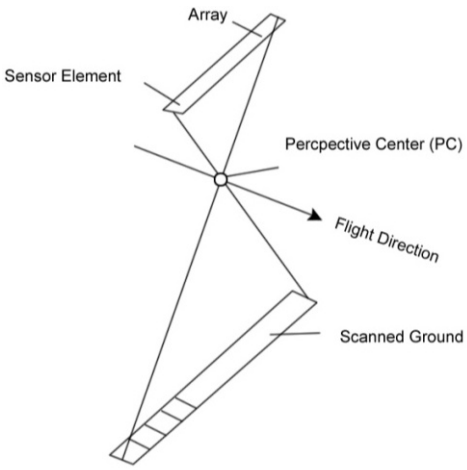

Figure 2-3: CCD Line Sensor

2.1.3 Characterization of the scanners according to the pointing direction for stereo data recording

There are three different configurations for stereo data recording: cross-track, along-track and flexible pointing.

2.1.3.1 Cross track configuration

The cross-track configuration makes use of a mirror that can be rotated in the cross-track direction (perpendicular to the flight path). Under command from a ground station, the mirror can be rotated in steps to either side of the flight line or orbital track. Stereo-coverage is produced from two separate flights on adjacent tracks using overlapping images acquired with the linear array sensor pointing in opposite directions during the two flights (Figure 2-4). This configuration is already in use with the existing SPOT and IRS-1C/D satellites.

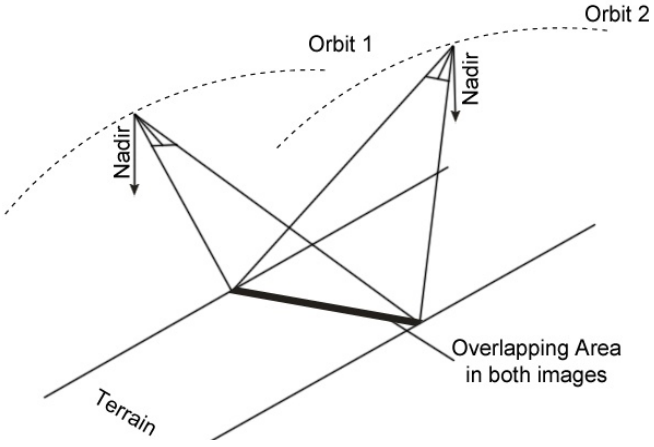

Figure 2-4: Cross Track Configuration (after Petrie1999)

2.1.3.2 Along track configuration

Along-track scanning sensor systems are equipped with two or more CCD line arrays, each tilted in a fixed orientation, one pointing in the forward direction down the flight line and the other pointing in the backward direction along the same line (Figure 2-5). These sensors produce overlapping images of the same piece of terrain from different positions in space during a single flight. When the two images are used in combination, they provide stereo-coverage of the swath of the Earth's surface that has been imaged by the two sensors. This configuration has already been used with the sensors mounted on board the MOMS-02 in 1993 and JERS-OPS satellites in 1992 (Petrie1999).

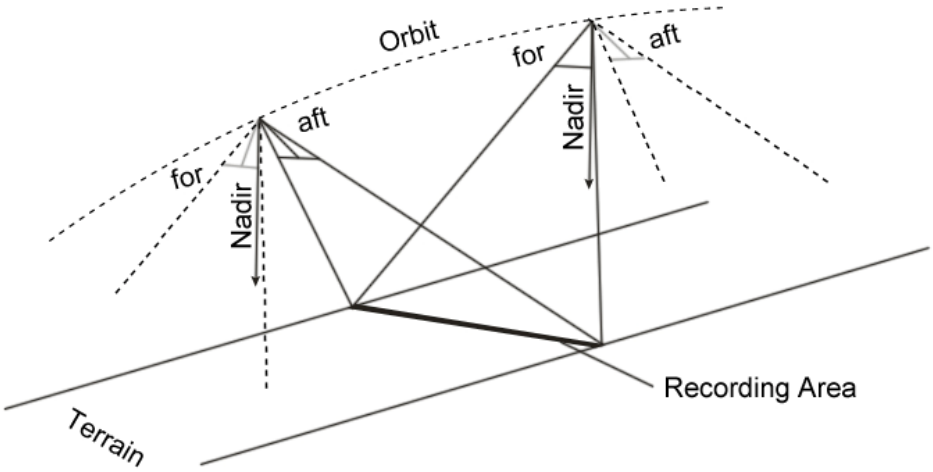

Figure 2-5: Along track configuration (after Petrie1999)

2.1.3.3 Flexible pointing configuration

Flexible pointing utilizes either gimballed mirrors or a whole body movement of the spacecraft. Whichever method is used, the sensor can be commanded to point in any direction, usually at viewing angles of up to 45° from the vertical. This allows the acquisition of image data in both the cross-track and along-track directions or in any other intermediate direction (Figure 2-6). Stereo-coverage of an area of terrain can be acquired either from a single orbital flight or from adjacent orbits. This arrangement is a feature of almost all the new commercial high-resolution satellites.

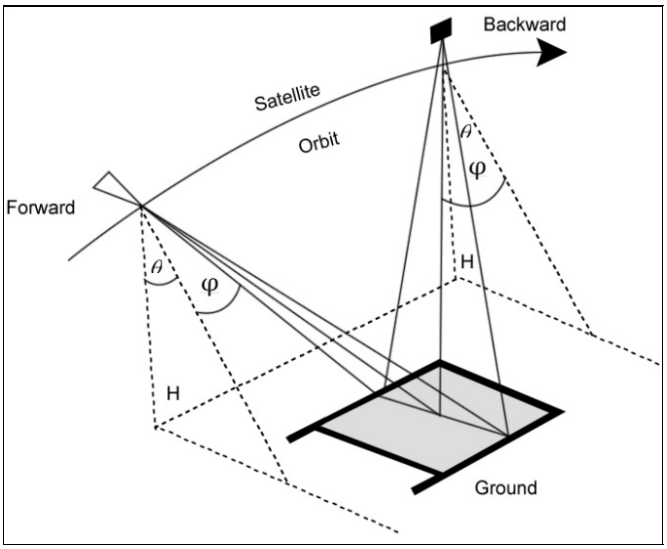

Figure 2-6: Flexible Pointing Configuration (after Petrie1999)

2.1.4 HRSI characteristics for topographic mapping

There are a number of HRSI characteristics which are ideally suited to topographic mapping applications, which was not previously the case with MRSI. This includes high spatial resolution that has significantly enhanced the ability for interpretation of features based on shape and texture, as well as the benefits of an agile sensor and subsequent along-track stereo acquisition which is advantageous for stereo interpretation. Equally important considerations for mapping applications are the design of satellite orbit parameters and the reconstruction of image to space geometry.

2.1.5 Satellite orbit

Satellites carrying sensors for mapping purposes require sun illumination to image in the visible spectrum, and consistent lighting conditions are preferred for mosaicking and for analyzing multiple scenes of the same area captured by revisiting the location. Therefore, satellites with HRSI sensors are designed to follow a sun-synchronous orbit to provide continuous illumination of the ground along its track. The inclination angle between the orbital plane and the equator is approximately 98° permitting the sensor to cover a large area of the Earth's surface as it travels North to South, crossing the Equator at approximately 10:30 am local time.

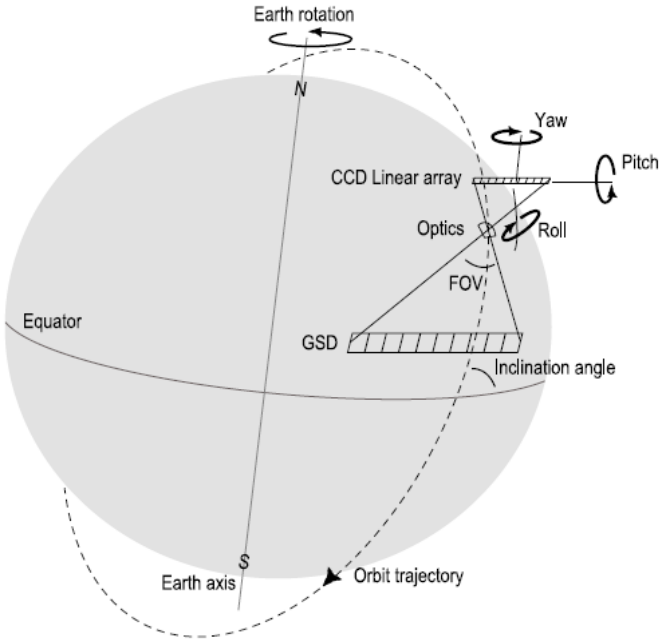

Figure 2-7: Typical space borne pushboom scanner orbit

The satellites carrying imaging sensors follow an elliptic orbit around the Earth, and any perturbations in the satellite path due to gravitational attractions of the Earth, Sun and Moon, solar radiation pressure and atmospheric drag result in deviations of the satellite from its reference mathematical path. However, the satellite position and attitude can be accurately determined with a global navigation satellite system (GNSS), such as GPS, star sensors and gyros. Smearing effects in the image may be created if there are velocity variations and similarly, altitude variations will alter pixel spacing.

The pushbroom linear array scanner acquires an image in strips as the satellite moves forward in its orbit. As the pixel size in the image space is constant, the ground distance of the pixel increases as the pixel becomes further away from nadir. Therefore, the sensor does not perfectly replicate the Earth and results in variable pixel sizing in the across-track direction, although these variations are small. It is more likely that other sources of errors contribute to large discrepancies, such as the instability of the sensor geometry.

2.1.6 Spatial resolution

Accurate measurements of terrain features require adequate image quality to replicate physical objects. The detail discernible in an image is dependent on the spatial resolution of the sensor and refers to the size of the smallest possible feature that can be detected. It is a function of the instantaneous field of view (IFOV) and the altitude and attitude of the sensor. The launch of IKONOS-2 by Space Imaging (later GeoEye and now DigtalGlobe) in 1999 provided civilian users with 1-m GSD imagery. Continuing advances in the satellite imaging sensor technology over the years have now made meter-level and sub-meter spatial resolution commercially available for mapping applications.

In this context, it needs to be emphasized that the GSD or the spatial resolution alone does not define the satellite image quality. Several factors that are beyond the user control affect the overall image quality, such as scene contrast and other radiometric characteristics that are affected by atmospheric and seasonal conditions and changing illumination resulting in shadows and other image artifacts due to sensor and sun geometry. Consequently, a distinction has to be made between the ability for the identification of features and image resolution. At the same time, while using 1 meter or sub-meter HRSI, shape and texture are better preserved which enhances the identification and measurement of ground features, as objects are represented over multiple pixels rather than a single pixel.

2.1.7 Agile imaging sensors

The older satellite imaging sensors were designed to collect the images of Earth in a fixed orientation. This could provide repeat coverage of the same area on Earth after several days or even weeks. The common weather and other atmospheric changes during long delay interval often resulted in large radiometric differences between two successive or overlapping satellite images that caused considerable difficulties both in qualitative and metric image exploitation. This fact seriously hindered the ability for manual extraction of features through stereo viewing as well as for automated image matching for generating digital elevation models. This led to the design of agile sensors (see also section 2.1.3.3) that rotate around three axes, such that after an initial forward image is acquired, the satellite can be steered within a short time to point backwards to image the same scene in similar illumination conditions (Gordecki and Dial, 2001).

IKONOS was designed as an agile system with the ability to maneuver to image up to 60° off-nadir. This shortens the revisit time and allows stereo imaging to be acquired across track from two orbits and along track imaging in a single orbit. Reverse scan mode describes the more commonly used imaging mode of IKONOS where scanning is in the same direction as the satellite trajectory, with the elevation angle essential remaining approximately constant throughout the scanning of the image. Forward scan mode, as for example used by QuickBird, scans in the opposite direction to the satellite trajectory, which introduces non-linearities as the sensor view angle changes with time. Since then, several other satellite imaging companies such as DigitalGlobe have launched agile satellite imaging sensors that are discussed in the following Sections. At the end of this Chapter, the technical features of all the satellite systems are summarized in Table 2-1: High Resolution Imaging Satellites.

2.2 Examples of High Resolution Satellite Systems

2.2.1 GeoEye

GeoEye Inc. (formerly Orbital Imaging Corporation or ORBIMAGE, now belonging to GeoEye) is a commercial satellite imagery company based in Virginia, US. In 2006, ORBIMAGE fully acquired the Colorado; US based company Space Imaging and changed the brand name to GeoEye. It is currently operating two satellite imaging systems described below.

2.2.1.1 IKONOS

The IKONOS sensor images with a single Kodak telescope, which itself consists of three curved and two flat mirrors. The five mirrors are designed and placed such that object rays are directed towards the focal plane to minimize optical distortions. Housed in the focal plane are one forward and one reverse TDI panchromatic array, and 4 multispectral linear CCD arrays. While the telescope length is approximately 2 m, the focal length is 10 m and has a narrow FOV of just 0.98°. Orbiting 680 km above the Earth, each pixel in the panchromatic imagery represents 0.82 m on the ground and multispectral pixels correspond to 3.28 m in object space depending on the off-nadir angle. However, the image distributed by Space Imaging is resample to 1-m and 4-m GSD for panchromatic and multispectral images respectively, as the telescope aperture has a diffraction limit of approximately 1 m (Grodecki and Dial, 2001).

IKONOS is an agile system and can maneuver to image up to 60° off-nadir. In addition to shortening revisit time, this pointing capability allows stereo imaging acquired across track from two orbits and along track imaging in a single orbit. A single scene covers 121 km2 and is available to order in 6 differing levels depending upon processing level.

Spatial Resolution:	0.82 m panchromatic GSD at nadir; 3.2 m multispectral SD at nadir
Spectral Range:	526–929 nm, 445–516 nm (blue), 506–595 nm (green), 632–698 nm (red), 757–853 nm (near IR)
Swath Width:	11.3 km
Dynamic Range:	11 bits per pixel
Off-Nadir Imaging:	up to 45 degrees
Orbital Altitude:	681km

The following Figure 2-8 displays a sample IKONOS image.

Figure 2-8: Sample IKONOS imagery

2.2.1.2 GeoEye-1

The GeoEye-1 Satellite sensor was developed by GeoEye and features the sophisticated technology used in modern commercial satellite imaging systems.GeoEye-1 is capable of acquiring image data at 0.41 meter panchromatic and 1.65 meter multispectral resolution. However, the image is resampled at 0.5 meter GSD for distribution outside US. It also features a revisit time of less than three days, as well as the ability to locate an object within just three meters of its physical location. This newly developed sensor launched in 2008 is optimized for large projects, as it can collect over 350,000 square kilometers of pan-sharpened multispectral satellite imagery every day.

Panchromatic Sensor:	0.41 m GSD at nadir
Multispectral Sensor:	1.65 m GSD at nadir
Spectral Range:	450–800nm, 450–510 nm (blue), 510–580 nm (green), 655–690 nm (red) 780–920 nm (near IR)
Swath Width:	15.2 km
Off-Nadir Imaging:	Up to 45 degrees
Dynamic Range:	11 bits per pixel
Orbital Altitude:	681 km

Figure 2-9: Sample GeoEye Imagery

2.2.2 DigitalGlobe

DigitalGlobe was founded in 1993 under the name WorldView Imaging Corporation, became EarthWatch Incorporated in 1995, before finally becoming DigitalGlobe in 2002. DigitalGlobe is currently operating a constellation of three different imaging satellite systems that are described in the following Sections.

2.2.2.1 QuickBird

The QuickBird satellite orbits the Earth at an altitude of approximately 450 km and travels at7 km per second (DigitalGlobe, 2007). With a FOV of 2.1° and focal length of 9 m, the pushbroom sensor acquires imagery at a resolution of0.61 – 0.72 m for panchromatic and 2.44 – 2.88 m resolution for multispectral to a radiometric resolution of 11-bits. Within the focal plane, 6 panchromatic arrays operate with TDI and there are 6 four-linear multi spectral arrays; all CCD lines are partially staggered.

The satellite is agile such that oblique pointing is possible to up to 30° off-nadir. For the first few years of operation, along and across track stereo capability supported collection of same pass stereo pairs and therefore the scene content, lighting conditions and satellite geometry were the same for the two images. A stereo pair covered an approximate area of 21.2 km x 21.2 km, totaling 450 km2. However, for a number of reasons, including the need to conserve onboard fuel supplies, stereo imaging was discontinued in 2006. DigitalGlobe completed an orbit raise in April of 2011 designed to extend the mission life of the QuickBird sensor. An operational altitude of 482 km was achieved with an expected gradual descent to 450 km by early 2013 (DigitalGlobe, 2011).

DigitalGlobe's QuickBird products are provided at different levels depending on their positional accuracy and varying levels of processing, and as the positioning accuracy increases, so too does the price of the image product.

Panchromatic Sensor:	0.65 m GSD at nadir
Multispectral Sensor:	2.62 m GSD at nadir
Spectral Range:	430 - 545 nm (blue), 466 - 620 nm (green), 590 - 710 nm (red) 715 - 918 nm (near IR)
Swath Width:	18 km
Off-Nadir Imaging:	up to 45 degrees
Dynamic Range:	11-bits per pixel
Orbital Altitude:	482 km

Figure 2-10: Sample Quick Bird imagery

2.2.2.2 WorldView-1

DigitalGlobe launched WorldView-1 in September 2007 as the first of its "next-generation satellites" that are exceptionally agile commercial satellites. The high-capacity, panchromatic imaging system features 0.5 meter resolution imagery. Operating at an altitude of 496 kilometers, WorldView-1 has an average revisit time of 1.7 days and is capable of collecting over one million square kilometers per day of 0.5 meter imagery. The satellite is also equipped with state-of-the-art geo location accuracy capabilities and exhibits fast agility with rapid targeting and efficient in-track stereo collection. Its ability for bidirectional scanning and rapid retargeting using Control Moment Gyros can image areas stereoscopically on a single pass, ensuring image continuity and consistency of quality. It provides a 17.7 km wide swath at nadir.

Panchromatic Sensor:	0.5 m GSD at nadir
Swath Width:	17.7 km
Off-Nadir Imaging:	up to 45 degrees
Dynamic Range:	11-bits per pixel
Orbital Altitude:	496 km

2.2.2.3 WorldView-2

WorldView-2, launched in October 2009, is the first high-resolution 8-band multispectral commercial satellite. Operating at an altitude of 770 kilometers, WorldView-2 provides 46 cm panchromatic resolution and 1.85 meter multispectral resolution. WorldView-2 has an average revisit time of 1.1 days and is capable of collecting up to 785,000 km2 of 8-band imagery per day.

The WorldView-2 system, offering improved accuracy, agility, capacity and spectral diversity, allowed DigitalGlobe to expand its imagery product offerings to both commercial and government customers.

Panchromatic Sensor:	0.46 m GSD at nadir
Multispectral Sensor:	1.85 m GSD at nadir
Spectral Range:	450-800 (Panchromatic)
	8 Multispectral: 400-450 nm (Coastal), 450 - 510 nm (Blue), 510-580 nm (Green), 585 - 625 nm (Yellow), 630 - 690 nm (Red), 705 - 745 nm (Red Edge), 770 - 895 nm (Near-IR1), 860 - 1040 nm (Near-IR2)
Swath Width:	16.4 km
Off-Nadir Imaging:	up to 45 degrees
Dynamic Range:	11-bits per pixel
Orbital Altitude:	770 km

2.2.3 Merger of DigitalGlobe and GeoEye

In accordance with a recent press release (http://www.digitalglobe.com/digitalglobe-geoeye-combine), both DigitalGlobe and GeoEye have agreed to merge which they claim makes them a strong earth imagery and geospatial analysis service provider. However, the French Pleiades system will most likely offer significant competition to the newly merged DigitalGlobe.

2.2.4 SPOT-5

The SPOT satellite constellation has been acquiring images of the Earth since 1986. SPOT-1 through to SPOT-3 operated with twin along track High Resolution Visible (HRV) linear scanning array instruments. The HRV sensor incorporated a steerable mirror enabling across track pointing to 27° off-nadir. This allowed stereoscopic imagery to be acquired when the same scene was captured from different orbits; depending on latitude, an area could be viewed at an interval of 3-4 days. GSDs were provided at 10 m for the panchromatic channel and 20 m for each of the three multispectral bands (blue, red and near infrared). The HRV pairs were upgraded for SPOT-4 to include a shortwave infrared band (SWIR), termed High Resolution Visible and Infrared (HRVIR).

Derived from the HRV sensor, the latest addition to the SPOT family, SPOT-5, carries two High Resolution Geometry (HRG) instruments (Petrie 2001). The HRG has a FOV of 4°, a focal length of 1.082 m and travels in a circular orbit 832 km above the Earth. Matching its HRVIR predecessor, across track pointing capability extends to 27° oblique viewing. SPOT-5 carries two panchromatic sensors imaging at 5 m GSD, three multispectral bands capturing 10 m GSD and a SWIR channel at 20 m; all channels image in 8 bits. A 2.5 m product is generated from the two panchromatic bands using a sampling process patented by CNES as ‘Supermode’ (Gleyzeset al., 2003).

Spatial Resolution:	Pan: 5m, MS: 10m, SWI: 20m GSD at nadir
	Spectral Range: 480–710 nm (Pan), 500–590 nm (green), 610–680 nm (red), 780–890 nm (near IR) , 1,580–1,750 nm (Shortwave IR)
Swath Width:	60 km to 80 km
Dynamic Range	8 bits per pixel
Orbital Altitude:	822 km

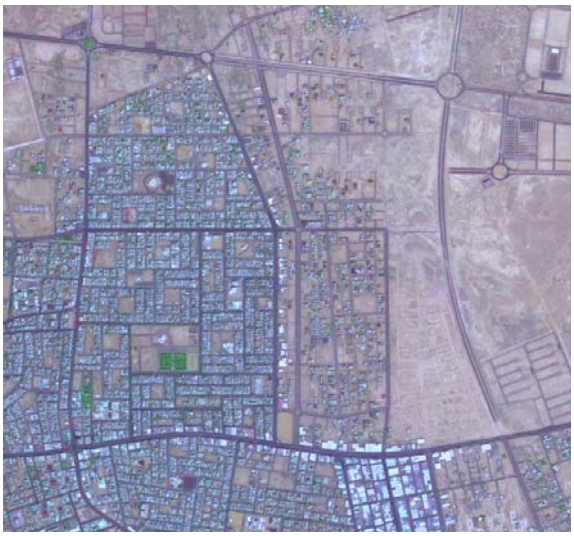

Figure 2-11: Sample SPOT-5 imagery

2.2.5 Other systems

While advancements in the existing satellite imaging systems is continuing, some additional countries such as Taiwan, India, etc. have also entered the space imaging market by launching new imaging satellites during the past decade. A brief description of some of these systems is included since they also provide HRSI that can be used for topographic mapping.

2.2.5.1 CARTOSAT-1

CARTOSAT-1is the first Indian Remote Sensing Stereo Satellite capable of providing in-orbit stereo images and was launched in May, 2005. The images are used for cartographic applications meeting the global requirements. The two line sensors of this satellite, PAN-Fore and PAN-Aft have a resolution of 2.5m. The CARTOSAT-1 provides stereo pairs required for generating Digital Elevation Models, Ortho Image products, and other products for mapping applications.

Spatial Resolution:	2.5 m (GSD at nadir).
Spectral Band:	0.4- 2.4 µm.
Swath:	30 km.
Cross-track:	up to 20 degrees
Orbital Altitude:	618 km
Dynamic Range:	11 bits per pixel

2.2.5.2 CARTOSAT-2

CARTOSAT-2 is an Earth observation satellite in a sun-synchronous orbit. The satellite was built, launched and is maintained by the Indian Space Research Organization. .

Spatial Resolution:	up to 80 cm (GSD at nadir).
Spectral Range:	0.5- 0.85 µm.
Swath:	9.6 km.
Off-Nadir Imaging:	up to 45 degrees
Orbital Altitude:	630 km
Dynamic Range:	11 bits per pixel

2.2.5.3 Pleiades-HR

Pleiades-HR is a two-spacecraft constellation of CNES (Space Agency of France), representing a long-term engagement with the introduction of advanced technologies in Earth observation capabilities. Starting with the first launch in 2011, the Pleiades program will follow the SPOT program satellite series services, with the overall objective to provide global coverage and daily observation accessibility to any point on Earth with optical high-resolution panchromatic (0.7 m) and multispectral (2.8 m) imagery with potential for high image location accuracy

The agile Pleiades satellites are capable to image targets along any ground direction within 47º of a vertical viewing position (with very low maneuver durations between two consecutive imaging scenes. Several types of acquisition modes are defined:

- One-pass acquisition mode: The satellite agility offers the possibility to locally enlarge (widen) the swath by realizing from the same orbit and thus quasi simultaneously the acquisition of several adjacent swaths within the Field Of Regard (FOR). Hence, it will be possible to acquire imagery with an area of approximately 120 km long, and 110 km wide, using the S/C pointing capability (maximal) in roll of 30º.
- Simultaneous stereoscopic or tri-stereoscopic acquisitions mode: This acquisition mode employs a variation of the one-pass mode. Instead of using the agility capabilities to acquire contiguous imagery, the same scene is acquired with two (or three) different view angles as shown in Figure 2-12.
- Multi-spot mode: Refers to a support mode in which the S/C acquires many spot targets around the S/C ground track, even fore and aft stereoscopic mode if needed. In this mode, the agility capabilities of the satellite are used to acquire the maximum of scenes on a given surface, in one day. (CNES, 2009)

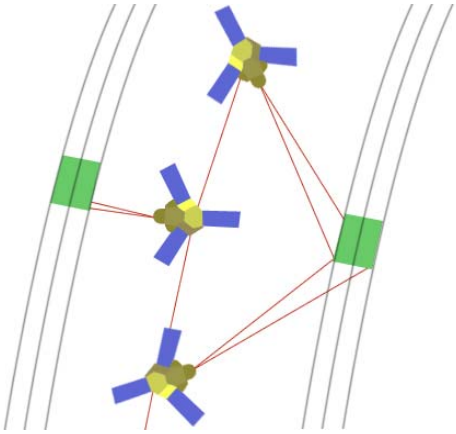

Figure 2-12: Simultaneous stereoscopic or tri-stereoscopic acquisitions mode with HIRI (Pleiades System, High-Resolution Optical Imaging Constellation of CNES)

Resolution: 50 cm (PAN), 2 m (MSS), 50 cm (Pan Sharpened), Bundle: 50 cm PAN & 2 m MS (GSD at nadir)

Spectral Range: 430-550 nm (blue), 490-610 nm (green), 600-720 nm (red), 750-950 nm (near IR), 480- 830 nm (pan)

Swath Width: 20 km

Orbital Altitude: 694 km

Dynamic Range: 8 bits per pixel

2.2.5.4 FORMOSAT-2

FORMOSAT-2 is the first satellite developed by the National Space Organization (NSPO) of Taiwan and was launched in May, 2004. After initial testing, it has been operational since 2006 and provides high resolution2 meter panchromatic and 8 meter multispectral satellite image data. The main mission of FORMOSAT-2 is to provide remote sensing imagery over Taiwan and on terrestrial and oceanic regions of the entire Earth.

The sensor is capable of providing imagery with cross-track and along-track (forward/aft) ± 45° viewing angles.

Panchromatic Sensor: 2 m GSD at nadir

Multispectral Sensor: 8 m GSD at nadir

Spectral Range: 0.45 - 0.90 µm (Panchromatic), 0.45 - 0.52 µm (Blue), 0.52 - 0.60 µm (Green) 0.63 - 0.69 µm (Red), 0.76 - 0.90 µm (Near-infrared)

Swath Width: 24km

Dynamic Range: 8 bits per pixel

Off-Nadir Imaging: up to 45 degrees

Orbital Altitude: 891 km

Name of Satellite / Sensor	**GeoEye-1**	**IKONOS**	**SPOT-5**
Company	DigitalGlobe (Formerly GeoEye)	DigitalGlobe (Formerly GeoEye)	CNES, France
Launch date	6th September, 2008	24th September, 1999	4th May, 2002
Launch Venue	Vandenberg Air Force Base, California, USA	Vandenberg Air Force Base, California, USA	Guiana Space Centre, Kourou, French Guyana
Altitude (km)	684 km	681 km	822 km
Weight	1,955 kg	726 kg	3,030 kg
Inclination (degrees)/ local time of equator crossing	98 / 10:30 am	98.1 / 10:30 am	98.7 / 10:30 am
Orbit type / period	Sun Synchronous, 98-min period	Sun Synchronous, 98-min period	Sun Synchronous, 101.4-min period
Revisit Frequency	~3 days for 40° nadir angle	~3 days for 40° nadir angle	2 - 3 days
Expected life time	Fully redundant 7+ year design life; fuel for 15 years	11 year	5 years
Spectral Resolution	Pan, MSx4	Pan, MSx4	Pan, MSx4
Spatial Resolution	0.41 Pan nadir, available with 0.5m	0.82 m GSD Pan at Nadir	2.5 m from 2x5 m scenes

Name of Satellite / Sensor	**GeoEye-1**	**IKONOS**	**SPOT-5**
Intensity Range (bits)	11 bits	11 bits	8 bits
Pan sharpened	Yes	Yes	Yes
Swath width (km)	15.2 km at Nadir	11.3 km at Nadir	15.2 km at Nadir
Scene Size (km)	Single Point Scene: 15x15km Contiguous Area: 300x50 km Contiguous Stereo: 224x28 km	Single Point Scene: 11x11 km	Single Point Scene: 60x60 km 360x120 km large area
Stereo (Along/Across track)	Along track	Along track	Across track
Geolocation Accuracy	90% CE Mono 2.5 m 90% CE Stereo 2.0 m 90% LE Stereo 3.0 m	90% CE Mono 15 m	Less than 15 m
File Format	GeoTiff	GeoTiff, NITF	GeoTiff, DTED
Name of Satellite / Sensor	**QuickBird**	**WorldView1**	**WorldView-2**
Company	Digital Globe	Digital Globe	Digital Globe
Launch date	18th October, 2001	18th September, 2007	8th October, 2009
Launch Venue	Vandenberg Air Force Base, California, USA	Vandenberg Air Force Base, California, USA	Vandenberg Air Force Base, California, USA
Altitude (km)	450 km	496 km	770 km
Weight	950 kg	2,500 kg	2,800 kg
Inclination (degrees) / local time of equator crossing	98 / 10:30 am	98 / 10:30 am descending node	98/ 10:30 am descending node
Orbit type/period	Sun Synchronous, 93.5-min period	Sun Synchronous, 94.6-min period	Sun Synchronous, 100-min period
Revisit Frequency	2.6 at 20 deg off-nadir	1.7 day at 20° off-nadir	1.1 day at 20° off-nadir
Expected life time	7-10 years	7-10 years	7-10 years
Spectral Resolution	Pan, MSx4	Pan	Pan, MSx8
Spatial Resolution	0.67/0.72 m Pan	0.43 m GSD at Nadir, avalaible with 0.5m	0.46 m GSD Pan at Nadir, available with 0.5m
Intensity Range (bits)	11 bits	11 bits	11 bits
Pan sharpened	Yes	No	Yes
Swath width (km)	16.5 km at Nadir	17.6 km at Nadir	16.4 km at Nadir
Stereo	Along track	Along track	Along track
Geolocation Accuracy	90% CE 23 m (no ground control) 90% LE 17 m (no ground control)	90% CE 6.5 m 90% LE 6.5 m	90% CE Mono 6.5 m 90% CE Mono 6.5 m
File Format	GeoTiff 1.0, NITF 2.0/2.1	GeoTiff 1.0, NITF 2.0/2.	GeoTiff 1.0, NITF 2.0/2.

Name of Satellite / Sensor	**Pléiades-HR**	**CARTOSAT-2A**	**KOMPOSAT-2**
Company	CNES, France	ISRO, India	KARI, Korea
Launch date	17th December 2011	28th April, 2008	28 July, 2006
Launch Venue	Kourou	Satishdhawan space center India	PletsetskCosmodrome,Russia
Altitude (km)	694 km	637 km	685 km
Weight	1,000 kg	690 kg	800 kg
Inclination (degrees)	98.2º	97.9 º	98.13 º
Orbit type/period	Sun-synchronous phased orbits	Polar Sun Synchronous	Sun Synchronous
Expected life time	5 year	5 year	3 year
Spectral Resolution	2-meter multispectral	Pan	Pan,MSx4
Spatial Resolution	0.7- m pan	0.82m pan	1-m pan
Intensity Range (bits)	11 bits	11 bits	10 bits
Pan sharpened	Yes	Yes	Yes
Swath width (km)	20 km	9.6 km	15x15 km
Scene Size (km)	3600 km2	92.16	15 X 15 km
Stereo (Along/Across track)	Along-track	Free view direction	Free view direction
Geolocation Accuracy	90% CE 3m without GCPs	250 m	CE90: 80 m
File Format	GeoTIFF	GeoTIFF	GeoTIFF

Table 2-1: Summary of characteristics of current High Resolution Satellite Imaging Systems

Chapter 3. Models for Mapping from HRSI

The last chapter described in detail various HRSI systems that are currently operational and generate imagery of sufficiently high metric quality that can be used for topographic mapping. This chapter describes the practical aspects of HRSI that influence the quality of the map products generated from HRSI. This requires a careful understanding of the type of geometric errors present in HRSI data and the mathematical models used for mapping that can account for such errors.

3.1 Geometric Characteristics of HRSI

The characteristics of HRSI that are directly relevant to mapping include the perturbations in the satellite orbit, imaging mode and the interior and exterior orientation of the imaging sensor. The effects of the satellite orbit and the imaging mode have been described earlier in chapter 2.

3.1.1 Interior and Exterior Sensor Orientation

One of the advantages of CCD arrays is their very stable interior orientation (Jacobsen, 2006). However, linear CCD segments within the focal plane or the flexing of full arrays and scale changes can influence image geometry. Since HRSI sensors use a very narrow field of view, non-linear image distortions are very much reduced. Even small exterior orientation errors mainly only cause 2D shifts in image space and 3D shifts in object space. Of the errors in the sensor exterior orientation, the pitch errors causes shifts in object space in the along-track direction, while the errors in roll cause cross-track shifts. Such errors can be of large magnitude and are usually noticeable in low-level products such as QuickBird “Basic“ and IKONOS “Geo“ images. Often, the yaw and scale errors are insignificant for HRSI (Jacobsen, 2006). Table 3-1, summarizes the various factors that can influence the errors in any HRSI scene (Baltsavias et al. 2006).

The interior and the exterior orientation data supplied by the HRSI vendors (often in the form of rational polynomial coefficients, RPCs)usually has systematic residual errors that result in biases in computed planimetric coordinates or in 3D positioning when processing stereo imagery, when vendor provided RPC data is used. It has been demonstrated that there need be no loss in georeferencing accuracy when bias-corrected RPCs are employed (Fraser and Hanley, 2003; Fraser et al., 2005). Another approach used is to develop generic sensor models that take full account of the physical imaging process by incorporating time dependent satellite orbit models and interior orientation provided by the satellite imagery vendors. Using such models, the self-calibration approach that is often used for the calibration of photogrammetric imaging systems can be employed to model systematic errors with additional parameters. For example, Kocaman and Gruen (2008) used ten additional parameters for each of the three cameras of the ALOS/PRISM sensor to account for the scale and blending effects and for the displacements of the centers of the CCD chips from the principal point. An affine model is used in Weser et al., (2008) to compensate for the displacement of the relative positions of the CCDs. However, even though efficient, the self-calibration approach requires a significant amount of GCPs. Also, the results are not always stable due to the correlation of model parameters, and the outcome is highly influenced by the distribution of GCPs. More recently, Zhang and Fraser (2012) have proposed to correct the IO errors by detailed examination and efficient modeling the IO error distribution in the focal plane.

Since this research is aimed at optimizing the georeferencing accuracy of HRSI by employing the available models, the biases introduced by the residual errors in exterior orientation are expected to play a more dominant role. It is proposed to demonstrate that the resulting biases in georeferencing can be minimized to an acceptable degree through the use of existing ground control data.

Interior Orientation	Linear CCD Arrays • Scale change; change in pixel size • Full CCD segments shifted or rotated within focal plane • Bending of CCD linear arrays into an arc • Temperature effects Sensor Optical Distortions • Symmetric lens distortion • Decentering lens distortion • Change in focal length • Cross track scale variation due to CCD line out of focal plane or rotated in focal plane • Principal point displacement
Exterior Orientation	GPS Measurements • Clock errors • Multipath • Antenna phase center shifts • Ionospheric and tropospheric refraction
Exterior Orientation	INS Measurements • Initialization and alignment errors • Eccentricity between GPS antenna, INS center of rotation and the perspective center of the imaging sensor • Drift in calibration parameters • Gravity model Star Trackers • Spatial frequency errors • Temporal noise
Imaging Mode	Across-Track Stereo • Time lag between stereo pairs - Radiometric variation - Land cover variation Along-Track Stereo • Agile Sensor - Variations in scanning angle Asynchronous Acquisition (Forward Scanned) • Angular changes between optic axis and velocity vector • Smaller GSD in flight direction • Non-linear imaging geometry due to temporal changes in viewing angle

Table 3-1: Summary of factors influencing errors in HRSI

3.2 Georeferencing of HRSI

Before any reliable map data can be extracted from HRSI, it is essential to reconstruct the image space to object space geometry by using an appropriate sensor model. A review of the current literature shows that a variety of sensor models have been used including the collinearity based models, Direct Linear Transform (DLT) as well as models derived from satellite orbital data (Weser et al. 2008). Some of these models are briefly described and their applicability to this study is discussed in this section.

3.2.1 Collinearity Based Models

A large number of imaging systems used for photogrammetric mapping generate imagery that capture a perspective geometric relation between images and object space. Such a relationship, illustrated in **Figure 3-1** is based on the simple geometric condition that the image point p, the corresponding object space point P and the perspective center of the imaging sensor are collinear (Kraus, K., 2004).. Mathematically, this geometric condition is captured by the two collinearity condition equation 3.1 below:

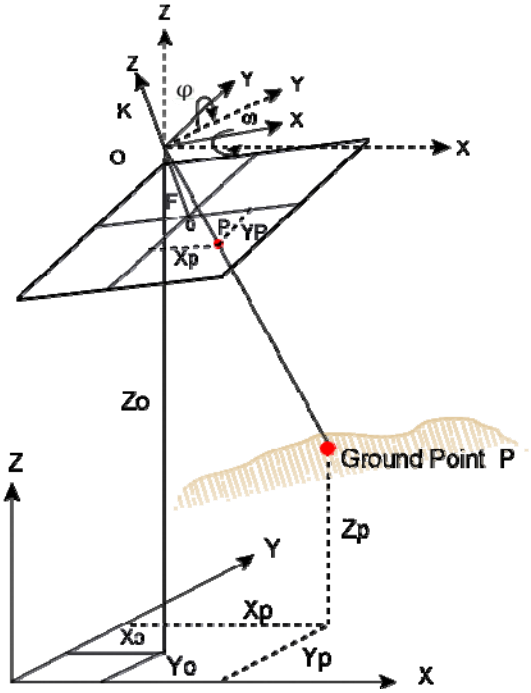

Figure 3-1: Collinearity condition

$$x_p = -f\left[\frac{m_{11}(X_P - X_0) + m_{12}(Y_P - Y_0) + m_{13}(Z_P - Z_0)}{m_{31}(X_P - X_0) + m_{32}(Y_P - Y_0) + m_{33}(Z_P - Z_0)}\right]$$

$$y_p = -f\left[\frac{m_{21}(X_P - X_0) + m_{22}(Y_P - Y_0) + m_{23}[Z_P - Z_0]}{m_{31}(X_P - X_0) + m_{32}(Y_P - Y_0) + m_{33}(Z_P - Z_0)}\right] \quad \text{Equation 3.1}$$

Where;

X_P, Y_P, Z_P: are the object space coordinates of a ground point P

X_0, Y_0, Z_0: are the object space coordinates of the perspective center O of the sensor

x_p, y_p: are the image coordinates of the image point p of the ground point P

f: is the calibrated focal length of the sensor

ω, ϕ, κ: are the spatial orientation angles of the sensor

The coefficients m11, m12,...,m33 are the elements of a 3x3 rotational matrix M as shown below and are functions of the orientation angles ω, ϕ and κ.

$$M = \begin{pmatrix} m_{11} & m_{12} & m_{13} \\ m_{21} & m_{22} & m_{23} \\ m_{31} & m_{32} & m_{33} \end{pmatrix}$$

Even though the collinearity model as given by Equations 3.1 is the most commonly used model for imagery obtained with aerial frme cameras, it has to be modified to fit the geometry of a linear pushbroom sensor. In the case of a pushbroom sensor, images are obtained line segment by line segment at a uniform rate. The resulting imagery is composed of consecutive scan lines where each scan line has its own time-dependent interior and exterior orientation parameters (Hoffmann et al., 1984, Gordecki and Dial, 2003). Consequently, the traditional collinearity equations must be modified as Equations 3.2 shown below:

$$x(t) = -f \frac{m_{11}(t)\left(X_P - X_0(t)\right) + m_{12}(t)\left(Y_P - Y_0(t)\right) + m_{13}(t)\left(Z_P - Z_0(t)\right)}{m_{31}(t)\left(X_P - X_0(t)\right) + m_{32}(t)\left(Y_P - Y_0(t)\right) + m_{33}(t)\left(Z_P - Z_0(t)\right)}$$

$$y(t) = -f \frac{m_{21}(t)\left(X_P - X_0(t)\right) + m_{22}(t)\left(Y_P - Y_0(t)\right) + m_{23}(t)\left(Z_P - Z_0(t)\right)}{m_{31}(t)\left(X_P - X_0(t)\right) + m_{32}(t)\left(Y_P - Y_0(t)\right) + m_{33}(t)\left(Z_P - Z_0(t)\right)} \qquad \text{Equation 3.2}$$

Where;

X_P, Y_P, Z_P:	are the object space coordinates of a ground point P
$X_0(t)$, $Y_0(t)$, $Z_0(t)$:	are the object space coordinates of the perspective center O of the sensor at epoch t
$X(t)$, $y(t)$:	are the image coordinates of P at epoch t
f:	is the calibrated focal length of the sensor
ω(t), ϕ(t), κ(t):	are the spatial orientation angles of the sensor at epoch t
$m_{11}(t)$, $m_{12}(t)$,..,$m_{33}(t)$:	are the elements of the orientation matrix M(t) at epoch t and are functions of ω(t), ϕ(t) and κ(t)

In order to use the above Modified Collinearity model to reconstruct the exterior orientation parameters of the sensor as a function of time, i.e. the position and the motion of the satellite along its orbit must be modeled. The movement of the satellite along its Keplerian orbit is fully defined by six orbital parameters. These include a, the semi-major axis of the elliptical orbit and e, the eccentricity; these two parameters define the size and shape of the orbital ellipse. The inclination *i*, the argument of perigee ω and the right ascension of the ascending node Ω determine the orientation of the orbital plane in the inertial space, while the true anomaly f determines the location of the satellite along its elliptical path (Seeber, 1993).

Modified collinearity-based models have been applied for georeferencing line scanners of medium-resolution satellite imagery (MRSI), such as, for example SPOT. The collinearity condition equations pertaining to an epoch t are modified to include six orbital parameters at epoch t as unknowns, and with the sensor viewing angle as the seventh unknown require a minimum of four GCPs for a solution (Gugan and Dowman, 1988; Michaelis and Dowman, 2004). Similar orbital parameter approach has been reported for IRS-1C (Radhadevi et al., 1998) and KOMPSAT-1 sensors (Kim and Dowman, 2006).

Another sensor orientation model for line scanner imagery based on time-variant collinearity condition models the

satellite motion as polynomial functions of time. The exterior orientation parameters are modeled for selected reference lines, and the fact that these parameters are highly correlated between adjacent lines is used to interpolate the parameters for intermediate lines. Finally, the unknown parameters are adjusted in a simultaneous bundle solution. Such an approach has been reported for MOMS imagery (Ebner, Müller 1986, Fraser and Shao, 1996, Ebner, et al., 1999).

The modified collinearity equations have rarely been used as a georeferencing model for HRSI. In the absence of a sensor model and satellite positional and ephemeris data, such as is the case with IKONOS imagery, and despite other vendors such as DigitalGlobe providing ephemeris information, there is no incentive for using the modified collinearity as a viable sensor model. In addition, alternate models for sensor orientation have been proposed some of which will now be described.

3.2.2 Direct Linear Transformation (DLT) Model

The Direct Linear Transformation (DLT) model directly establishes a projective relationship between a point in 3D object space with its projected 2D image point. It has been used largely in close-range photogrammetric applications, especially when using images taken from a non-metric camera (Abdel Aziz and Karara, 1971). Mathematically, such a transformation is expressed as shown in Equation 3.3:

$$x = \frac{L_1X + L_2Y + L_3Z + L_4}{L_9X + L_{10}Y + L_{11}Z + 1} \qquad y = \frac{L_5X + L_6Y + L_7Z + L_8}{L_9X + L_{10}Y + L_{11}Z + 1} \qquad \text{Equation 3.3}$$

Where;

x,y: are the 2D image coordinates

X,Y,Z: are the coordinates in 3D object space

In the above equation, L_1, L_2,...,L_{11} are the unknown coefficients which can be approximated if a minimum of 6 GCPs are available. It is necessary that the GCPs must be well distributed so as to fully reflect the range of variation in X, Y and Z in object space.

The justification for using the DLT model for line scanner imagery is the fact that the image is central perspective in the cross-track direction (El-Manadili and Novak, 1996). The primary advantage of using the DLT model is the fact that a multi-image DLT triangulation does not require camera or ephemeris information to obtain 3D geopositioning.

Variations of the DLT have been suggested to incorporate corrections for self-calibration (Wang, 1999) and adapted to piece-wise functions (Yang, 2001). Both approaches have been tested for processing MRSI with reasonable success. However, the DLT has not been used extensively as a sensor orientation model for HRSI. The main reason is the requirement for a larger number of GCPs and their distribution in object space to obtain geopositioning accuracy that is comparable to what is achievable with alternative methods (Fraser et al., 2002, Jacobsen, 2006). Consequently, there is not much incentive in the use of DLT for HRSI.

3.2.3 Rational Function Model

Rational Functions (RFs) in their direct form are like collinearity equations in expressing the image space coordinates as a function of object space coordinates. The RFs carry no reference to the sensor model nor to the satellite ephemeris; their development and use have mostly been promoted by the defense industry (Greve et al., 1992; Dowman, 1992). Due to their applicability to frame and panoramic cameras as well as pushbroom line scanners, their use has also been widely adopted by the civilian photogrammetric industry. RF-based sensor models are now readily implemented in commercial

photogrammetric software packages and have been recognized by the Open Geospatial Consortium (OGC) as a standard geometry model for satellite imagery (OGC, 2004).

The parameters of the sensor model for HRSI are either supplied by the image provider, as is the case with Rational Polynomial Coefficients (RPCs) for IKONOS and QuickBird imagery, or can be determined in an orientation procedure requiring GCPs and corresponding image coordinate measurements. This alternative approach, resulting in rational function models (RFMs) has been reported by several investigators to produce accuracy better than product expectations (Tao et al., 2002; Toutin and Cheng, 2002; Yang, 2000; Di et al., 2003). Moreover, by correcting the inherent biases in the RFs, 1-pixel level positioning in object space can be achieved (Fraser and Hanley, 2003; 2005; Grodecki and Dial, 2003).

The HRSI RPC replacement sensor model has been comprehensively described in Grodecki and Dial, (2001) and Tao and Hu (2002) and is based on the backward transformation from object space to image space. IKONOS RPCs are derived from a rigorous sensor model (Grodecki and Dial, 2003) and supplied with the imagery. Forward RPCs express image space coordinates as a function of object space coordinates, whereas inverse RPCs express planimetric object space coordinates as a function of image coordinates and object elevation. To improve numerical precision, image- and object-space coordinates are normalized to (-1, +1) range (Gordecki and Dial, 2003). Custodians of HRSI have adopted terrain independent forward RPCs as an alternative sensor orientation model for processing HRSI. Such a model consisting of 80 terms with 10 additional scale and offset terms per image, is expressed by equation 3.4, as a ratio of two third-order polynomial functions:

$$x_{ij} = \frac{P_{i1}(X,Y,Z)_j}{P_{i2}(X,Y,Z)_j} \qquad y_{ij} = \frac{P_{i3}(X,Y,Z)_j}{P_{i4}(X,Y,Z)_j} \qquad \text{Equation 3.4}$$

Where for any point

x_{ij}, y_{ij} are image coordinates; normalized with offset and scale

$$x = \frac{Line-Offset}{Scale} \qquad y = \frac{Step-offset}{Scale} \qquad \text{Equation 3.5}$$

X,Y,Z are object space coordinates; normalized with offset and scale

$$X = \frac{Longitude-Offset}{Scale} \qquad Y = \frac{Latitude-Offset}{Scale} \qquad Z = \frac{Height-Offset}{Scale} \qquad \text{Equation 3.6}$$

P_{ij} with j=1,..4 express a 20-term cubic polynomial function of object space coordinates; representing 80 RPC coefficients a_{kj} with k=1,…20 and j=1,…4

$$\begin{aligned} P_{ij}(X,Y,Z)_j = {} & a_{1j} + a_{2j}Y + a_{3j}X + a_{4j}Z + a_{5j}YX + a_{6j}YZ + a_{7j}XZ + a_{8j}Y^2 \\ & + a_{9j}X^2 + a_{10j}Z^2 + a_{11j}XYZ + a_{12j}Y^3 + a_{13j}YX^2 + a_{14j}YZ^2 \\ & + a_{15j}Y^2X + a_{16j}X^3 + a_{17j}XZ^2 + a_{18j}Y^2Z + a_{19j}X^2Z + a_{20j}Z^3 \end{aligned} \qquad \text{Equation 3.7}$$

The RPCs which are solely produced from the data from on-board GPS receivers, gyros and star trackers, often suffer from systematic biases, primarily in attitude determination. Due to a lack of reference to any GCP data geopositioning biases are also present in image products. Such biases must be removed in order to exploit the full metric accuracy potential of HRSI (Fraser et al., 2002; Fraser et al., 2006).

Consequently, an extended RPC bundle adjustment was developed to model these effects and to compensate for existing biases (Grodecki and Dial, 2003; Fraser and Hanley, 2005). This is given by equation 3.8. The revised generation of bias-corrected RPCs represented as P^{c}_{ij} in Equations 3.9 and 3.10 (given for the two numerators only; those for the denominators look alike) has been reported to produce 1-pixel level positioning in object space without using additional correction terms (Fraser and Hanley, 2005).

$$x_i + L_{0\,ij} = \frac{P_{i1}(X,Y,Z)}{P_{i2}(X,Y,Z)} \qquad y_i + S_{0\,ij} = \frac{P_{i3}(X,Y,Z)}{P_{i4}(X,Y,Z)}$$

Equation 3.8

$$\begin{aligned}
P^{c}_{i1} &= (a_1 - b_1 L_0) + (a_2 - b_2 L_0)\,Y + (a_3 - b_3 L_0)\,X + (a_4 - b_4 L_0)\,Z \\
&+ (a_5 - b_5 L_0)\,YX + (a_6 - b_6 L_0)\,YZ + (a_7 - b_7 L_0)\,XZ \\
&+ (a_8 - b_8 L_0)\,Y^2 + (a_9 - b_9 L_0)\,X^2 + (a_{10} - b_{10} L_0)\,Z^2 \\
&+ (a_{11} - b_{11} L_0)\,XYZ + (a_{12} - b_{12} L_0)\,Y^3 + (a_{13} - b_{13} L_0)\,YX^2 \\
&+ (a_{14} - b_{14} L_0)\,YZ^2 + (a_{15} - b_{15} L_0)\,Y^2X + (a_{16} - b_{16} L_0)\,X^3 \\
&+ (a_{17} - b_{17} L_0)\,XZ^2 + (a_{18} - b_{18} L_0)\,Y^2Z + (a_{19} - b_{19} L_0)\,X^2Z \\
&+ (a_{20} - b_{20} L_0)\,Z^3
\end{aligned}$$

Equation 3.9

$$\begin{aligned}
P^{c}_{i3} &= (c_1 - d_1 S_0) + (c_2 - d_2 S_0)\,Y + (c_3 - d_3 S_0)\,X + (c_4 - d_4 S_0)\,Z \\
&+ (c_5 - d_5 S_0)\,YX + (c_6 - d_6 S_0)\,YZ + (c_7 - d_7 S_0)\,XZ \\
&+ (c_8 - d_8 S_0)\,Y^2 + (c_9 - d_9 S_0)\,X^2 + (c_{10} - d_{10} S_0)\,Z^2 \\
&+ (c_{11} - d_{11} S_0)\,XYZ + (c_{12} - d_{12} S_0)\,Y^3 + (c_{13} - d_{13} S_0)\,YX^2 \\
&+ (c_{14} - d_{14} S_0)\,YZ^2 + (c_{15} - d_{15} S_0)\,Y^2X + (c_{16} - d_{16} S_0)\,X^3 \\
&+ (c_{17} - d_{17} S_0)\,XZ^2 + (c_{18} - d_{18} S_0)\,Y^2Z + (c_{19} - d_{19} S_0)\,X^2Z \\
&+ (c_{20} - d_{20} S_0)\,Z^3
\end{aligned}$$

Equation 3.10

3.2.4 3D-Affine Model

Similar to RFMs, the affine projection model does not directly utilize sensor or exterior orientation parameters. Instead, the use of an empirical model based on parallel projection is justified due to the narrow FOVs (Okamoto 1992; Okamoto et al., 1999) for commercial high-resolution satellites, such as 0.98° for IKONOS and 2.1° for QuickBird.

To solve for an affine model bundle adjustment, an 8 parameter linear transformation for each image can be computed, as expressed in equation 3-11. The parameters account for 2 translations, 3 rotations and 3 independent scaling and skew distortions.

$$x = C_1 + C_2 X + C_3 Y + C_4 Z$$

$$y = C_5 + C_6 X + C_7 Y + C_8 Z$$

Equation 3.11

As the FOV of the linear array sensor becomes small, high correlations develop between the exterior orientation parameters and the bundle of rays effectively approaches a skew parallel projection. Fraser & Yamakawa (2004) have pointed out that the geometry of a cylindrical projection system (such as UTM) closely matches that of imaging the curved surface of the earth with a pushbroom scanner. Based on test data using Cartesian, geographic and UTM coordinate systems, the UTM coordinate system is reported as the optimal reference coordinate system for the affine sensor orientation model and its assumption of a parallel imaging plane. This is significant for this study since all mapping in MOMRA is based on UTM system. Similar to the DLT model, the performance of the affine model also depends on the distribution of GCPs. The model requires a minimum of four GCPs to solve for the 8 unknown transformation parameters. The affine model represents an abbreviated RPC model comprising only the first-order coefficients. It has been shown to produce similar levels of geopositioning accuracy as RPCs for reverse scanned imagery (Fraser and Yamakawa, 2004). However, time-variant parameters are required to manage the non-linear, dynamic pointing angle variations inherent in forward scanned imagery (Jacobsen, 2006).

3.2.5 Comparison and evaluation of presented models

Based on the above discussion of the various mathematical models available for processing HRSI to derive reliable map data, it can be concluded that the issue of georeferencing the HRSI has satisfactorily been resolved to a degree that pixel-level accuracies can now be achieved. Consequently, additional research effort in refining these models is not called for. It is, however, of considerable interest for this study to assess which model is best suited for the terrain and the environmental conditions in Saudi Arabia. Clearly, the bias corrected RPCs supplemented with well distributed GCPs will provide the highest geometric accuracy for large scale mapping. However, it will be necessary to explore which approach can practically be implemented in a map production environment to automate the selection of existing control data for georeferencing of the recently acquired satellite imagery for updating the existing map database. As stated in Section 1.4, the primary objective of this research study is to use existing orthorectified aerial image information instead of traditional ground control for the orthoprojection of new satellite imagery in order to automate and thus speed up as much as possible the whole process. Since this will require automated matching of HRSI with existing digital orthoimagery, the image matching strategy and methodology are included in this Chapter. The actual approach for processing HRSI and the areas for this practically oriented research study are discussed in the following Chapter 4.

3.3 Image matching strategy and approach

Stereo photogrammetry relies entirely on the measurement of conjugate points in two or more overlapping images. Such measurements are currently performed automatically in digital photogrammetry through image matching. Consequently, it is necessary to explore how existing image matching methods and strategies can be useful in automated georeferencing of new satellite imagery.

Aerial imagery is normally acquired for photogrammetric mapping with 60 percent or larger overlap in the flight

direction and with 30 percent or larger overlap across the direction of flight. In processing such aerial imagery the problem of image matching can be stated as follows (Schenk, 1999):

1. Select a matching entity in one image;
2. Find its corresponding entity in other overlapping image(s);
3. Compute the 3-D (or 2-D) location of the matched entity in object space;
4. Assess the quality of the match.

The second step presents the biggest challenge due to the fact that image matching. in general, is not a well-posed problem because it often violates the essential requirements that (i) a solution exists, (ii) the solution is unique, and (iii) the solution depends continuously on the initial data (Schenk, 1999). In the case of overlapping aerial imagery, no solution may exist due to occlusion or ambiguous solutions may exist due to poor texture. Consequently, a crucial challenge is how image matching is made well-posed. This problem has routinely been solved in automated image matching of overlapping aerial imagery by using approximations and enforcing constraints based on known geometry. Table 3-2 lists the strategic approach on which the common image matching methods are based.

Matching Method	Similarity Measure	Matching Entities
area-based	correlation, least squares	gray levels
feature-based	cost function	edges, regions
Symbolic	cost function	symbolic description

Table 3-2: Relation between common matching methods and matching entities (after Schenk, 1999)

In spite of the geometric distortions in the two images being matched due to any local scale difference, or due to orientation parameters or due to image displacement caused by terrain relief, the area-based methods are widely and successfully being used in routine digital photogrammetric map production practice. In Automated Aerial Triangulation (AAT), the mensuration of the tie points is initially based on the maximum value for the normalized correlation coefficient which is often further refined through least squares matching. The ease with which airborne GNSS and IMU data can be acquired during aerial imaging missions is greatly helpful in more accurately defining the image footprints, and consequently, significantly reduces the necessary search radius for matching conjugate entities.

The processing of digital aerial imagery for the production of Digital Surface Models (DSM) has been completely automated through image matching like least square matching (LSM), pixel base matching with dynamic programming (DP) and semiglobal matching (SGM). Semiglobal matching is reported to be more time consuming as compare to DP, but the DSM from SGM is comparatively better as the one from DP (Alobeid et al., 2011). The overlapping imagery captured with aerial frame cameras is often transformed to a normalized set of conjugate images before matching them along epipolar lines. This pre-processing step presents an elegant example of the use of geometric constraint, thereby reducing a 2-D matching problem to a much faster 1-dimensional matching along epipolar lines. But it requires the parameters of relative orientation, which in the current problem are not available.

3.3.1 Matching of HRSI with aerial imagery

This research study proposes to use existing aerial imagery that has already been georeferenced accurately, such as an orthophoto, to serve as control for the orthoprojection of a more recently acquired satellite image instead of using ground control points. This amounts to multi-scale, multi-season and of course to multi-sensor image matching; a brief discussion of these terms follows.

3.3.2 Multi-scale images

We perceive objects in the physical world as meaningful entities only over certain ranges of scale. A simple example is the concept of a branch of a tree, which makes sense only when viewed from a few centimeters to a few meters. It becomes a totally meaningless concept at the nanometer or the kilometer level. The fact that objects appear in different ways depending on the scale of observation has important implications in our efforts to describe them. Therefore, the scale concept and the notion of multi-scale representation are of crucial importance; this is well understood in the field of cartography where maps are produced at different levels of abstraction.

The computer community in its efforts for representing image data and the multi-scale nature of it has developed a general framework for multi-scale representation, called "scale space theory" (Witkin, 1983; Koenderink, 1984). A scale space consists of a series of representations of a signal, at resolutions ranging from the original down to some arbitrary minimum, parameterized by a scale factor. As the scale is decreased, the amount of detail in the signal is reduced (Lindeberg, 1994).

An important property of scale space is that no new details are introduced into the signal as the scale is reduced. It has been shown (Yuille and Poggio, 1986) that the only operator that does not introduce false details is the Gaussian and its derivatives. For Gaussian filtering, the scale factor is the standard deviation of the kernel.

Image pyramids, commonly used in digital photogrammetric data processing are an example of scale space. Although Gaussain filtering is the most theoretically accepted method, in most production systems image pyramids are formed by some filtering and subsampling.

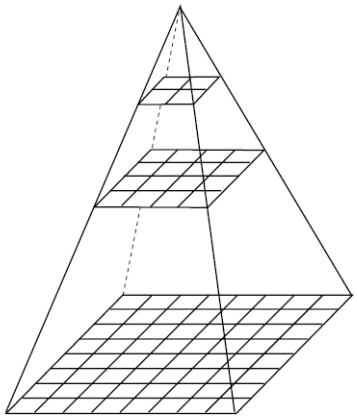

Figure 3-2: A pyramid representation is obtained by successively reducing the image size by combined smoothing and subsampling (after Lindberg, T., 1994)

3.3.3 Multi-season images

A digital image is a regular array of pixels and is described in terms of its geometry and its radiometry. The geometry of an imaged terrain scene is predominantly determined by the geometric design of the imaging sensor and its spatial location and attitude in relation to the scene. The radiometry, viz the variation and the distribution of the image intensities across the image is a function of many variables such as:

- the spectral and spatial capabilities of the imaging sensor, e.g. vignetting
- the strength and the spectral characteristics of the incident electromagnetic energy
- the orientation (the angle of incidence with imaged surface normal)
- the reflectance of the surface objects
- Prevailing environmental conditions (clouds, haze, dust, etc.)

The above factors that significantly affect the image intensity distribution in the scene form the very basis for most remote sensing applications such as land cover classification, etc. Many such remote sensing applications require that multi-season imagery be acquired under varying weather and illumination conditions at different times during the year. (Rosnell et al., 2011; Dana et al., 2008).

The large variations in the image texture in images of the same terrestrial scene create very serious hindrances in our ability to successfully match these images. For example, in an effort to obtain stereo coverage some HRS sensors can point downwards or obliquely to one side so that the area of interest is covered on different passes. The disadvantage of this method is that there is a time interval between images during which land cover and illumination conditions may have changed. Current high resolution satellite sensors are "agile" that have a single telescope that can be oriented rapidly to enable fore and aft overlapping images that are obtained on a single pass within a few minutes of each other (Dowman et al., 2012).

3.3.4 Multi-sensor images

Currently a large number of earth observation satellites are operational. Each of them with different spectral, spatial, and radiometric characteristics. There is an increasing interest in combining the multi-sensor image data of varying spectral, spatial and temporal resolution since it provides a more complete view of the observed objects. Therefore, for the full exploitation of increasingly sophisticated multisource data, advanced analytical and numerical data fusion techniques are being developed (Shen 1990). The primary aim of image fusion is to integrate different data in order to obtain more information than can be derived from each of the single sensor data alone (Pohl and van Genderen, 1998).

With the increase in the number of images collected every day from different sensors, the need for automated registration of multi-sensor images has equally increased. It is a classical problem in several image processing applications where it is necessary to match two or more images of the same scene (Fonseca and Manjnath, 1996).

3.4 Selection of matching method for experiment

The above discussion clearly indicates that in order to perform the matching of HRSI to include GeoEye-1 imagery of 50-cm GSD, IKONOS-2 imagery of 1.0-m GSD and SPOT-5 imagery of 2.5-m GSD, obtained between 2008 and 2010 with existing orthophoto at 50-cm GSD, produced from aerial imagery flown in 2005, we face the combined challenge of matching multi-sensor, multi-scale and multi-season imagery, Under these constraints, it becomes quite clear that the area based and the feature based algorithms routinely used for matching aerial imagery in photogrammetric map data processing are not suitable. Instead, the solution to the problem in hand must be sought in the field of computer vision which seeks solutions to more demanding image matching tasks such as object recognition and manipulation.

A study of the computer vision literature led to the method for extracting distinctive invariant features from images that can be used to perform reliable matching between different views of an object or scene. The features are invariant to image scale and rotation, limited change in 3D viewpoint, noise, and change in illumination and are shown to provide robust matching across a substantial range of affine distortion. This approach has been named the Scale Invariant Feature Transform (SIFT), as it transforms image data into scale-invariant coordinates relative to local features (Lowe, 2004).

3.4.1 SIFT Algorithm:

A large number of features can be extracted from typical images with the SIFT algorithm. Also the cost of extracting these features is minimized by taking a cascade filtering approach in which the more costly operations are applied only at locations that pass an initial test. The feature extraction and detection process in SIFT consists of

1. Scale-space extrema (minima and maxima) detection
2. Key point localization
3. Orientation assignment
4. Generation of key point descriptors.
5. Matching of the key point descriptors

It was shown by Koenderink (1984) and Lindeberg (1994) that under reasonable assumptions, the only possible scale-space kernel is the Gaussian function. Accordingly, the scale space is defined as a function, L(x,y,σ),that is produced from the convolution of a variable-space Gaussian $G(x, y, \sigma)$, with an input image $I(x, y)$:

$$L(x,y,\sigma) = G(x,y,\sigma) * I(x,y), \quad \text{Equation 3.12}$$

Where *is the convolution operation in x and y, and

$$G(x,y,\sigma) = (1/2\pi\sigma^2)\, e^{-(x2+y2)/2\sigma 2} \quad \text{Equation 3.13}$$

To efficiently detect stable keypoint locations in scale space, Lowe (1999) has proposed using scale-space extrema in the difference-of-Gaussian (DoG) function convolved with the image, $D(x, y, \sigma)$, which can be computed from the difference of two adjacent scales separated by a constant scale factor k:

$$D(x,y,\sigma) = (G(x,y,k\sigma) - G(x,y,\sigma)) * I(x,y)$$
$$= L(x,y,k\sigma) - L(x,y,\sigma) \quad \text{Equation 3.14}$$

This is a particularly efficient function to compute since the progressively smoothed (or blurred) images need to be computed in any case for the scale space feature description, and D can therefore be computed by simple image subtraction, as depicted in Figure 3-3. In addition, Lindeberg (1994) showed that the normailization of the Laplacian with the facor σ^2 is required for true scale invariance and the DoG function provides a close approximation to the scale-normalized Laplacian of Gaussian, $\sigma^2\nabla^2 G$, and therefore,

$$G(x, y, k, \sigma) - G(x, y, \sigma \approx (k-1)\sigma^2\nabla^2 G$$

Equation 3.15

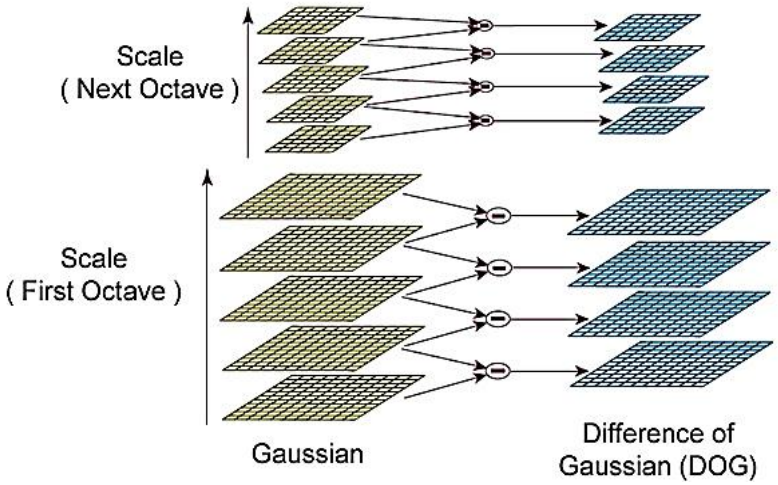

Figure 3-3: Process of DoG filtering in SIFT feature extraction algorithm (after Lowe, 2004)

Figure 3-3, shows that for each octave of scale space, the initial image is repeatedly convolved with Gaussians to produce the set of scale space images shown on the left. Adjacent Gaussian images are subtracted to produce the difference-of-Gaussian images on the right. After each octave, the Gaussian image is down-sampled by a factor of 2, and the process repeated.

3.4.1.1 Key point detection

The key points are identified as local maxima or minima of the DoG images across the scales. In order to determine the local maxima and minima of D (x,y,σ),each sample point is compared to its eight neighbors in the current image and nine neighbors in the scale above and below as marked with circles in Figure 3-4.

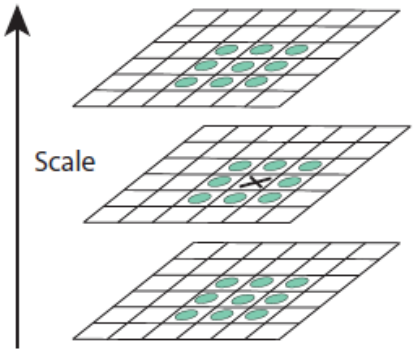

Figure 3-4: Maxima and minima of the DoG images are detected by comparing a pixel (marked with X) to its 26 neighbors in 3x3 regions at the current and adjacent scales (after Lowe, 2004)

If the pixel is a local maximum or minimum then it is selected as a candidate key point. For each such point, interpolation of nearby data is used to accurately determine its position, key points with low contrast are removed and responses along edges are eliminated.

3.4.1.2 Orientation assignment.

Finally, each key point is assigned an orientation. By assigning a consistent orientation to each keypoint based on local image properties, the keypoint descriptor can be represented relative to this orientation and therefore achieve invariance to image rotation. The scale of the keypoint is used to select the Gaussian smoothed image, L, with the closest scale, so that all computations are performed in a scale-invariant manner. For each image sample, L(x, y), at this scale, the gradient magnitude, m(x, y), and orientation, θ(x, y), is pre-computed using pixel differences:

$$m(x,y) = [(L(x+1,y) - L(x-1,y))^2 + (L(x,y+1) - L(x,y-1))^2]]^{1/2}$$
$$\theta(x,y) = \tan^{-1}((L(x,y+1) - L(x,y-1))/(L(x+1,y) - L(x-1,y))) \quad \text{Equation 3.16}$$

An orientation histogram is formed from the gradient orientations of sample points within a region around the key point. The orientation histogram has 36 bins covering the 360 degree range of orientations. Each sample added to the histogram is weighted by its gradient magnitude and by a Gaussian-weighted circular window with a radius that is 1.5 times that of the scale of the key point.

3.4.1.3 Local image descriptor

The previous operations have assigned an image location, scale, and orientation to each keypoint. These parameters impose a repeatable local 2D coordinate system in which to describe the local image region, and therefore provide invariance to these parameters. The next step is to compute a descriptor for the local image region that is highly distinctive yet is as invariant as possible to remaining variations, such as change in illumination or 3D viewpoint.

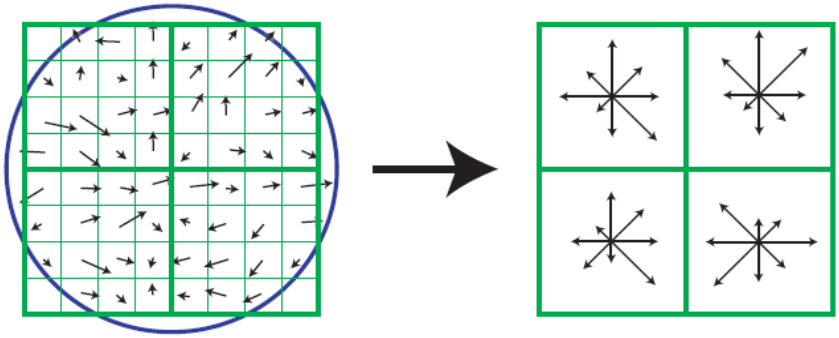

Image gradients Key point descriptor

Figure 3-5: Feature representation by creating key point descriptors (according to Lowe, 2004)

This is achieved by creating a keypoint descriptor by first computing the gradient magnitude and orientation at each image sample point in a region around the key point location, as shown in Figure 3-5 on the left. These are weighted by a Gaussian window, indicated by the overlaid circle. These samples are then accumulated into orientation histograms summarizing the contents over 4x4 subregions, as shown on the right, with the length of each arrow corresponding to the sum of the gradient magnitudes near that direction within the region. The figure on the right shows a 2x2 descriptor array computed from an 8x8 set of samples. Lowe (2004) reported the use of 4x4 descriptors computed by a 16x16 sample array. The histograms contain 8 bins each which leads to a SIFT feature vector with 4 x 4 x 8 = 128 elements. This vector is normalized to enhance invariance to changes in illumination.

3.4.1.4 Matching of keypoint descriptors

Key points determined individually for any image can be matched with the corresponding key points determined in another image. The correspondence of the key points is determined by the lowest root mean square (RMS) or lowest mean absolute difference (MAD) of the sum of gradients in the 8 main directions of the 4x4 sub-matrix of the key-points together with some specified conditions. The matching of the corresponding points can be constrained by coordinate differences, maximal value for the RMS or MAD and maximal y-parallaxes and be supported by the histogram of magnitudes in 36 direction groups determined earlier. If the corresponding image position difference between the two images exceeds a specified threshold, the RMS or MAD is increased for this special point combination by the chosen penalty. If the frequency distribution of the gradient orientation in the 16x16 sub-matrix agrees in a satisfactory manner, the RMS or MAD is reduced by subtracting a reward. The satisfactory correspondence of the frequency distribution of the gradient orientation is specified by the fact that the orientation group (36 orientation groups for 360°) with the maximal sum of gradient magnitudes corresponds with one group of extreme values corresponds to the second file with a maximal difference of the group index of 1. (Jacobsen, 2012).

3.5 SURF Algorithm

Inspired by the approach used in SIFT, Bay et al. (2006) presented a modified scale- and rotation-invariant detector and descriptor that is equally repeatable and robust but can be computed much faster and appropriately, called it Speeded-Up Robust Features (SURF). Similar to SIFT, the SURF algorithms is comprised of the following two consecutive steps:

1. Interest point detection
2. Interest point description and matching.

3.5.1 Interest point detection

SURF locates features using an approximation to the determinant of a basic Hessian-matrix, selected for its stability and repeatability. This permits the use of integral images (Viola and Jones, 2001) that significantly reduces the computation

time. An ideal filter would construct the Hessian by convolving the second order derivatives of a Gaussian of a given scale σ with the input image. This is approximated by replacing the second order Gaussian filters with a box filter, which can be evaluated extremely efficiently using integral images. An integral image, also called "summed area table" is an intermediate representation for the image and contains the sum of gray scale pixel values of image. The entry of an integral image I_I at a location (x, y) represents the sum of all pixels in the input image I within a rectangular region formed by the origin and the location (x, y).

$$I_I(x,y) = \sum_{i=0}^{x}\sum_{j=0}^{y} I(i,j)$$

Equation 3.17

Once the integral image has been computed, it takes only four lookups and three additions to sum up the intensities over any arbitrarily-sized, axis-aligned 2D region as shown in Figure 3-6. This is important as the SURF uses big filter sizes.

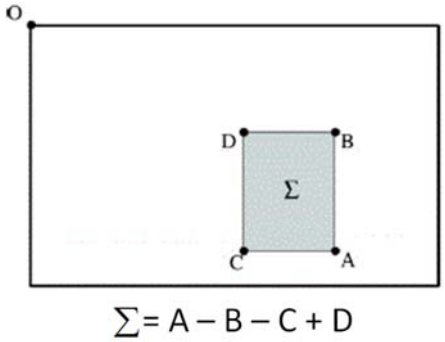

Figure 3-6: Using integral images, the sum of intensities is obtained through 3 additions for a rectangular area, independent of its size. (after Bay et al., 2006)

SURF uses Hessian matrix to detect blob-like structures at locations where the determinant is maximum. The scale selection is also based on the determinant of the Hessian. Given a point **x**= (x, y) in an image I, the Hessian matrix H (x, σ) in x at scale σ is defined as:

$$H(x,\sigma) = \begin{pmatrix} L_{xx}(x,\sigma) & L_{xy}(x,\sigma) \\ L_{xy}(x,\sigma) & L_{yy}(x,\sigma) \end{pmatrix}$$

Equation 3.18

Where $L_{xx}(x,\sigma)$ is the Laplacian of Gaussian (LoG) of the image and is the convolution of the Gaussian second order partial derivative $\frac{\partial^2}{\partial x^2} g(\sigma)$ with the image *I* in point ***x,*** and similarly for $L_{xy}(\boldsymbol{x}, \sigma)$ and $L_{yy}(\boldsymbol{x}, \sigma)$.

As pointed out by Lindeberg (1990), Gaussians are optimal for scale–space analysis but for practical reasons they have to be discretized and cropped. While the SIFT algorithm approximates the LoG with the Difference of Gaussian, the SURF algorithm approximates the Hessian matrix with box filters. Using a 9 x 9 box filter with σ = 1.2, the Gaussian second order partial derivatives Lyy and Lxy, discretised and cropped, are shown in Figure 3-7. In the above equation for the Hessian matrix, denoting the corresponding approximate Laplacians as Dxx, Dyy and Dxy, the determinant of the Hessian is approximated as:

$$\det(H_{\text{approx}}) = D_{xx}D_{yy} - (w D_{xy})^2$$

Equation 3.19

The w in the above equation represents relative weight of the filter responses and is used for balancing the Hessian determinant and, for the 9 x 9 filter with σ = 1.2, is approximately equal to 0.9. This is the lowest scale or the highest resolution used by Bay et al. (2006). The Laplacian of Gaussian is graphically illustrated in Figure 3-7 and the arrows point to the resulting corresponding approximated element.

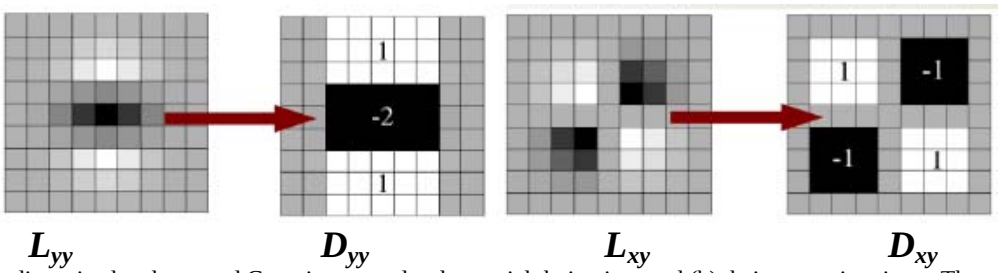

Figure 3-7: The discretized and cropped Gaussian second order partial derivatives and (b) their approximations. The gray regions are equal to zero. (after Bay et al., 2006)

Similar to SIFT, the SURF finds interest points at different scales. However, due to the use of box filters and integral images, there is no need to apply the same filter to a previously filtered layer, but instead can apply box filters of increasing size at exactly the same processing cost directly on the original image. Therefore, the scale space is analyzed by increasing the filter size rather than iteratively reducing the image size, as illustrated in Figure 3-8.

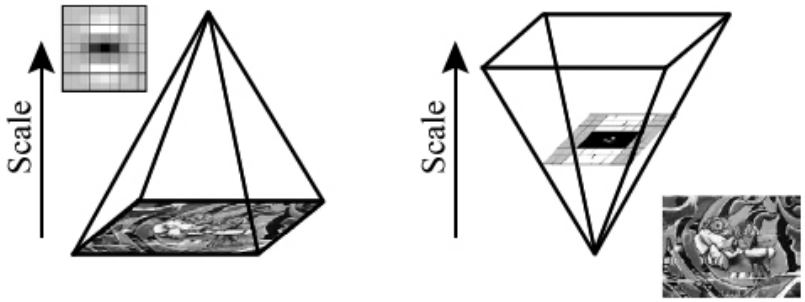

Figure 3-8: Instead of reducing the image size (left), the use of integral images allows up-scaling of the filter (right) at constant processing cost. (after, Bay et al., 2008)

SURF divides the scale space into octaves; an octave representing a series of filter response maps resulting from convolving the same input image with filters of increasing size. Each octave is subdivided into a constant number of scale levels that encompass a scaling factor of 2. Bay et al. (2006) compute three octaves with the option of going to four octaves. They derive their size 9 x 9 filter as the best box-filter approximation of the second-order derivatives of a Gaussian with scale $\sigma = 1.2$ and compute the scale associated with the rest of the filters based on the ratio of their size to that of the base filter. Due to the discrete nature of integral images, the minimum scale difference between two subsequent scales depends on the positive or negative lobes of the partial second order derivative in the direction of derivation, x or y, which Bay et al. (2006) set to a third of filter size length; 3 for the 9 x 9 filter. In order to keep the filter size uneven to ensure the presence of the central pixel, this size must be increased by a minimum of 2 pixels for two successive scale levels. The resulting growth in the filter size is illustrated in Figure 3-9.

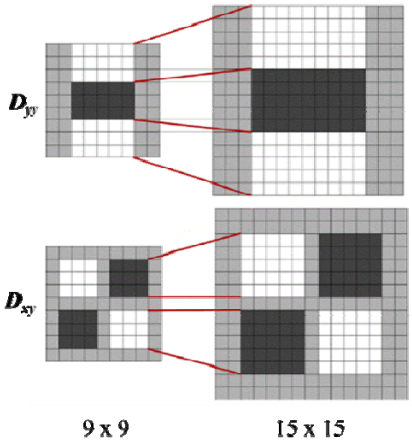

Figure 3-9: Filters D_{yy} and D_{xy} for two successive scale levels 9 x 9 and 15 x 15 (After Bay et al., 2008).

The scale space is constructed using filters starting with size 9 x 9 followed by sizes 15 x 15, 21 x 21 and 27 x 27. The filter sizes for the second octave are 15, 27, 39, and 51. A third octave is computed with the filter sizes 27, 51, 75, 99. If the size of the original image is still larger than the corresponding filter sizes, the analysis is continued with the fourth octave using filter sizes 51, 99, 147, 195. More octaves may be used but the number of detected interest points per octave decays very rapidly (Bray et al., 2006). The filter side lengths for the first three octaves are graphically represented in Figure 3-10. The octaves overlap to ensure full coverage of each scale.

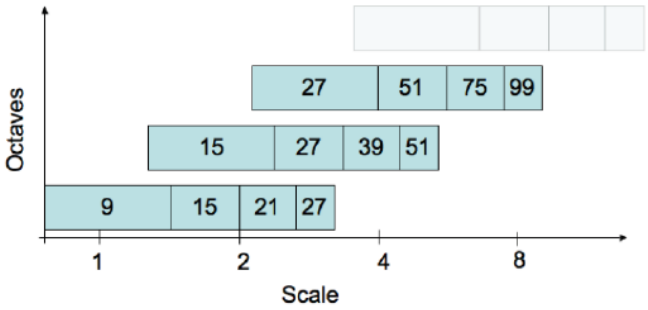

Figure 3-10: Graphical representation of the filter side lengths for first three octaves. Scales are represented by the logarithmic horizontal axis. (After Bay et al., 2008)

Once the Hessian determinant values have been computed for a triplet of scales, local maxima over a given threshold become interest points. In order to localize the interest points in the image and over scales, a non-maximum suppression in a 3 x 3 neighborhood is applied (Neubeck and Van Gool, 2006). The non-maximum suppression is applied within the same blob response map as well as with the blob response map above and below the image in scale space for each octave. Consequently, only the middle two blob response maps for each octave are used. The location x0 of each interest point is then refined to sub-pixel accuracy via (Brown and Lowe, 2002):

$$\hat{x} = x_0 - \left(\frac{\partial^2 H}{\partial x^2} \right)^{-1} \frac{\partial H}{\partial x}$$

Equation 3.20

Where $\boldsymbol{x} = (x, y, \sigma)^T$ are scale space coordinates and H is the magnitude of the Hessian determinant.

The derivatives of H are computed around x_0 via finite differences.

3.5.2 Interest point description and matching

SURF describes the intensity distribution within the interest point neighbourhood, similar to the gradient information extracted by SIFT. In order to be invariant to image rotation, SURF identifies a dominant orientation for the interest points. For this purpose, the Haar wavelet responses are calculated in x and y direction within a circular neighbourhood of radius 6s around the interest point; s is the scale at which the interest point was detected. The wavelets are scale dependent and set to a side length of 4s. The used filters are shown in Figure 3-11.

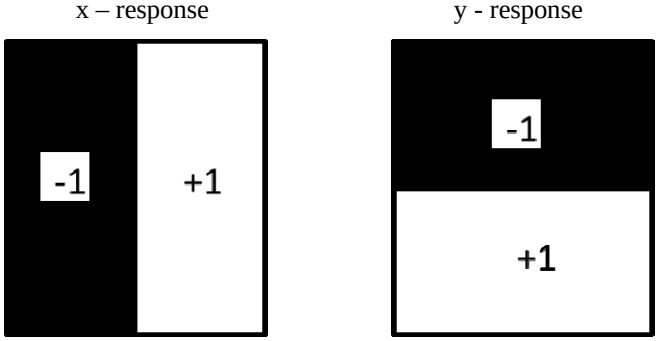

Figure 3-11: Haar wavelet filters to compute the responses in x and y direction (after Bay, H. et al., 2008)

The wavelet responses are calculated and weighted with a Gaussian (σ = 2s) centered at the interest point and used as x and y values in a Cartesian map. The dominant orientation is estimated by rotating a wedge of 60 degrees around the circle and choosing the direction of maximum total weight, as seen in Figure 3-12.

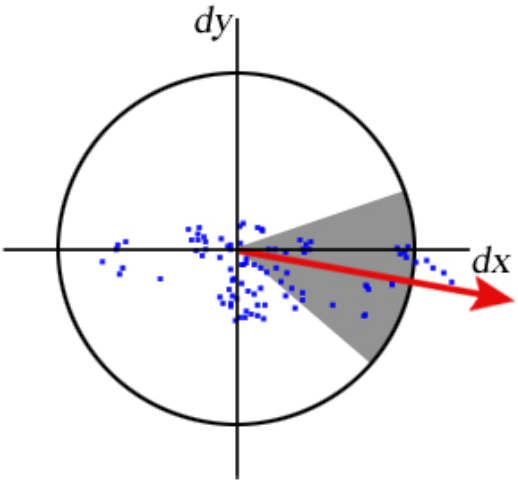

Figure 3-12: Dominant orientation assignment within a circular neighbourhood around interest point (after Bay, H. et al., 2008)

The SURF descriptor is based on the sum of Haar wavelet responses. The interest region is split into 4 x 4 square sub-regions oriented along the calculated dominant orientation, each with 5 x 5 regularly spaced sample points where Haar wavelet response dx and dy (along rectangular axes) are calculated (see Figure 3-13). The Haar wavelet responses are first weighted with a Gaussian (σ = 3.3) and summed up over each sub-region separately for dx and dy resulting in a feature vector of length32. In order to bring in information about the polarity of the intensity changes, the sum of the absolute values of the responses |dx| and |dy| are also summed. This results in the final feature vector length of 64. Finally, invariance to contrast is assured by normalizing the vector into unit length.

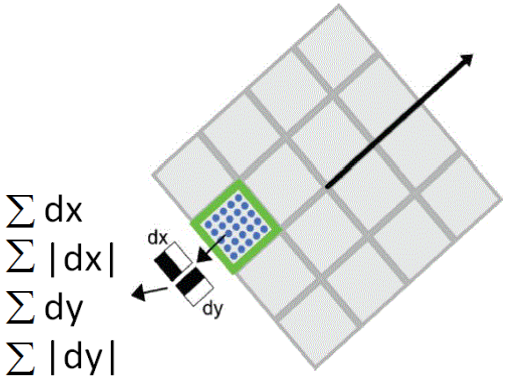

Figure 3-13: Partitioning of the interest area in sub-regions and aggregation of Haar wavelet responses relative to the orientation of the grid.(modified after Bay, H. et al., 2008)

The SURF approach proposed by Bay et al. (2006) uses the sign of the Laplacian (trace of the Hessian matrix) for the underlying interest point for fast indexing during the matching stage. No additional computational cost is involved because this information is already generated during the detection stage. Since the interest points are typically found at blob-type structures, the sign of the Laplacian distinguishes bright blobs on dark backgrounds from the dark ones on light background (Figure 3-14). This speeds up the matching process by comparing only those features which have the same type of contrast. Such minimal information allows for faster matching without reducing the descriptor's performance.

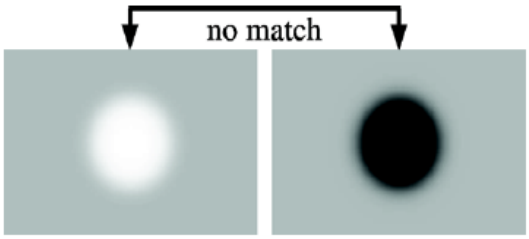

Figure 3-14: Interest points with different contrast are not considered for matching. (After Bay et al., 2008)

3.6 Concluding comments on image matching

Even though SIFT was the first algorithm proposed for scale-invariant image matching, the very rationale for the design of SURF algorithm was to speed up the matching process. In comparing SURF with SIFT algorithm, Juan and Gwun (2010) reported that SURF is much faster than SIFT. However, SIFT has superior performance against image rotation and illumination changes. While matching approximately georeferenced satellite imagery with precisely orthorectified aerial imagery, the rotation should not be a concern. Consequently, SURF has been selected as the most appropriate approach for use for this research study.

Chapter 4. Test Area and HRSI Coverage

As pointed out in Chapter 1, the primary objective of this research study is to assess the feasibility of using HRSI that is currently available for rapid topographic mapping to meet the following two distinct needs:

- Updating the existing photogrammetrically compiled large scale maps of those urbanized areas that have recently gone through rapid development and expansion, as an alternative to the lengthy and time-consuming current practice of photogrammetric mapping from aerial imagery.
- Delineating the parcels of land for areas for which only small scale maps at 1:50,000 scale currently exist, for the compilation of region-wide cadastral fabric to support the Cadastral registration program in the Kingdom of Saudi Arabia.

Accordingly, some experimental testing is called for to make this assessment. The test objectives, the selection of test areas and the testing experimental procedures are described in this chapter. The data collected during the experiments and the results obtained are described in the following Chapter 5.

4.1 Test Objectives

The tests must be designed to investigate the answers to the issues raised in Chapter 1. The tests should be designed to also include the following considerations:

i. The test should cover heavily urbanized areas as well as suburban areas where significant new development activity is concentrated.
ii. The test should include rural areas covering cultivated as well as non-cultivated land parcels for delineating the parcel boundaries.
iii. The test areas should be representative of the range of topography and landform typical for Saudi Arabia.
iv. The test should be based on the commonly used alternative models for mapping from HRSI and evaluate the need for any supplementary information such as GCPs, existing maps or orthophotos, etc. to enhance the accuracy of georeferencing of the resulting map data.
v. The testing should be carried out for mapping from a single HRS image and should be representative of the range of resolutions provided by current HRSI systems.
vi. The georeferencing accuracy of the map data resulting from the processing of HRSI should be checked through a well-designed set of Check Points.
vii. An important objective of the testing is to demonstrate what steps in the processing of HRSI can be fully or partially automated to enhance the mapping productivity.

4.2 Selection of HRSI

As discussed in chapter 2, satellite imagery with a wide ranging resolution and mapping capabilities is now available for exploitation. However, the choice of the satellite imagery for this research study has to be restricted to the imagery covering Saudi Arabia which can periodically and readily be procured in Saudi Arabia. Any uncertainty about the availability of the satellite imagery for an area of interest or lengthy procedures which may result in long delay in the procurement process would negate the very premise of this thesis.

In the Kingdom of Saudi Arabia, the King Abdul Aziz City for Science and Technology (KACST) operates a satellite receiving station and is responsible to provide imagery to all users in Saudi Arabia. MOMRA has been able to procure

SPOT-5 and IKONOS high resolution satellite imagery from KACST in the past. However on special request, KACST can also provide imagery from other HRSI systems such as GeoEye-1, etc. Most probably, KACST will be able to provide imagery that is available for general use from any existing satellite imaging systems or from those currently under development.

Besides the timely availability, an equally important relevant consideration is the cost of procurement of HRSI. The cost is an especially important consideration in the procurement of HRSI for this research study. Consequently, it was decided to procure the following satellite imagery coverage for the selected test sites.

a. SPOT-5 coverage at 2-5 m GSD
b. IKONOS coverage at 1-0 m GSD
c. GeoEye-1 or WorldView-2 coverage at 0.5-m GSD

Such an imagery dataset covers a significant spread in the geometric resolution (variation with a factor of 5) and permits the analysis of the range of accuracy with which map data can be derived from the processing of the high resolution satellite imagery.

4.3 Selection of Test Areas

In the light of the considerations outlined above, the selection of the Test areas was also influenced by additional practical considerations. The foremost consideration was to select areas that are easily accessible from Riyadh and already have a large amount of ground control and mapped data to serve as ground truth and check data. Accordingly, it was decided to use three separate sites to serve as Test Areas. The test areas are shown in Figure 4-1 against map image background to show the topography and the landform involved. This is followed by a brief description of each selected test area.

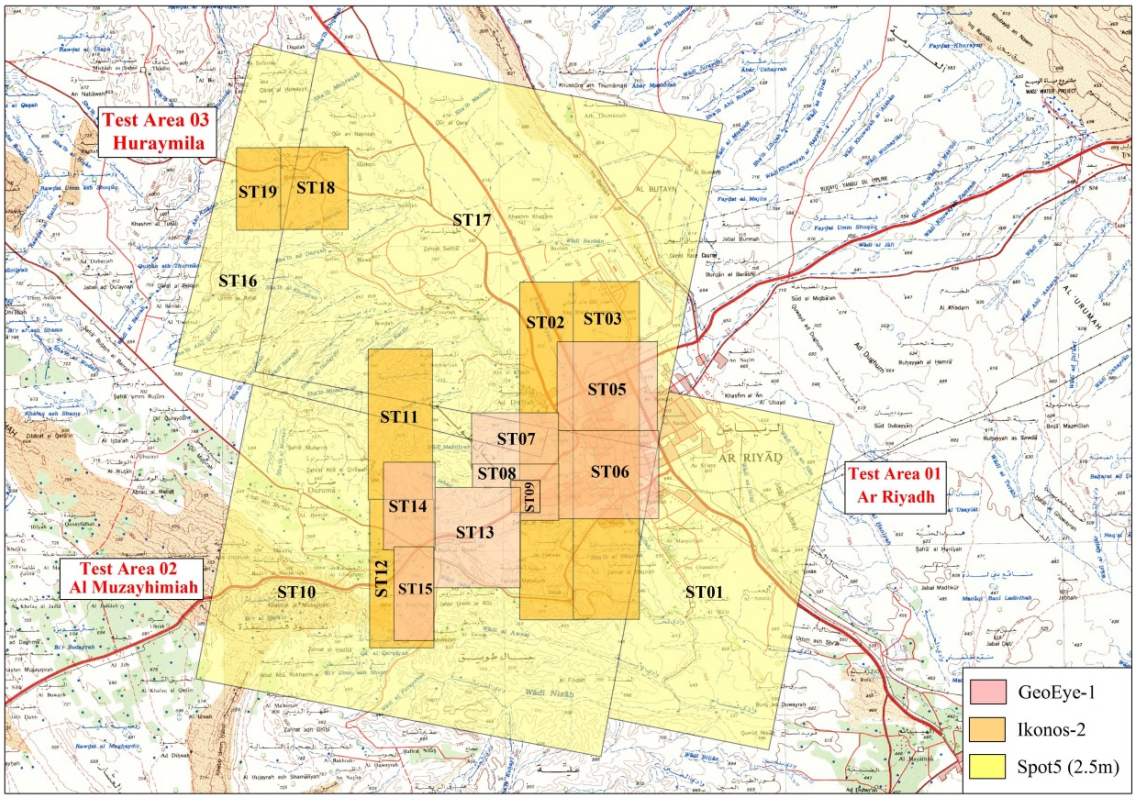

Figure 4-1: The location of the selected Test Areas is shown on satellite images against map background.

4.3.1 Test Area 1: Ar Riyadh

Riyadh lies in the great plateau area of Najd. This region is mainly rocky plateau interspersed by small, sandy deserts and isolated mountain clumps. Historically, from a large oasis in the plateau of Najd, Riyadh has been the capital of the Kingdom of Saudi Arabia since early 1930s and has experienced the most phenomenal urban growth and development during the past about four decades. The average altitude is around 650 meter above sea level.

The area selected for test mapping covers the densely urbanized south-western part of Riyadh Metropolis as well as the adjoining suburban area which is undergoing rapid new development. Its location in the same city as MOMRA and the rapid rate of urban growth as well as the availability of a large amount of ground control data provided the main impetus for selecting this site for testing. The topography does not significantly vary within the Test Area-1 as seen in Figure 4-1.

4.3.2 Test Area 2: Al-Muzahimiah

This site is located about 25 km south-west of Riyadh along an escarpment and includes several cultivated farm parcels. While the primary focus in the Test Area-1 is the high urban density, the Test Area-2 provides a significant variation in topography in a rural landscape. In addition, the easy accessibility from Riyadh and the availability of existing ground control and large scale map information influenced the choice of this test site, which is shown in Figure 4-1.

4.3.3 Test Area 3: Huraymila

Huyraymila is a small city with a population of about 10,000 and located around 90 Km from the capital, Riyadh, as shown in Figure 4-1. Surrounded with old style farms with a lot of palm trees, Huraymila presents a landscape ranging from acacia covered wadi to dramatic escapment and wide plains.

This site represents a typical mix of urban and rural landscape and is selected primarily due to the reason that detailed cadastral surveys have recently been completed for this area as the pilot project for the implementation of the Kingdom wide cadastral registration system. In addition, the availability of large scale maps and a wealth of ground control data make it an attractive test area.

4.4 Procurement of HRSI

As pointed out earlier, the most important considerations for the selection of HRSI coverage were the cost and the timely availability. Accordingly the procurement of the following satellite imagery coverage for the selected test sites was arranged.

a. SPOT-5 (June 2010) stereo coverage at 2.5 m GSD for Areas 1, 2 and 3
b. IKONOS-2 (January 2010) coverage at 1.0 m GSD for Area 1
c. GeoEye-1 (January 2010) coverage at 0.5 m GSD for Area 1 and (September 2010) for Area2

Sensor	**GSD** (m)	**Scene** (Sq Km)	**Cost / Scene** (Euro)	**Cost / Sq Km** (Euro)
GeoEye	0.5	225	4,500	20.00
IKONOS	1.0	121	1,883	15.56
SPOT-5	2.5	3,600	8,100	2.25

Table 4-1: HRSI Price List

While the procurement of the above SPOT-5, IKONOS-2 and GeoEye-1 coverage for the selected sites was being arranged, it was decided to also use some existing recent IKONOS-2 and GeoEye-1 coverage of the selected Test Areas to develop and test the proposed processing procedures using the commercial software currently available in MOMRA. The Test Areas and the satellite imagery coverage used in this study are tabulated in Table 4-2.

The series of experiments carried out in support of this study and the testing methodology are described in the following Chapter 5.

AREA	HRSI	Date of Imaging	Image Number	Ref. No.
Ar Riyadh	SPOT-5 (2.5 m)	13 Jun 2010	147-301	ST01
	IKONOS-2 (1 m)	09 Aug 2008	po_2411348_0000000	ST02
	IKONOS-2 (1 m)	09 Aug 2008	po_2411348_0010000	ST03
	IKONOS-2 (1 m)	01 May 2010	po_2418067_0000000	ST04
	GeoEye-1 (0.5 m)	09 Nov 2009	po_2415597_0000003	ST05
	GeoEye-1 (0.5 m)	09 Nov 2009	po_2415597_0000004	ST06
	GeoEye-1 (0.5 m)	20 Nov 2009	po_2415788_0000007	ST07
	GeoEye-1 (0.5 m)	20 Nov 2009	po_2415788_0000008	ST08
	GeoEye-1 (0.5 m)	01 May 2010	po_2418066_0000000	ST09
Al Muzahimiyah	SPOT-5 (2.5 m)	13 Jun 2010	146-301	ST10
	IKINOS-2 (1 m)	25 Nov 2008	po_2411975_0000001	ST11
	IKINOS-2 (1 m)	25 Nov 2008	po_2411975_0000002	ST12
	GeoEye-1 (0.5 m)	09 Nov 2009	po_2415598_0000003	ST13
	GeoEye-1 (0.5 m)	26 Nov 2009	po_2415858_0010001	ST14
	GeoEye-1 (0.5 m)	09 Jan 2010	po_2416389_0000000	ST15
Huraymila	SPOT-5 (2.5 m)	13 Jun 2010	144-300	ST16
	SPOT-5 (2.5 m)	13 Jun 2010	146-300	ST17
	IKONOS-2 (1 m)	28 Dec 2009	po_2416186_0010000	ST18
	IKONOS-2 (1 m)	28 Dec 2009	po_2417522_0000000	ST19

Table 4-2: HRSI used for test

Chapter 5. Test Methodology and Experiments

The fulfillment of the objectives of this study demands that a set of practical experiments be conducted to generate data that can be analyzed to assess the feasibility of the use of HRSI for rapid updating of the map data in Saudi Arabia. The design and the methodology used for such experiments carried out using satellite imagery listed in Table 4-2 are described in this Chapter. The data resulting from the experiments is presented and discussed in the following Chapter 6.

5.1 Experiment I: Georeferencing Accuracy

The objective of this Test is to evaluate the accuracy with which satellite image data can be georeferenced by exploiting the capability of a commercial satellite image processing software suite currently available in MOMRA. The aim is to seek answers to Questions No. 1 and No.2 posed earlier in Section 1.4.4. The first phase of this experiment is conducted entirely through interactive processing of the satellite imagery. This is followed by the second phase, carried out as Experiment IV, where the interactive role is replaced with automated processing. The test Experiment I was conducted in two parts. The processing steps involved in each part of the test are briefly described below.

5.1.1 Experiment I-A:

Step 1: Orthorectification of 0.5-m GSD GeoEye-1 imagery using existing DTM data based solely on the vendor supplied RPCs and without using any additional GCP data. This task was completed by employing the available Inpho OrthoMaster software. Once the satellite image input file, the related metadata file containing RPCs, and the DTM data file have been identified, the processing proceeds without further operator interaction if no ground control points are used. Consequently, this task easily lends itself to batch processing.

Step 2: Comparison of the coordinates of well identifiable image points that are properly distributed over the rectified satellite image with the coordinates of the corresponding image points (to serve as CPs) on an existing orthophoto map at 1:10 000 scale produced from 1:45 000 aerial photography with 0.5-m GSD. The selection and the measurement of the CPs were carried out manually and required considerable time and effort.

Step-3: Repeat Step-1 and Step-2 above with 1.0-m GSD IKONOS-2 imagery.

Step 4: Repeat Step-1 and Step-2 above with 2.5 m GSD SPOT-5 imagery.

5.1.2 Experiment I-B:

Step 1: Orthorectification of 0.5-m GSD GeoEye-1 imagery using existing DTM data based on the vendor supplied RPCs but supplemented with well identifiable GCPs distributed over the image scene, carried out using Inpho OrthoMaster software.

Step 2: Comparison of the coordinates of selected CPs measured on the georeferenced satellite orthoimage resulting from Step-1 above with the coordinates of the CPs derived from an existing orthophoto map at 1:10,000 scale produced from 1:45,000 aerial photography with 0.5-m GSD.

In order to investigate the influence of the number and the distribution of the GCPs on the georeferencing accuracy, the above step 1 and step 2 were performed three times, each time increasing the number of GCPs used for processing. The judicious selection of GCPs with optimal distribution over the image scene and their interactive measurement required considerable effort and operator time. This testing also covered all the three test areas that represent considerable landscape variation. In the case of the mostly urbanized Riyadh Area, a large number of GCPs and CPs could easily be selected. Accordingly, the test was performed with 5 GCP, 10 GCP and 15 GCP. As an example, the location and the

distribution of the 15 GCPs and 10 CPs used for the test on the GeoEye-1 image of the Riyadh Area (ST09) is shown in Figure 5-1. A sample of the typical features selected as GCPs and CPs are compiled in Figure 5-2.

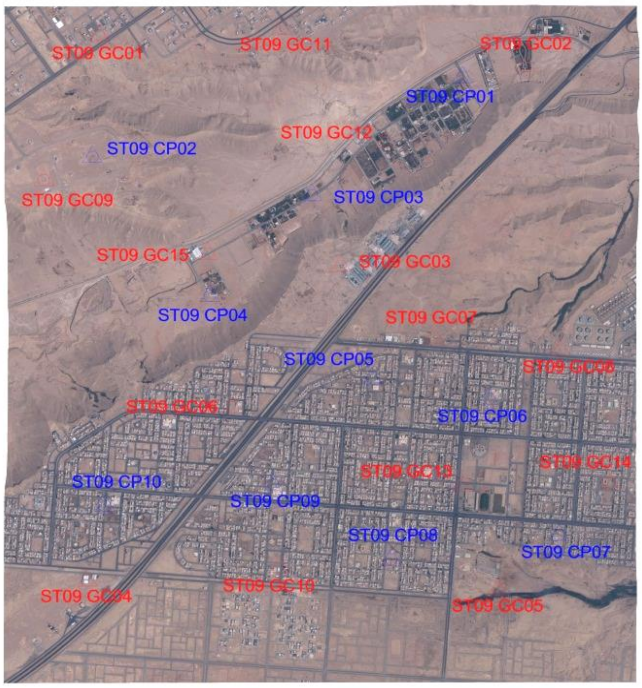

Figure 5-1: GCP (red) and CP (blue) distribution

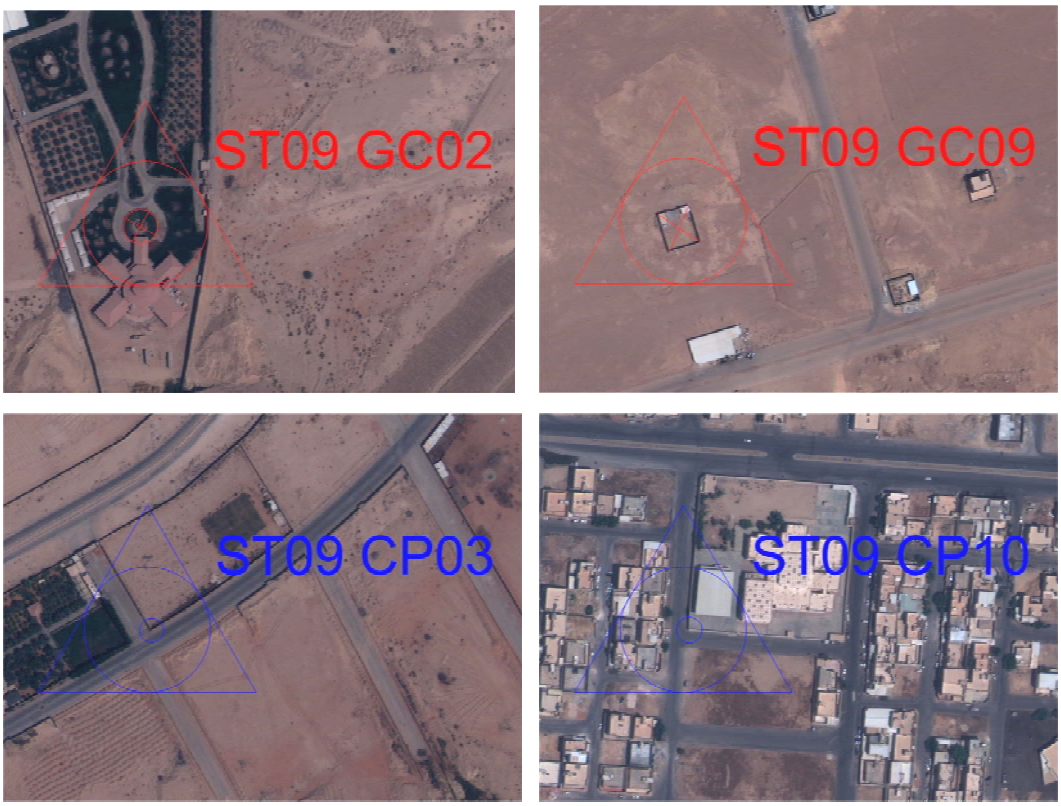

Figure 5-2: Typical features used as GCP (red) and as CP (blue)

The selection of suitable GCPs and CPs was much more challenging in the open and hilly terrain of the Al Muzahimiah Area, the GeoEye-1 coverage of which is shown in Figure 5-3. For this area, the Experiment 1-B had to be limited to the use of 5 GCP, 7 GCP and 10 GCP only.

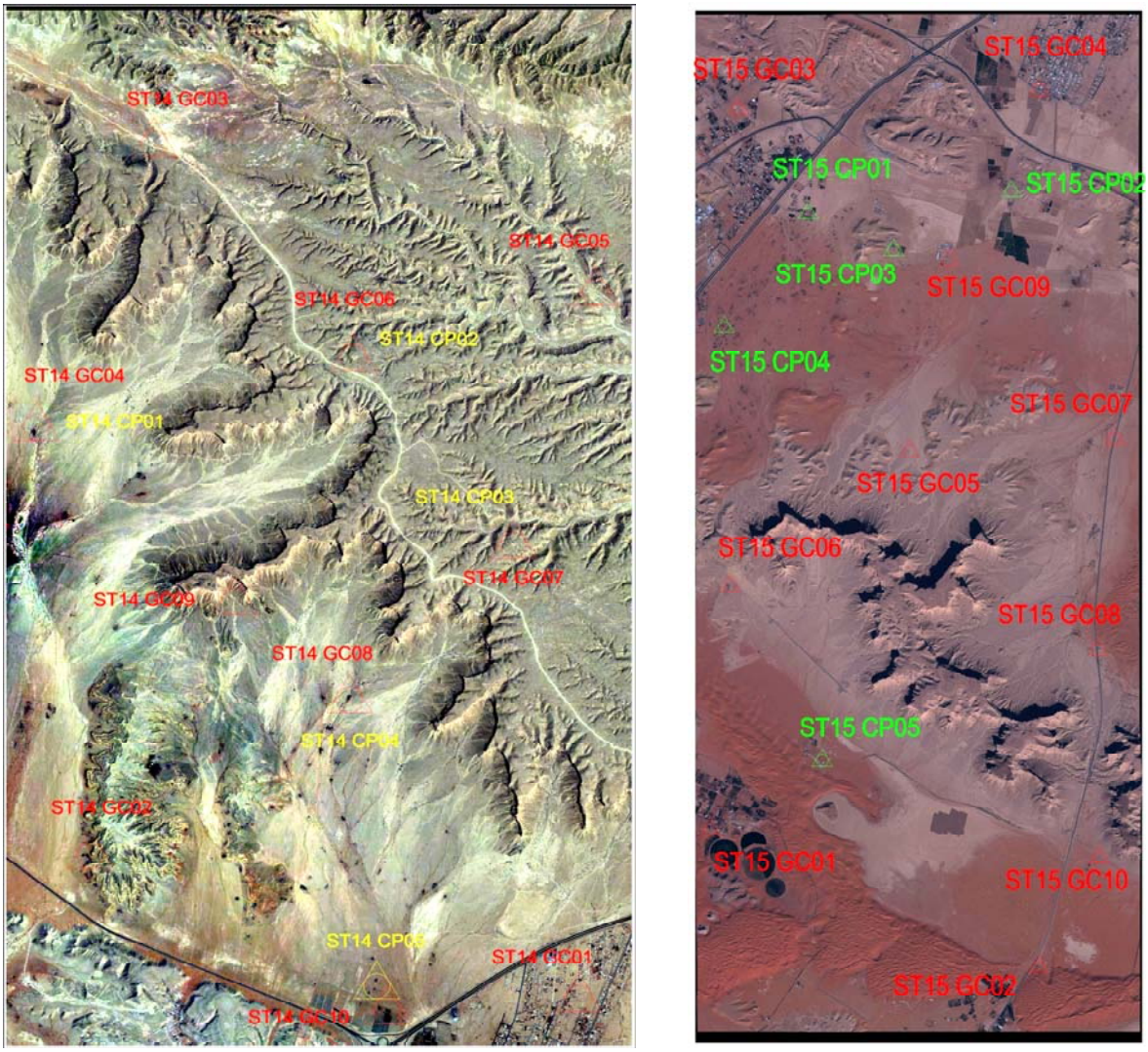

Figure 5-3: GeoEye-1 Coverage (ST14 and ST15) of the Al Muzahimiah Area; the GCPs are in red, the CPs are shown in yellow (ST14) and in green (ST15)

Step 3: Repeat the Step-1 and the Step-2 of the above Experiment 1-B on 1.0-m GSD IKONOS-2 imagery.

Step 4: Repeat the Step-1 and the Step-2 of the above Experiment 1-B on 2.5-m GSD SPOT-5 imagery.

5.2 Experiment-II: Mapping Accuracy

The objective of this test is to assess the accuracy with which important map features such as buildings, boundary walls, fences, roads, land parcels, etc. can be mapped from the optimally georeferenced satellite imagery. Accordingly, this test was carried out on the georeferenced satellite imagery resulting from Experiment I-B for all the three Test Areas. Satellite imagery of GSD range from 0.5 m to 2.5 m and representative of the 19 scenes (Table 4-2) employed for Test1-B was used for this test as described below.

Step 1: Manual feature extraction from a single georeferenced GeoEye-1 image resulting from Experiment I-B.

Step 2: Manual extraction of the same features as mapped under Step 1 by stereo compilation from large scale aerial imagery on a Digital Photogrammetric Workstation.

Step 3: Comparison of the outcome of Steps 1 and 2 above through graphic representation. This is supplemented with the extraction of x- and y-coordinates of well-identifiable points for each feature in order to statistically evaluate any 2D positional shift.

For example, a building mapped by following the above steps on a GeoEye-1 image of the Al Muzahimiah Area (ST15) appears in green in Figure 5-4, against the red building compiled stereoscopically from aerial imagery. This building has 14 distinct corners the coordinates of which are measured on the satellite image as well as in the aerial model for analyzing the RMS differences in planimetry.

Figure 5-4: A building feature mapped for Experiment II

Step 4: Repeat Step 1 through Step 3 above for 1.0-m GSD IKONOS imagery.

Step 5: Repeat Step 1 through Step 3 above for 2.5-m GSD SPOT-5 imagery.

5.3 Experiment III: Map Updating

Experiments I and II are designed to investigate the mapping accuracy and, therefore, address the specific questions, Q.1 and Q.2, posed in Section 1.4.4. It is also important to investigate how effectively existing map data can be updated through georeferenced satellite imagery. The data accuracy is only one of the attributes for the quality of map data; the completeness and the validity of the map data are equally important quality measures. Therefore, for Experiment III, sample areas were identified in the existing map database (orthophoto and line maps produced from past aerial imagery) and where, since the acquisition of aerial imagery, significant changes have occurred. The next step was to use the related satellite imagery that resulted from the georeferencing performed under Experiment I-B for updating the map data. The resulting updated map data was checked for spatial accuracy in relation with the existing map data as well as for completeness through field verification. Obviously, the completeness would correspond only to the acquisition date for the satellite imagery.

5.4 Experiment IV: Semi-Automated Georeferencing

The outcome of Test I-B is expected to establish that a large number, perhaps 10 to 15 GCPs are required for removing all the biases associated with the vendor supplied RPCs and to achieve optimum georeferencing accuracy. The manual identification of such a large number of GCPs is the most time consuming task in the processing workflow for georeferencing of satellite imagery. Accordingly, there is a strong incentive to explore means for automating this task. This is particularly relevant for a map production organization like MOMRA.

As emphasized in Chapter 1, it is highly desirable that the need for establishing new ground control for mapping from satellite imagery should be entirely eliminated by using the existing geodatabase information. To serve this purpose, the most useful database currently available in MOMRA is the existing coverage of digital orthophoto data with 50-cm GSD

derived from 1:45,000 scale aerial imagery. It is reasonable to expect that such a georeferenced imagery resource can effectively provide control to supplement the RPCs for more accurate georeferencing of HRSI, especially in the case of the 50-cm GSD GeoEye-1 imagery.

Preliminary thinking had led to the belief that a logical approach for an automated use of the existing orthophoto data may be through the development of a database of Image Control Point (ICP) patches that can be transferred to and identified on the recently acquired satellite imagery through template matching. Practically, however, even though the orthophoto and GeoEye-1 satellite imagery may have the same GSD, there is considerable variation in perspective due to large variation in the sensor altitude and viewing geometry. The fact that recently acquired satellite imagery has to be matched with an orthophoto that has been generated by aerial imagery that may have been acquired a few (3 to 5) years earlier creates additional complications. Consequently, we are faced with the challenge of multi-sensor, multi-season and multi-scale image matching. As pointed out earlier in Chapter 3, the image matching methods that are routinely used in automated matching of overlapping aerial imagery for map production do not present a viable solution. Therefore, it is suggested that the solution to the problem posed may, instead, be investigated by employing either the SIFT algorithm described in Section 3.4.1 or the SURF algorithm described in Section 3.4.2. While SIFT was first and nicely illustrates the concept of scale-invariant and rotation-invariant matching, SURF is faster than SIFT (Bay et al., 2008; Juan and Gwun, 2010). Therefore, SURF is selected to carry out Experiment IV.

5.4.1 Design of Experiment IV

This Experiment is critical to meeting the basic objective of this research study and to demonstrate how efficiently HRSI can be used for routinely updating the existing map database in a map production environment. Therefore, the processing approach and the landscape variation were the major considerations that influenced its design.

The georeferencing of a satellite image is performed in the following steps:

Step 1: Orthorectification of the satellite image using RPC data provided by the vendor, combined with the highest quality DTM data available in the MOMRA database, using commercial software (such as Inpho OrthoMaster). Since no GCP data is used, the resulting orthorectified image will generally have X- and Y-coordinate biases of a few meters. It is to be noted that such orthorectified images have already become available on the earlier completion of Experiment 1-A.

Step 2: Location and matching of key points on the satellite image resulting from step 1 and the overlapping aerial orthophoto image using SURF. An implementation of the SURF algorithm in MATLAB has been developed and tested for completing this step. The MATLAB Toolbox permits the import of a georeferenced satellite image or an orthophoto as a geotiff file that preserves the georeferencing information embedded in the file header. When exported as a geotiff file, the raster file (in pixel coordinates) recovers the georeferencing information. Both the georeferenced satellite image resulting from step 1 and the corresponding orthophoto were based on the UTM coordinate system. Since the primary objective is to demonstrate the capability for effectively matching the satellite and the aerial imagery (and proving the concept), it was decided to use a subset of the corresponding pairs of satellite and aerial images only, instead of the full images for the purpose of testing. Accordingly, this testing was carried out on 800 x 800 pixel image patches, which is analogous to the use of control image chips for image matching. In the area of this size, the maximum number of key points was restricted to 200. UTM coordinates, on the satellite and the aerial orthophoto can be compared at this point and the outliers showing bad matches with large coordinate differences can be rejected. The RMS values for the X-coordinate and the Y-coordinate differences were calculated and any variation larger than 3 times the RMS value was rejected.

Step 3: Transformation of the satellite orthoimage to the orthophoto through a 2-D Affine Coordinate Transformation

using the coordinates of the key points on the orthophoto as control data. Even though the differences in the two coordinate data sets are likely to be dominated by X and Y coordinate shifts (Fraser and Yamakawa, 2003; Dowman et al., 2012), six transformation parameters were used to accommodate any scale differences along the two coordinate axes, any rotation as well as non-orthogonality in the system. The large number of matched key points, well distributed over the image should provide a strong least squares based adjustment solution for the resulting georeferenced satellite image. In addition, the adjustment residuals provide further information regarding the quality of image matching. An implementation of the affine coordinate transformation was also developed in MATLAB and used for this Experiment.

Step 4: Checking the accuracy in georeferencing through Check Points extracted from the aerial orthophoto as described for Experiments I and II.

5.4.2 Landscape Variation

It is essential that the proposed automated georeferencing process described above is tested over widely different landscape features seen in the satellite imagery covering Saudi Arabia, as well as, be representative of all three different types of satellite imagery tested under Experiments I, II and III. With this objective, image patches of 800 x 800 pixels each were extracted from selected GeoEye-1, IKONOS and SPOT-5 images, representing the three different types of landscape features. The landscape type was selected as Urban, to represent mostly built-up area in cities, Agriculture, to include extended vegetation cover and Rural Open, which primarily represents large open areas with sparse human activity. A sampling of such landscape areas is shown in Figure 5-5.

Figure 5-5: A sample of the three different landscape types used for Experiment IV

5.5 Concluding Comments

The above Experiment-I through Experiment-IV are designed to answer the five questions posed in Chapter 1. The predominant interest in this study is reflected in Q1 and Q2 that relate to the geopositional accuracy achievable from HRSI under map production conditions. Accordingly, the results obtained from Experiment-I, Experiment-II and Experiment-III should lead to appropriate answers to Q1 and Q2. The remaining three questions are aimed at accelerating the map production process through automation in the GCP selection. In the light of the detailed discussion presented in Section 5.4 regarding the choice of a method that is best suited for matching the satellite and aerial orthophotos, and consequently, the decision arrived at to use SURF based matching approach, the Experiment-IV is designed to provide insight in seeking answers to the questions Q3, Q4 and Q5 which are of critical importance for satellite mapping in a production environment. The Experiment results are presented and discussed in the following Chapter 6.

Chapter 6. Experimental Results

All the experiments mentioned in the last Chapter were completed successfully by following the processing steps described for each experiment. Even though new satellite imagery was especially acquired for this study as described in Chapter 4, the scope of testing was significantly extended by including all 19 available satellite images (ST01 through ST19) listed in Table 4-2. Experimenting with such a large number of satellite images to reflect the impact of satellite image resolution as well as the variation in landscape has generated a large volume of test result data. All the result data has been organized systematically in Appendix-I. Consequently, only summaries of the results from various experiments are presented and discussed in this Chapter.

The experiments were designed to address two main issues: the georeferencing accuracy and speed of HRSI and the ability to map or update an existing map using HRSI. Accordingly, the results of the experiments are presented in the same order. Both Experiment I and Experiment IV are designed to investigate the achievable HRSI georeferencing accuracy, while Experiments II and III are aimed at demonstrating the ability to map or update an existing map using HRSI.

6.1 Georeferencing Accuracy

6.1.1 Results of Experiment I

As described in Section 5.1, the Experiment I-A was designed to test the georeferencing accuracy achieved when high resolution satellite imagery is processed for orthoprojection using vendor supplied RPCs combined with DTM data but without using any ground control.

The improvement in the achievable georeferencing accuracy with the additional input of an increasing number of ground control points distributed over the image scene is investigated in Experiment I-B. The mean and the RMS values for the residuals obtained at the Check Points resulting from Experiment I-A and I-B for the GeoEye-1 imagery of all the three Test Areas are summarized in Table 6-1. The corresponding results of Experiment I-A and I-B for IKONOS-2 imagery are shown in Table 6-2, and for SPOT-5 imagery are given in Table 6-3.

Table 6-1: Summary of Experiment I-A and 1-B Results for GeoEye-1 imagery

Summary of Exp 1A & 1B: GeoEye-1 (50-cm)								
CASE	**RIYADH**					**Al-MUZAHIMIAH**		
	ST0 TT	**ST06**	**ST07**	**ST08**	**ST09**	**ST13**	**ST14**	**ST15**
Total Check Points	15	15	10	15	10	5	5	5
RPC with No GCP								
Mean_x (m)	0.9	0.53	0.18	-0.69	1.73	-3.37	1.94	-1.03
Mean_y (m)	-3.79	-3.18	-2.04	-1.48	1.25	-3.61	1.83	-0.81
RMS_x (m)	1.17	2.24	0.95	1.3	1.79	3.43	2.04	1.1
RMS_y (m)	3.87	3.68	3.89	1.58	1.34	3.63	1.85	1.21

Summary of Exp 1A & 1B: GeoEye-1 (50-cm)								
CASE	**RIYADH**					**Al-MUZAHIMIAH**		
	ST05	**ST06**	**ST07**	**ST08**	**ST09**	**ST13**	**ST14**	**ST15**
Total Check Points	15	15	10	15	10	5	5	5
RPC + 5 GCP								
Mean_x (m)	-0.65	-0.82	-0.61	-0.29	-0.76	-0.31	-0.16	0.06
Mean_y (m)	0.15	-0.02	0.52	0.56	0.33	-0.1	0.26	0.09
RMS_x (m)	1.06	1.62	2.04	1.16	0.87	0.88	0.54	0.29
RMS_y (m)	1.56	1.56	2.6	0.67	0.52	0.28	0.41	0.54
RPC + 10 GCP						**RPC + 7 GCP**		
Mean_x (m)	-0.72	-0.39	-0.38	-0.34	-0.34	-0.19	-0.11	0.28
Mean_y (m)	0.86	0.29	0.22	0.34	0.46	-0.13	0.2	0.18
RMS_x (m)	1.2	1.03	1.7	1.05	0.51	0.73	0.55	0.37
RMS_y (m)	0.9	0.57	2.31	0.66	0.52	0.27	0.41	0.53
RPC + 15 GCP						**RPC + 10 GCP**		
Mean_x (m)	-0.52	-0.45	-0.15	-0.47	-0.03	-0.38	-0.15	0.16
Mean_y (m)	0.76	0.24	0.47	0.54	0.46	-0.04	0.36	0.11
RMS_x (m)	0.88	0.96	0.71	1.03	0.37	0.71	0.44	0.21
RMS_y (m)	1.1	0.69	0.75	0.63	0.51	0.26	0.39	0.58

Table 6-2: Summary of Experiment I-A and 1-B Results for IKONOS-2 imagery

Summary of Exp 1A & 1B: IKONOS (1-m)							
CASE	**RIYADH**			**Al-MUZAHIMIAH**		**HURAYMILA**	
	ST02	**ST03**	**ST04**	**ST11**	**ST12**	**ST18**	**ST19**
Total Check Points	15	15	10	8	10	10	10
RPC with No GCP							
Mean_x (m)	-4.09	-1.69	-3.47	-0.7	0.11	-1.39	3.18
Mean_y (m)	4.79	6.38	8.98	1.75	4.91	4.62	13.18
RMS_x (m)	4.17	1.96	3.53	0.85	1.01	1.58	3.27
RMS_y (m)	4.86	6.42	9.02	1.95	5.02	4.68	13.19

Summary of Exp 1A & 1B: IKONOS (1-m)							
CASE	**RIYADH**			**Al-MUZAHIMIAH**		**HURAYMILA**	
	ST02	**ST03**	**ST04**	**ST11**	**ST12**	**ST18**	**ST19**
Total Check Points	15	15	10	8	10	10	10
RPC + 5 GCP							
Mean_x (m)	-0.63	-0.57	0.47	-0.72	-0.69	-0.22	0.58
Mean_y (m)	1.31	2.07	0.99	0.61	1.01	0.85	0.5
RMS_x (m)	1.13	1.31	0.3	0.94	1.24	1.25	1.37
RMS_y (m)	1.56	2.17	0.35	1.19	1.39	1.36	1.01
RPC + 10 GCP				**RPC + 7 GCP**			
Mean_x (m)	-0.51	-0.76	-0.26	-0.7	-0.31	-0.44	0.43
Mean_y (m)	1.24	1.61	0.83	0.83	0.86	0.6	0.9
RMS_x (m)	0.95	1.3	0.75	0.87	0.84	0.91	0.69
RMS_y (m)	1.47	1.72	1.22	0.97	1.13	1.27	0.99
RPC + 15 GCP				**RPC + 10 GCP**			
Mean_x (m)	-0.43	-0.96	-0.19	-0.36	-0.17	-0.01	0.06
Mean_y (m)	1.17	0.59	0.89	0.85	0.58	0.97	0.76
RMS_x (m)	0.75	1.33	0.65	0.73	0.77	0.8	0.68
RMS_y (m)	1.43	0.95	1.09	0.89	1.04	1.15	0.94

Table 6-3: Summary of Experiment I-A and 1-B Results for SPOT-5 imagery

Summary of Exp 1A & 1B: SPOT-5 (2.5-m)				
CASE	**RIYADH**	**Al-MUZAHIMIAH**	**HURAYMILA**	
	ST01	**ST10**	**ST16**	**ST17**
Total Check Points	13	10	10	10
RPC with No GCP				
Mean_x (m)	-0.37	0.58	-1.91	0.54
Mean_y (m)	2.47	0.26	1.48	-0.15
RMS_x (m)	1.55	3.9	2.54	4.26
RMS_y (m)	2.88	1.75	2.63	2.32

Summary of Exp 1A & 1B: SPOT-5 (2.5-m)				
CASE	**RIYADH**	**Al-MUZAHIMIAH**	**HURAYMILA**	
	ST01	**ST10**	**ST16**	**ST17**
Total Check Points	13	10	10	10
RPC + 5 GCP				
Mean_x (m)	-0.2	0.76	-0.34	-0.09
Mean_y (m)	1.99	0.6	2.33	-0.53
RMS_x (m)	1.48	3.33	1.78	2.68
RMS_y (m)	2.35	1.62	0.64	2.4
RPC + 10 GCP				
Mean_x (m)	-0.55	-0.16	0.59	-0.18
Mean_y (m)	1.24	0.84	1.22	-0.5
RMS_x (m)	1.54	2.74	1.83	2.17
RMS_y (m)	1.62	1.69	1.42	1.83
RPC + 15 GCP				
Mean_x (m)	-0.13	0.06	0.32	-0.39
Mean_y (m)	0.61	0.83	0.58	-0.23
RMS_x (m)	0.89	2.54	1.73	2.09
RMS_y (m)	1.00	1.78	1.19	1.68

The results of Experiment I-A and I-B performed on GeoEye-1 imagery and tabulated in Table 6-1 have been summarized by averaging the RMS values in the X- and the Y-coordinate differences at the Check Points, according to the number of GCPs used for georeferencing. The results are tabulated in Table 6-4 and displayed graphically in Figure 6-1 and Figure 6-2.

Riyadh			Al Muzahimiah		
GCP	**RMSE_x** (m)	**RMSE_y** (m)	**GCP**	**RMSE_x** (m)	**RMSE_y** (m)
0	1.49	2.19	0	2.87	2.23
5	1.35	1.38	5	0.57	0.41
10	1.10	0.99	10	0.55	0.40
15	0.79	0.74	15	0.45	0.41

Table 6-4: RMS at Check Points for GeoEye-1 Imagery

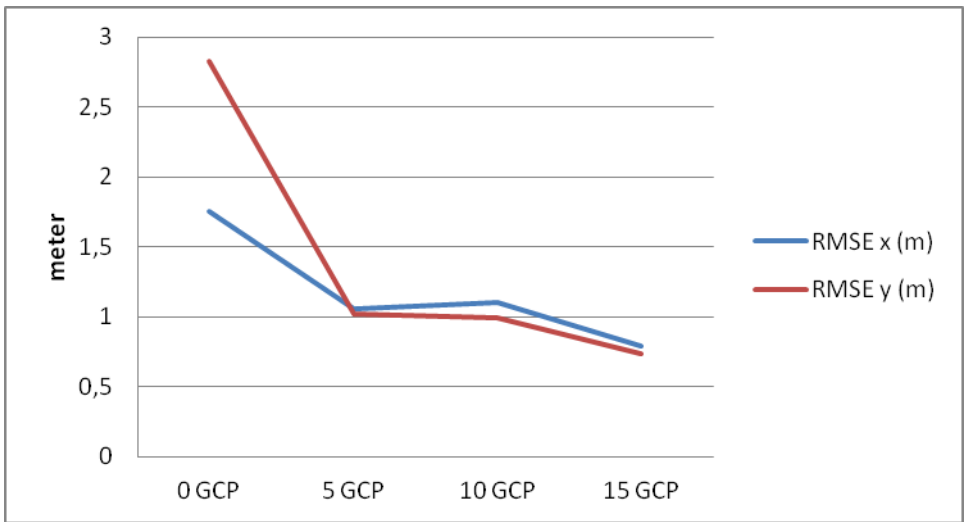

Figure 6-1: Impact of number of GCPs on georeferencing accuracy for GeoEye-1 imagery of Riyadh Area

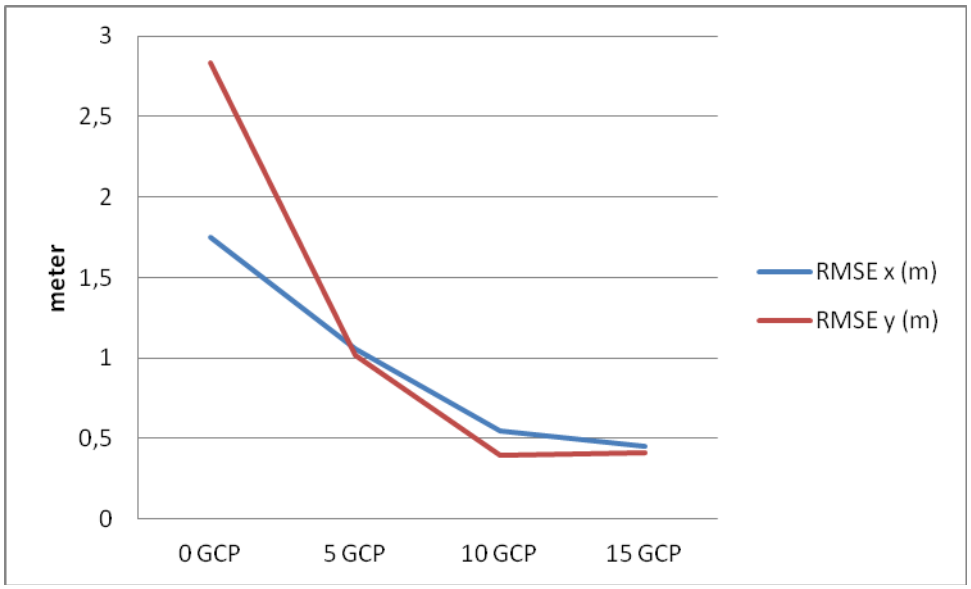

Figure 6-2: Impact of number of GCPs on georeferencing accuracy for GeoEye-1 imagery of Al-Muzahimiah Area

Similar results of Experiment I-A and I-B for the 1-m IKONOS-2 imagery are tabulated in Table 6-5 and displayed graphically in Figure 6-3 for Riyadh Area and for the Al-Muzahimiah and Huraymila Areas in Figure 6-4.

Riyadh			Al Muzahimiah & Huraymila		
GCP	RMSE_x (m)	RMSE_y (m)	GCP	RMSE_x (m)	RMSE_y (m)
0	2.34	6.45	0	2.34	6.45
5	1.22	1.43	5	1.22	1.43
10	1.00	1.41	10	0.83	1.09
15	0.91	1.16	15	0.75	1.01

Table 6-5: RMS at Check Points for IKONOS-2 Imagery

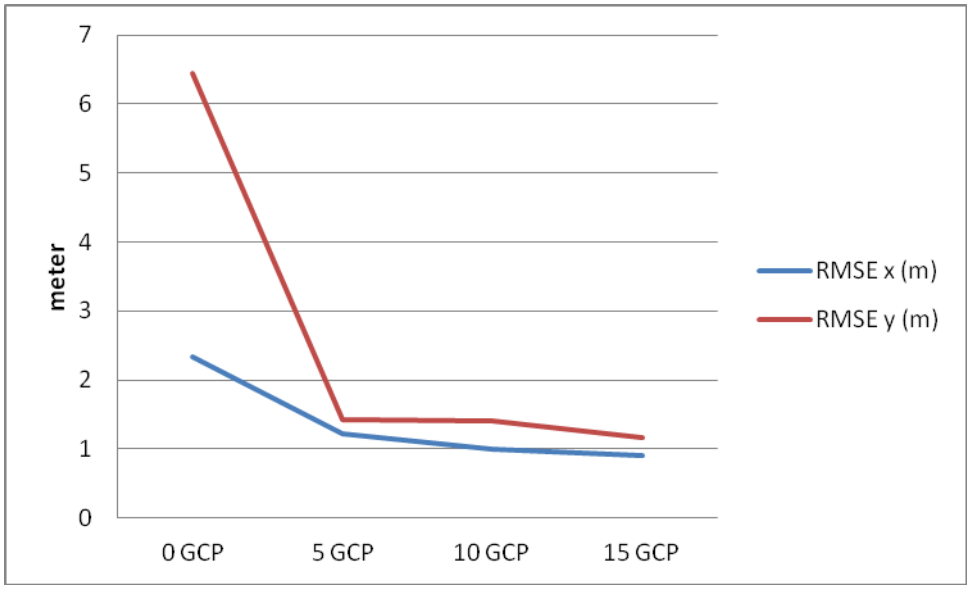

Figure 6-3: Impact of number of GCPs on georeferencing accuracy forIKONOS-2 imagery of Riyadh Area

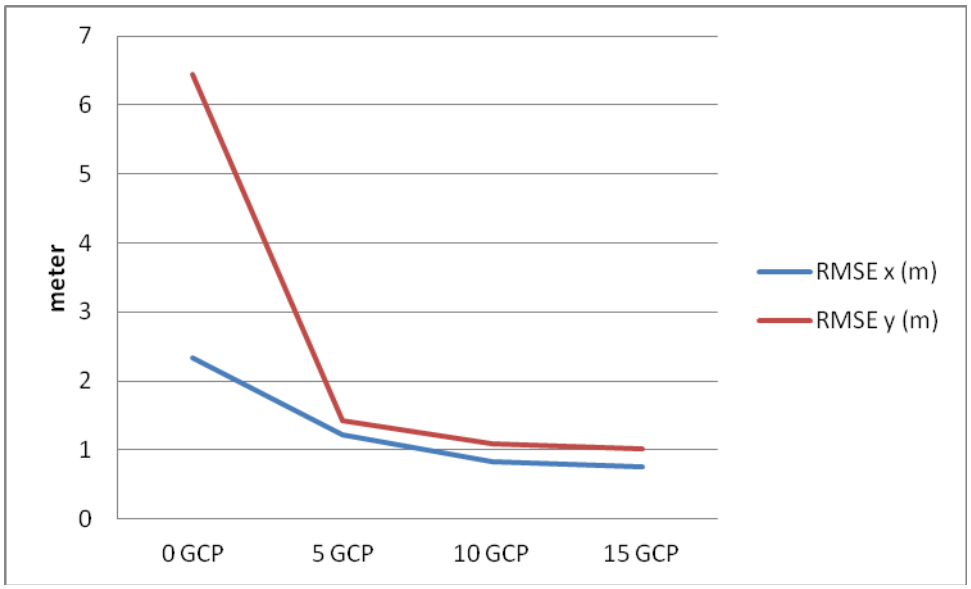

Figure 6-4: Impact of number of GCPs on georeferencing accuracy forIKONOS-2 imagery of Al-Muzahimiah and Huraymila Areas

Similar data for the impact of the number of GCPs used during georeferencing processing of SPOT-5 imagery for all the three Test Areas is tabulated in Table 6-6 and displayed graphically in Figure 6-5.

All Test Areas		
GCP	**RMSE_x** (m)	**RMSE_y** (m)
0	3.06	2.40
5	2.32	1.75
10	2.07	1.64
15	1.81	1.41

Table 6-6: RMS at Check Points for SPOT-5 Imagery

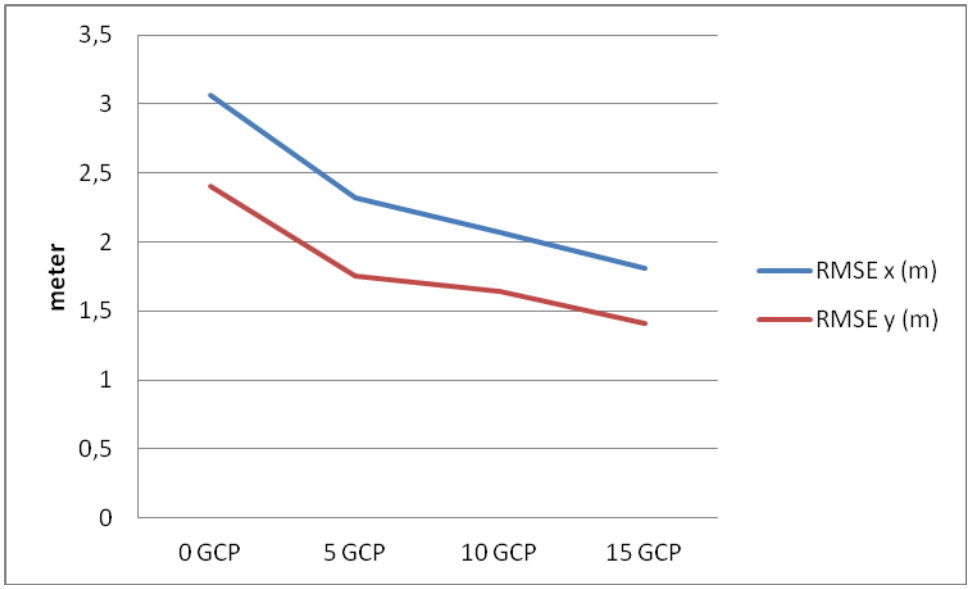

Figure 6-5: Overall impact of number of GCPs on georeferencing accuracy for SPOT-5 imagery for all Areas

As an alternative to the manual selection and measurement of control point data, the Experiment IV was designed to use existing georeferenced aerial imagery, such as an orthophoto to serve as the control for the semi-automated georeferencing of recently acquired satellite imagery. Therefore, the results of the Experiment IV are presented next.

6.1.2 Results of Experiment IV

As discussed in detail in Section 5.4, it was decided to perform the automated matching of the satellite and the aerial orthophoto images using the SURF algorithm for compiling test data for Experiment IV. Since the effectiveness of the matching approach is independent of the size of the two images being matched, but rather on the image texture, it was decided not to use the entire satellite image scenes for this experiment. Instead, 800 x 800 pixel patches were extracted from the satellite images to reflect differences in texture resulting from differences in landscape. As pointed out earlier in Chapter 5, test samples were selected that are representative of typical agricultural, urban and rural landscapes in Saudi Arabia. However, all three types of satellite imagery, viz. GeoEye-1, IKONOS-2 and SPOT-5 imagery have been tested.

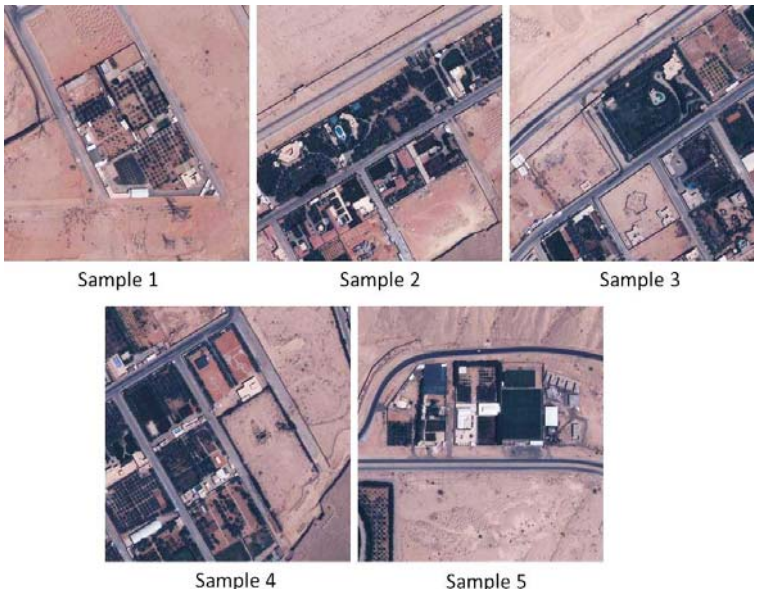

Figure 6-6: Riyadh GeoEye imagery Agricultural site samples used for test

6.1.2.1 GeoEye-1 Imagery

The 50-cm GSD GeoEye-1 image No. 2418066_0010000 (ST09) of Riyadh acquired in 2010 (see Figure 5-1) was selected for the test as it includes urban, agricultural and rural sites. Five 800 x 800 pixel size image patches were sampled from this image to represent each type of landscape. The selected agricultural samples (numbered 1 through 5) are shown in Figure 6-6. Similar samples for the urban landscape (numbered 6 through 10) and for the rural areas (numbered 11 through 15) are shown in Figure 6-7 and Figure 6-8, respectively.

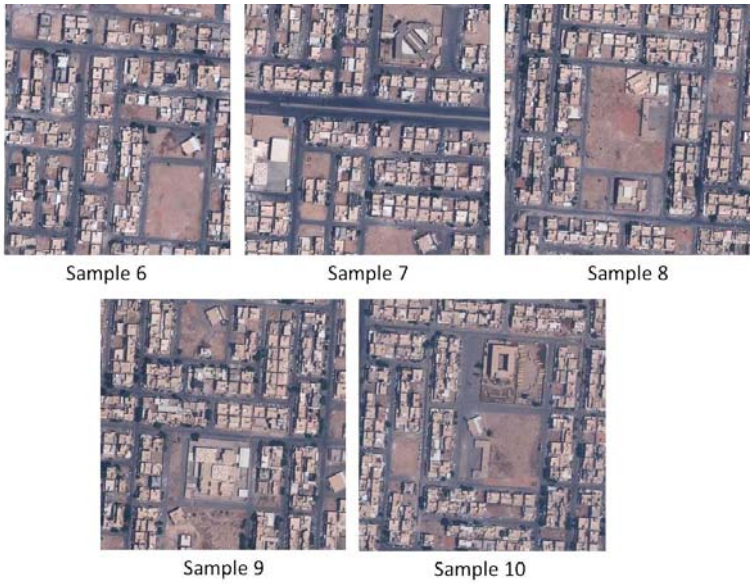

Figure 6-7: Riyadh GeoEye imagery urban site samples used for test

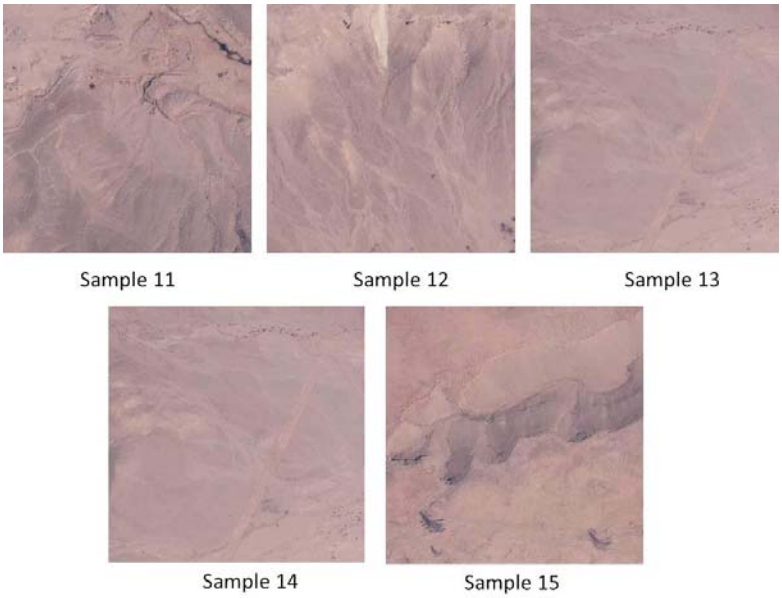

Figure 6-8: Riyadh GeoEye imagery rural site samples used for test

Corresponding image areas of 800 x 800 pixels were also extracted from an existing orthophoto with 50-cm GSD that had been produced from 1:45,000 scale aerial imagery. As described in Chapter 5, the GeoEye-1 and the corresponding orthophoto image of a sample were matched using the SURF tool. An example of the distribution of the extracted key points and the matched tie points for an agricultural area sample is shown in Figure 6-9 and Figure 6-10. Similar key point and tie point distribution for an urban area and a rural area are shown in Figure 6-11 through Figure 6-14, respectively. Table 6-7 contains the number of extracted key points and tie points (note that the maximum number of tie points was set to 200).

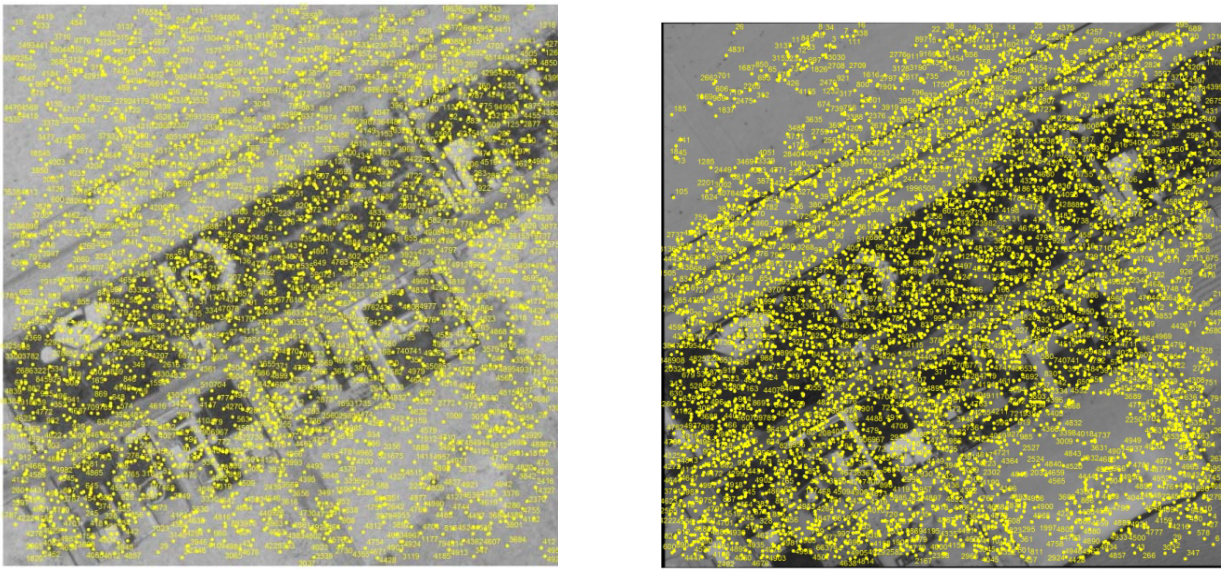

Figure 6-9: Key point distribution in Agricultural Sample 2; Riyadh, GeoEye Imagery (left); orthophoto (right)

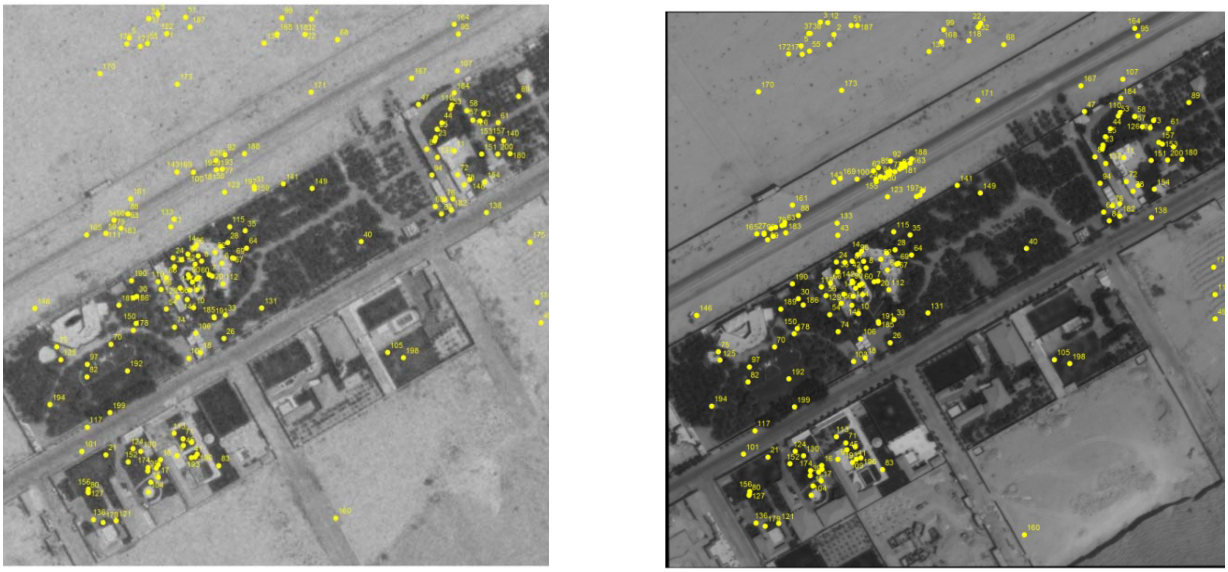

Figure 6-10: Tie point distribution in Agricultural Sample 2; Riyadh, GeoEyeImagery (left); orthophoto (right)

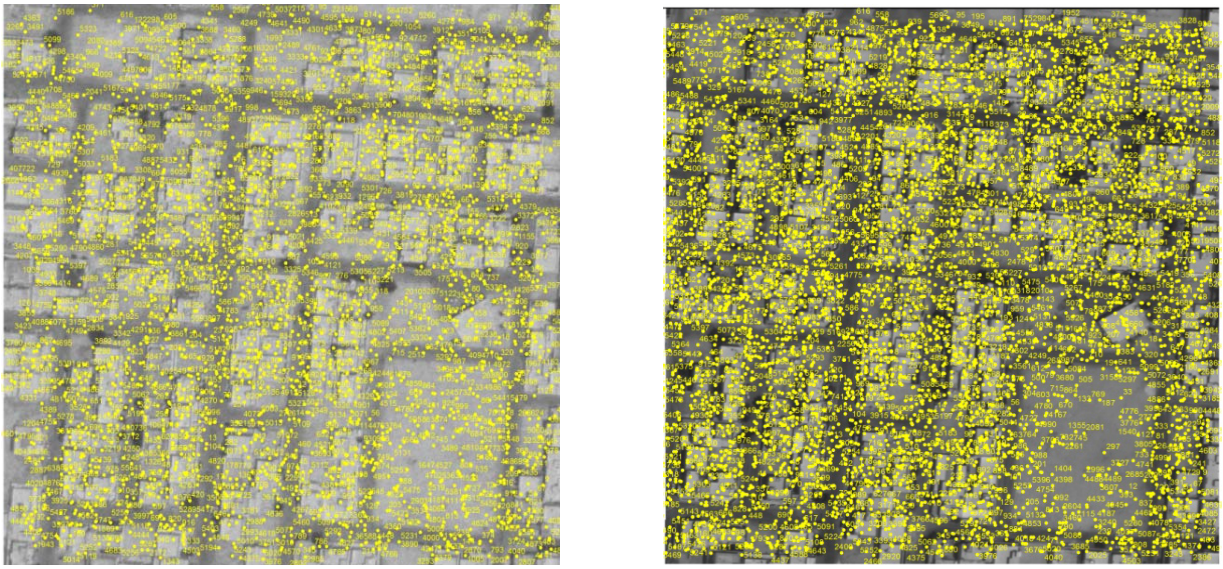

Figure 6-11: Key point distribution in Urban Sample 6; Riyadh, GeoEye Imagery (left); orthophoto (right)

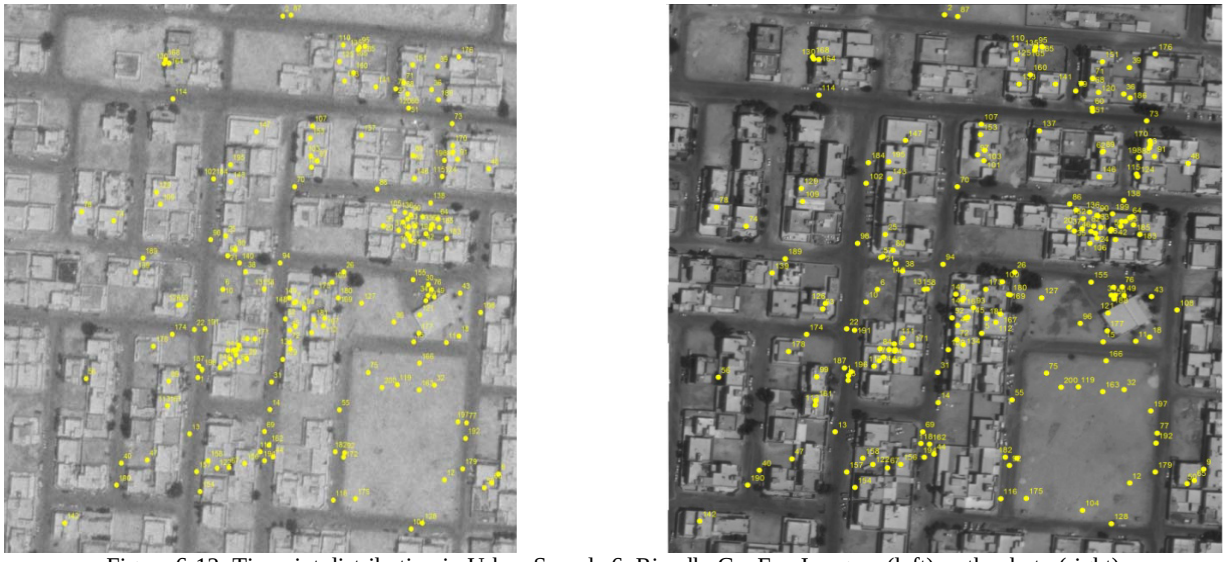

Figure 6-12: Tie point distribution in Urban Sample 6; Riyadh, GeoEye Imagery (left); orthophoto (right)

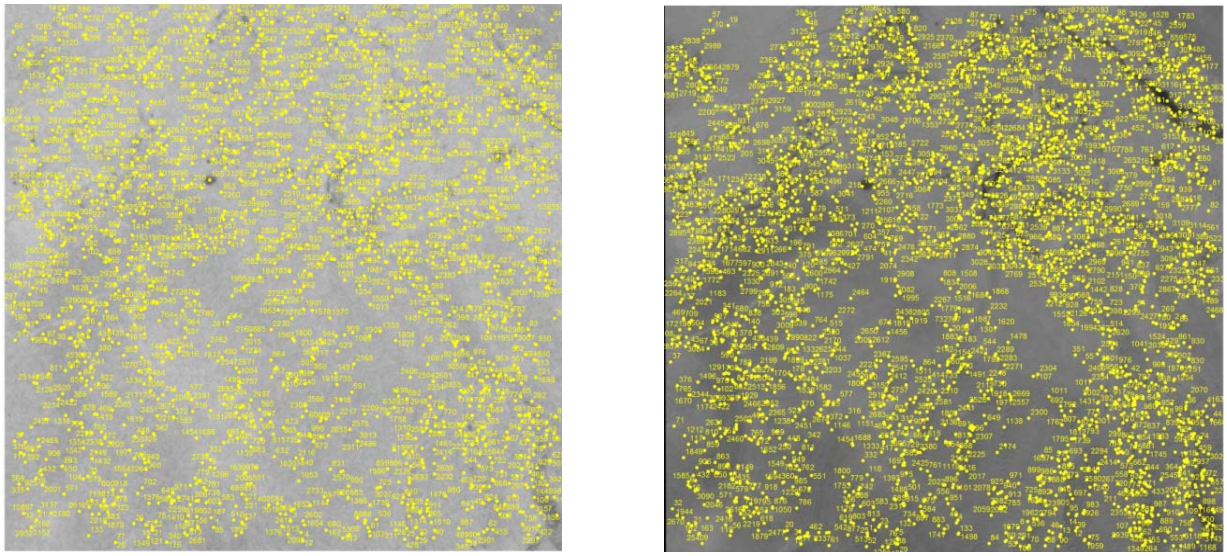

Figure 6-13: Key point distribution in Rural Sample 11; Riyadh, GeoEye Imagery (left); orthophoto (right)

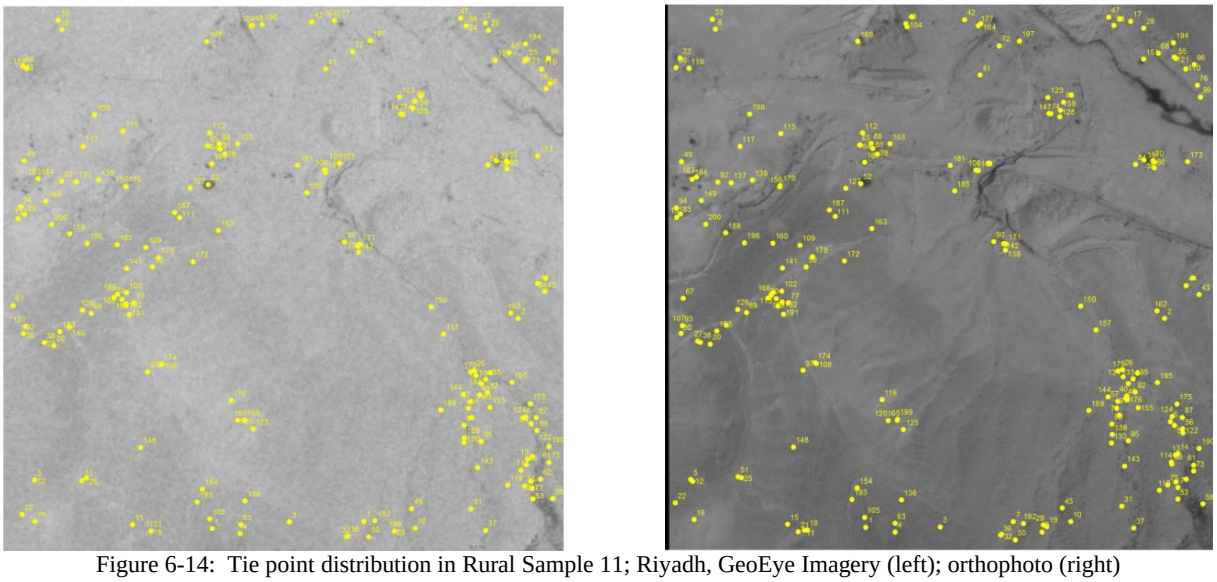

Figure 6-14: Tie point distribution in Rural Sample 11; Riyadh, GeoEye Imagery (left); orthophoto (right)

#	Sample No.	Sensor	Area	Key Points Orthophoto	Key Points Satellite	Tie Points
1	ExpIV-06-1	GeoEye	Agricultural	4,868	3,729	200
2	ExpIV-06-2	GeoEye	Agricultural	5,210	4,995	200
3	ExpIV-06-3	GeoEye	Agricultural	5,523	4,868	200
4	ExpIV-06-4	GeoEye	Agricultural	5,555	5,405	200
5	ExpIV-06-5	GeoEye	Agricultural	5,177	5,022	200
6	ExpIV-06-6	GeoEye	Urban	5,429	5,490	200
7	ExpIV-06-7	GeoEye	Urban	5,771	5,962	200
8	ExpIV-06-8	GeoEye	Urban	5,508	6,141	200
9	ExpIV-06-9	GeoEye	Urban	5,495	6,201	200
10	ExpIV-06-10	GeoEye	Urban	5,594	5,928	200
11	ExpIV-06-11	GeoEye	Rural	3,822	3,161	200
12	ExpIV-06-12	GeoEye	Rural	5,210	4,995	200
13	ExpIV-06-13	GeoEye	Rural	3,249	1,353	200
14	ExpIV-06-14	GeoEye	Rural	3,832	2,260	200
15	ExpIV-06-15	GeoEye	Rural	3,968	2,552	200

Table 6-7: Number of Key points and Tie points based on SURF-processing of GeoEye-1 imagery

GeoEye-1(50-cm) Image No. 2418066_0010000 (Riyadh/2010)											
Agricultural				Urban				Rural			
Patch	RMSx (m)	RMSy (m)	Check Points	Patch	RMSx (m)	RMSy (m)	Check Points	Patch	RMSx (m)	RMSy (m)	Check Points
1	0.77	1.00	5	6	0.87	0.92	5	11	0.32	0.27	5
2	0.63	0.91	5	7	0.94	1.03	5	12	0.23	0.39	5
3	0.48	0.86	5	8	0.62	0.83	5	13	0.27	0.44	5
4	0.54	0.86	5	9	0.38	1	5	14	0.57	0.69	5
5	0.31	0.84	5	10	0.99	0.99	5	15	79	0.95	5
Mean	**0.55**	**0.89**		**Mean**	**0.76**	**0.76**		**Mean**	**0.44**	**0.55**	
Average of all coordinate RMS values = 0.70 m											

Table 6-8: Check Point discrepancies based on SURF-processing of GeoEye-1 imagery

The processing for matching was followed by the transformation of the GeoEye-1 image to the orthophoto image using the orthophoto image coordinates of the tie points as control for a 2D Affine coordinate transformation. Several Check Points distributed evenly over the transformed GeoEye-1 image were measured. The RMS values in the differences in X- and Y-coordinate at the Check Points are tabulated in Table 6-8 for all the 15 sample sites used.

Even though the above test was carried out over a reasonably large set of data samples, a similar test was repeated on GeoEye-1 image No. 2415597_0000003 (ST05) of Riyadh acquired in 2009. Six samples were used and the results are tabulated in Table 6-9. The Check Points used for any sample were also measured on the corresponding satellite image that had been georeferenced for completing Experiments I-A and I-B, and these results are also included in Table 6-9.

GeoEye-1 (50-cm) Image No. 2415597_0010000 (Riyadh/2009)							
Area Type	Sample	RPC + DTM No GCP		RPC + DTM 15 GCP		RPC + DTM SURF + 2D Affine	
		RMS x (m)	RMS y (m)	RMS x (m)	RMS y (m)	RMS x (m)	RMS y (m)
Urban	1	0.60	4.89	1.60	1.04	1.18	1.6
	2	2.17	4.13	1.09	1.26	1.36	1.19
	3	0.76	4.97	0.89	0.66	0.32	0.5
	Mean	**1.18**	**4.66**	**1.19**	**0.99**	**0.95**	**1.1**
Agricultural	4	1.45	3.32	2.54	1.79	1.79	1.31
	5	1.18	4	1.09	1.37	1.01	1.58
	Mean	**1.31**	**3.66**	**1.82**	**1.58**	**1.4**	**1.45**
Rural	6	1.32	4.34	0.95	0.59	1.09	0.31
	Mean	**1.32**	**4.34**	**0.95**	**0.59**	**1.09**	**0.31**

Table 6-9: Examples of comparative Check Point discrepancies based on SURF-processing against georeferencing performed without GCP and with manually measured GCP data

6.1.2.2 IKONOS-2 Imagery

The IKONOS-2 image No. 2418067_0010000 (ST04) covering the Riyadh area and acquired in 2010 was used for this experiment. The IKONOS-2 image has a 1-m GSD while the corresponding orthophoto has a 50-cm GSD; therefore, both the images were first brought to the same resolution level before matching them. The reason is because even though both SIFT and SURF are scale-invariant, Oh et al. (2010), while using SIFT, reported a significant drop in the number of matched points when increasing the difference in image resolution. The approach adopted was to down-sample the orthophoto image from a resolution of 50-cm to 1 m in order to avoid any aliasing effects by sub-sampling of the IKONOS-2 image. After some experimenting with different interpolation algorithms for resampling, it was found that resampling based on bilinear interpolation resulted in the best radiometric quality. Accordingly, the down-sampled orthophoto image was obtained at 1 m resolution using bilinear interpolation.

For automated georeferencing through SURF-based processing, different samples of 800 x 800 pixels were extracted from the IKONOS-2 image covering agricultural sites, urban sites and rural sites. An example of the distribution of the extracted key points and the matched tie points for an agricultural area sample is shown in Figure 6-15 and Figure 6-16. Similar key point and tie point distribution for an urban area and a rural area are shown in Figure 6-17 through Figure 6-20, respectively. Table 6-10 contains the number of extracted key points and tie points (note again that the maximum number of tie points was set to 200). The results at the Check Points are tabulated in Table 6-11.

#	Image No	Sensor	Area	Key Points Orthophoto	Key Points Satellite	Tie Points
1	ExpIV-02-1	IKONOS	Agricultural	4,868	2,403	200
2	ExpIV-02-2	IKONOS	Agricultural	5,210	3,006	200
3	ExpIV-02-3	IKONOS	Agricultural	5,523	3,721	200
4	ExpIV-02-4	IKONOS	Agricultural	5,555	3,901	200
5	ExpIV-02-5	IKONOS	Agricultural	5,177	2,876	200
6	ExpIV-02-6	IKONOS	Urban	5,771	4,201	200
7	ExpIV-02-7	IKONOS	Urban	5,508	4,443	200
8	ExpIV-02-8	IKONOS	Urban	5,495	4,468	200
9	ExpIV-02-9	IKONOS	Urban	5,594	4,363	200
10	ExpIV-02-10	IKONOS	Rural	3,822	885	200

Table 6-10: Examples of number of Key points and Tie points based on SURF-processing of IKONOS-2 imagery

IKONOS-2 (1-m) Image No. 2418067_0010000 (Riyadh/2010)											
Agricultural				Urban				Rural			
Patch	RMS x (m)	RMS y (m)	Check Points	Patch	RMS x (m)	RMS y (m)	Check Points	Patch	RMS x (m)	RMS y (m)	Check Points
1	1.26	0.95	6	6	1.42	1.28	10	10	1.14	1.96	6
2	0.62	1.29	12	7	0.41	0.81	12	-	-	-	-
3	2.01	2.12	5	8	1.64	2.36	12	-	-	-	-
4	0.96	1.84	6	9	0.94	0.79	12	-	-	-	-
5	0.95	1.57	12	-	-	-	-	-	-	-	-
Mean	**1.16**	**1.55**	-	**Mean**	**1.10**	**1.31**	-	**Mean**	**1.14**	**1.96**	-
Average of all coordinate RMS values = 1.37 m											

Table 6-11: Examples of check point discrepancies based on SURF-processing of IKONOS-2 imagery

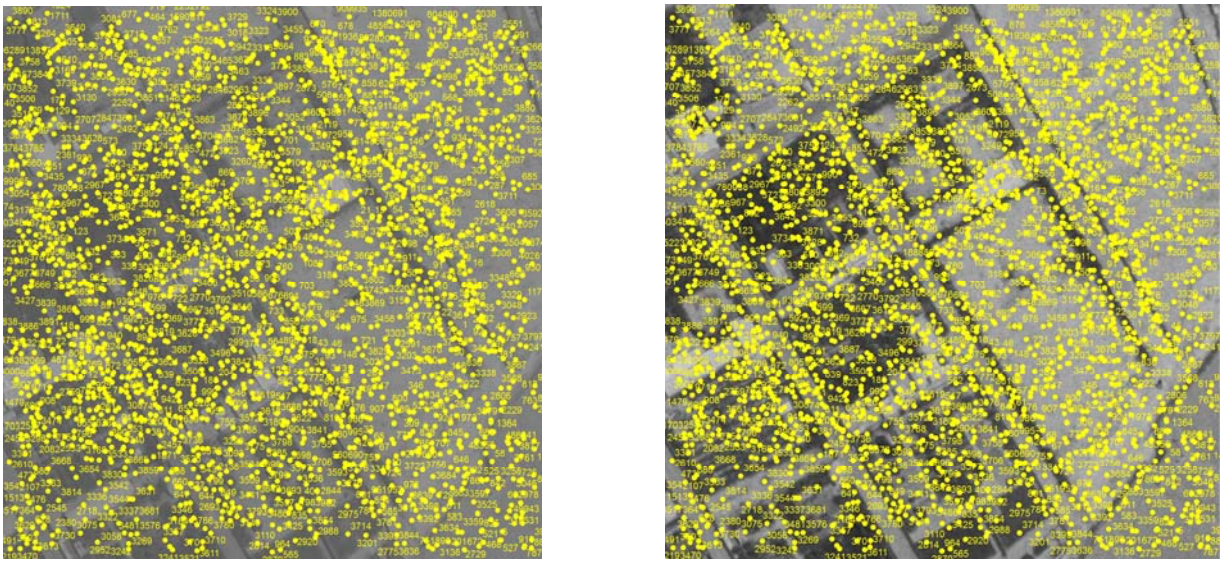

Figure 6-15: Key point distribution in Agricultural Sample 4; IKONOS-2 Imagery (left) down sampled orthophoto (right)

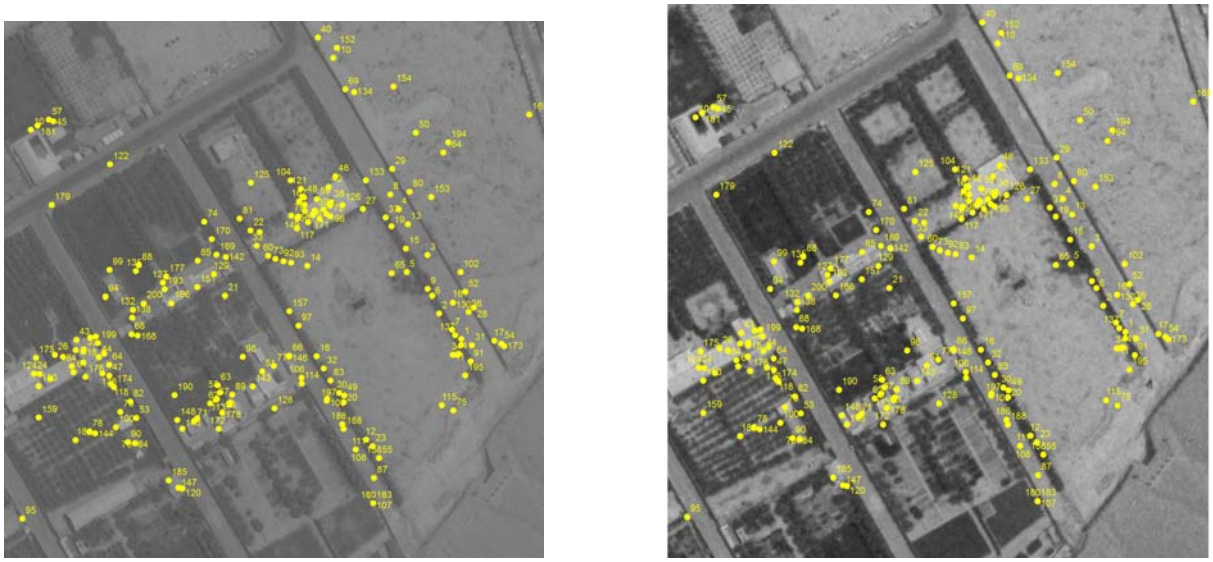

Figure 6-16: Tie point distribution in Agricultural Sample 4; IKONOS-2 Imagery (left) down sampled orthophoto (right)

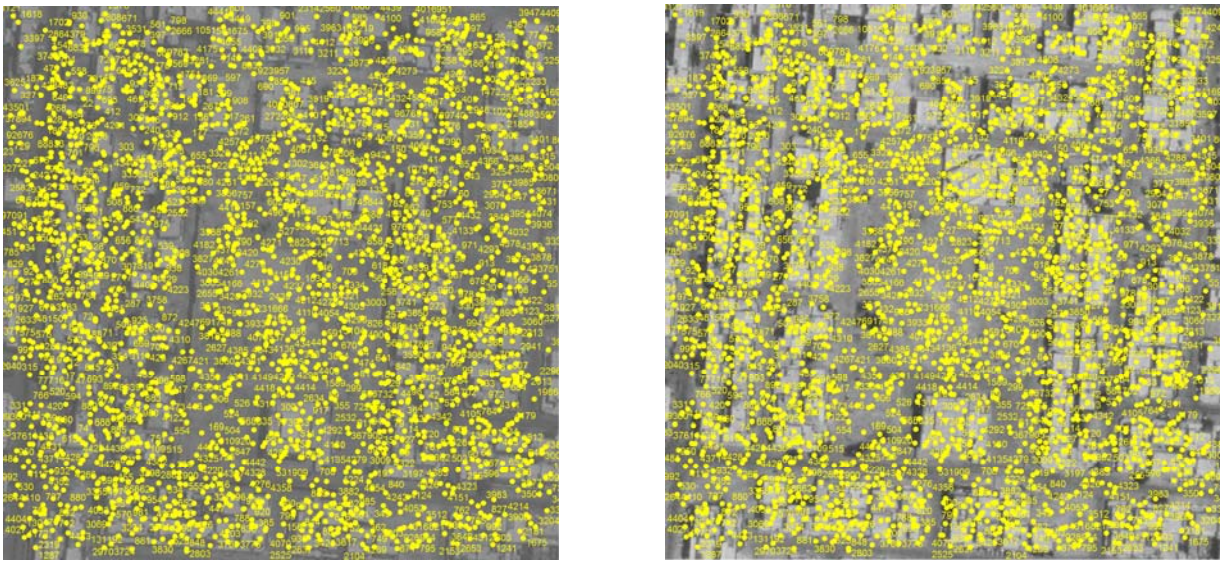

Figure 6-17: Key point distribution in Urban Sample 7; IKONOS-2 Imagery (left) down sampled orthophoto (right)

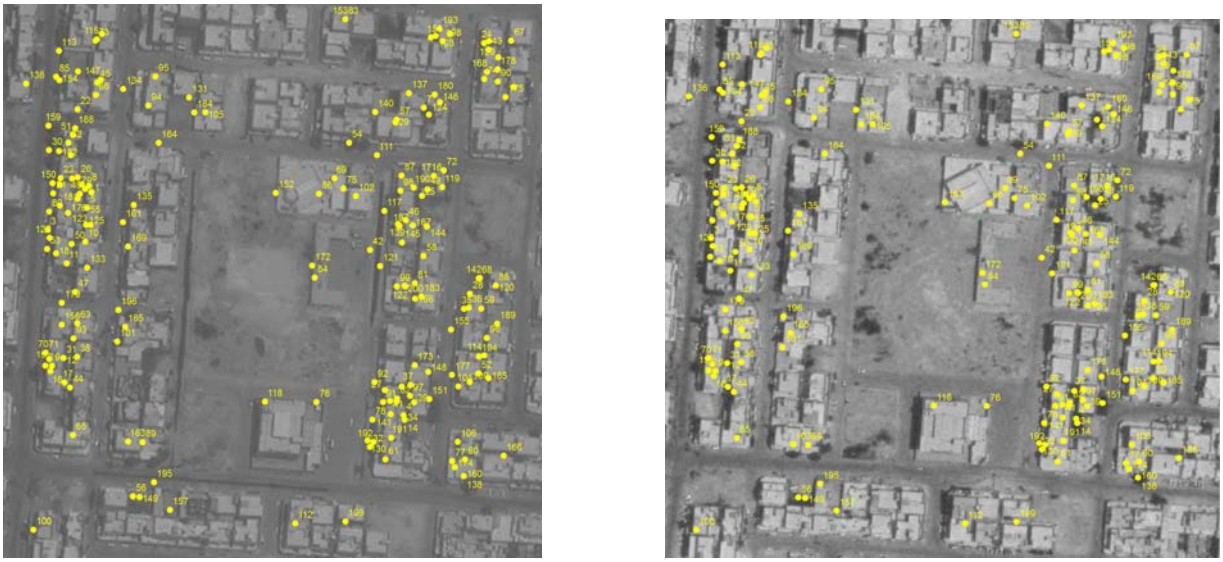

Figure 6-18: Tie point distribution in Urban Sample 7; IKONOS-2 Imagery (left) down sampled orthophoto (right)

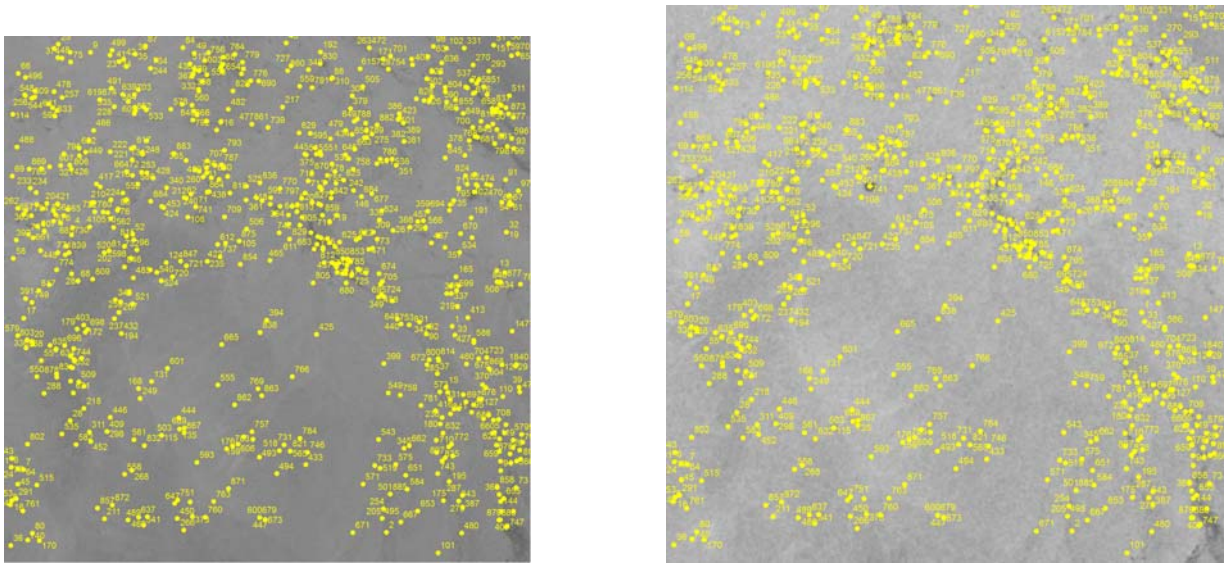

Figure 6-19: Key point distribution in Rural Sample 10; IKONOS-2 Imagery (left) down sampled orthophoto (right)

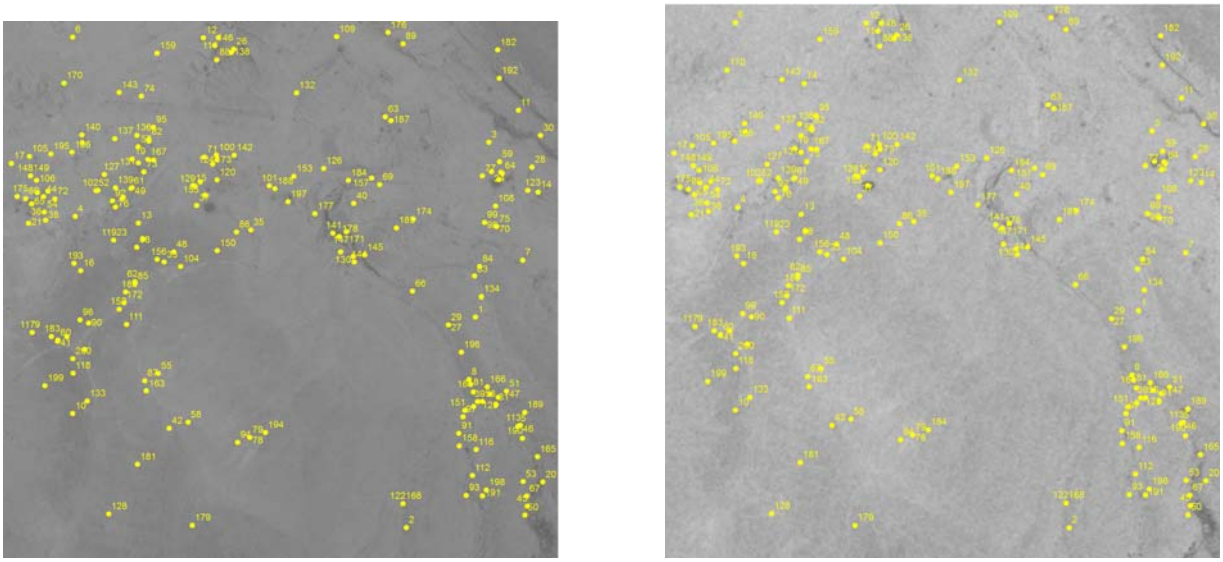

Figure 6-20: Tie point distribution in Rural Sample 10; IKONOS-2 Imagery (left) down sampled orthophoto (right)

6.1.2.3 SPOT-5 Imagery

The matching of 50-cm GSD aerial imagery with 2.5-m GSD SPOT-5 imagery presented a bigger challenge. The orthophoto image was down-sampled from 50-cm to 2.5-m pixel size using bilinear interpolation to match the resolution of SPOT-5 imagery. The processing for matching the SPOT-5 image samples with the corresponding aerial image samples proceeded smoothly and resulted in usual distributions of matched tie points.

For automated georeferencing through SURF-based processing, 9 different samples of 800 x 800 pixels were extracted from the SPOT image; four for agricultural sites, four for urban and one for a rural sites. An example of the distribution of the extracted key points and the matched tie points for an agricultural area sample is shown in Figure 6-21 and Figure 6-22. Similar key point and tie point distribution for an urban area and a rural area are shown in Figure 6-23 through Figure 6-26, respectively. Table 6-12 contains the number of extracted key points and tie points (note again that the maximum number of tie points was set to 200). The results at the Check Points are tabulated in Table 6-13.

#	Sample No.	Sensor	Area	Key Points Orthophoto	Key Points Satellite	Tie Points
1	Exp-IV-7-1	SPOT-5	Agricultural	1,027	676	200
2	Exp-IV-7-2	SPOT-5	Agricultural	1,101	716	200
3	Exp-IV-7-3	SPOT-5	Agricultural	1,134	631	200
4	Exp-IV-7-4	SPOT-5	Agricultural	588	1,010	200
5	Exp-IV-7-5	SPOT-5	Rural	924	583	200
6	Exp-IV-7-6	SPOT-5	Urban	1,258	817	186
7	Exp-IV-7-7	SPOT-5	Urban	1,160	816	200
8	Exp-IV-7-8	SPOT-5	Urban	1,287	799	200
9	Exp-IV-7-9	SPOT-5	Urban	1,239	779	200

Table 6-12: Key points and Tie points based on SURF-processing of SPOT-5 Imagery

SPOT-5 (2.5-m) Image No. 147-301 (Riyadh/2010)											
Agricultural				Urban				Rural			
Patch	RMSx (m)	RMSy (m)	Check Points	Patch	RMSx (m)	RMSy (m)	Check Points	Patch	RMSx (m)	RMSy (m)	Check Points
1	2.09	2.62	10	6	3.26	3.15	10	5	1.73	1.96	8
2	3.79	1.77	10	7	2.96	1.58	10	-	-	-	-
3	1.59	1.13	10	8	2.69	1.74	10	-	-	-	-
4	3.71	2.58	7	98	3.18	1.91	9	-	-	-	-
Mean	**2.80**	**2.03**	-	**Mean**	**3.02**	**2.10**	-	**Mean**	**1.73**	**1.96**	**-**
Average of all coordinate RMS values = 2.27 m											

Table 6-13: Examples of check point discrepancies based on SURF-processing of SPOT-5 imagery

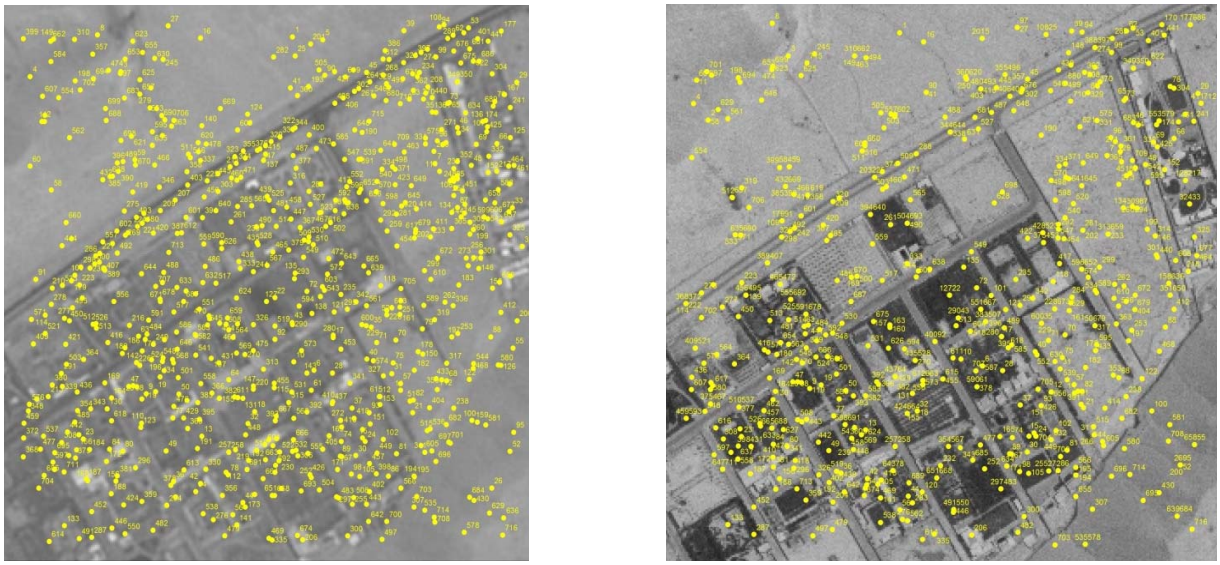

Figure 6-21: Key point distribution in Agricultural Sample 2; Riyadh SPOT-5 imagery (left); down sampled orthophoto (right)

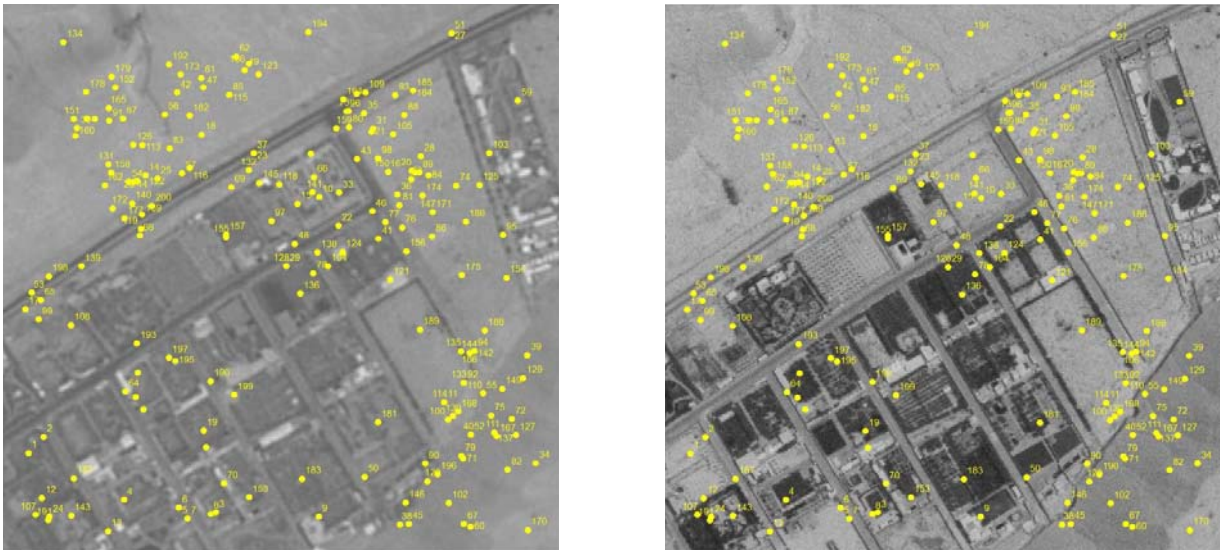

Figure 6-22: Tie point distribution in Agricultural Sample 2; Riyadh SPOT-5 imagery (left); down sampled orthophoto (right)

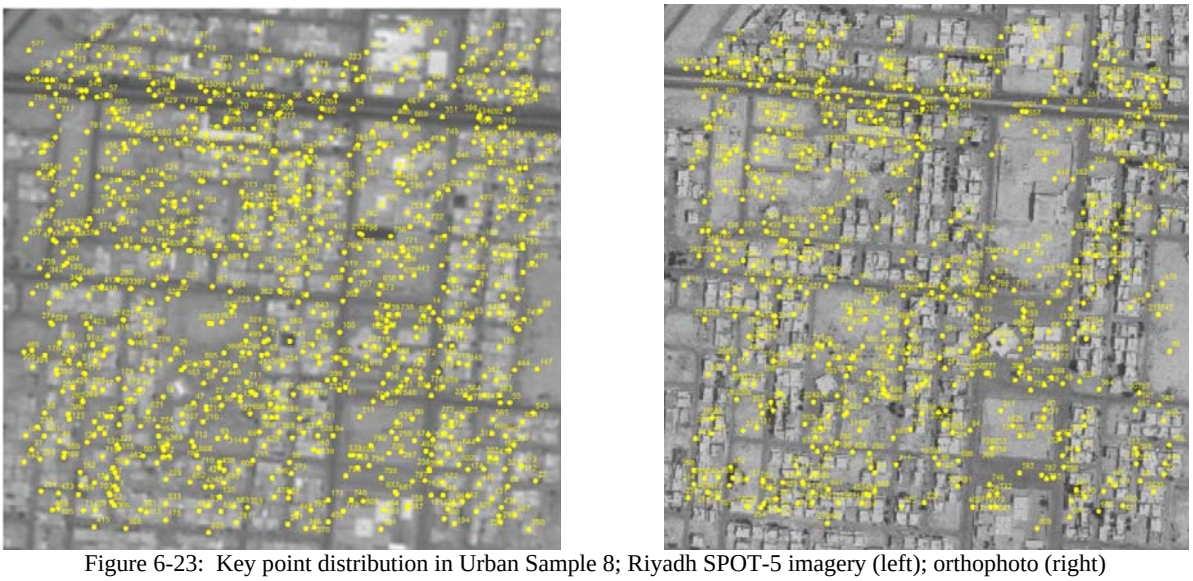

Figure 6-23: Key point distribution in Urban Sample 8; Riyadh SPOT-5 imagery (left); orthophoto (right)

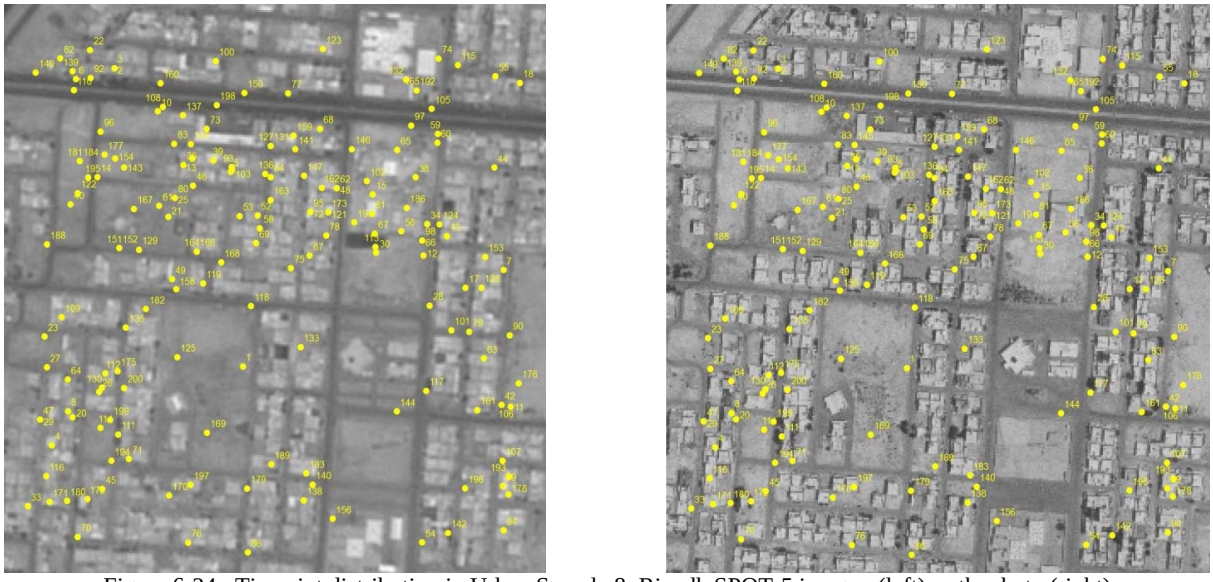

Figure 6-24: Tie point distribution in Urban Sample 8; Riyadh SPOT-5 imagery(left); orthophoto (right)

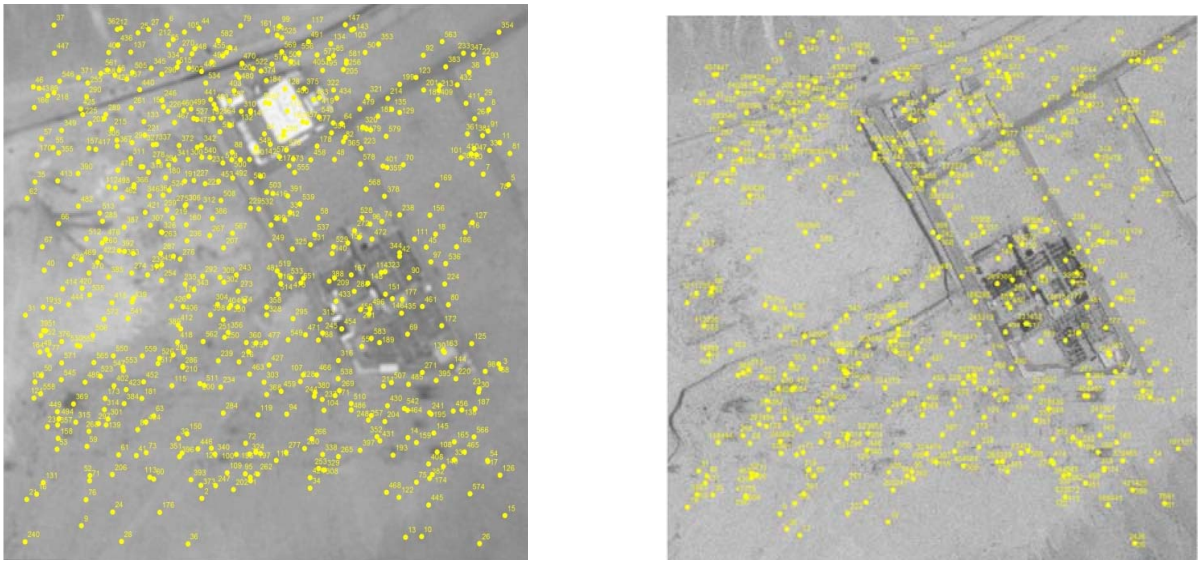

Figure 6-25: Key point distribution in Rural Sample 5; Riyadh SPOT-5 imagery (left); orthophoto (right)

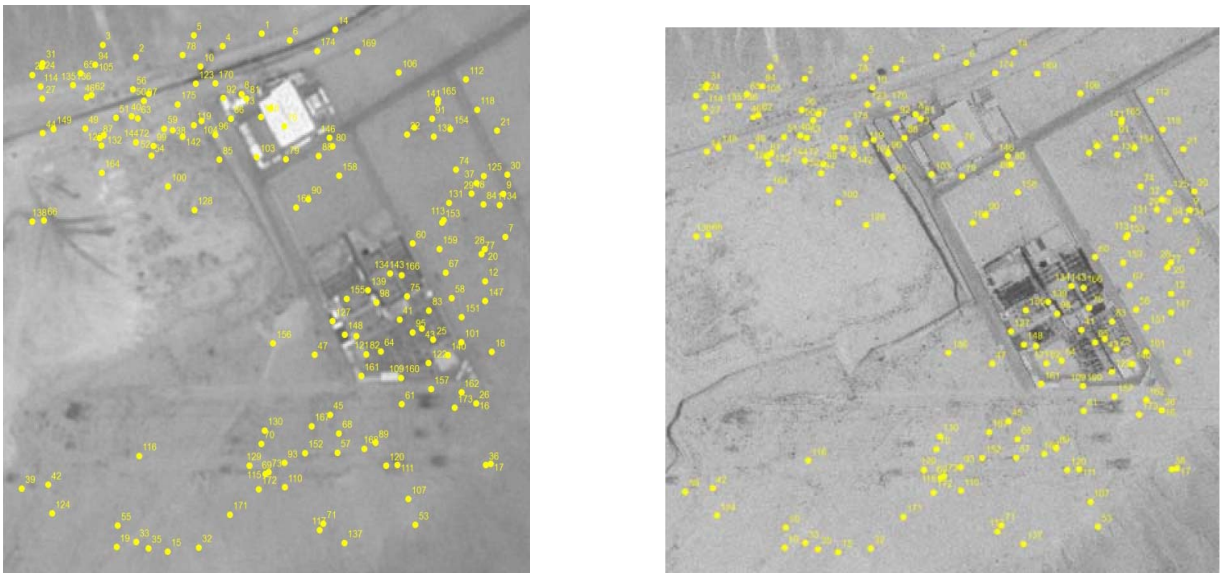

Figure 6-26: Tie point distribution in Rural Sample 5; Riyadh SPOT-5 imagery(left); orthophoto (right)

It was, however, noticed that in the case of SPOT-5 imagery, the matching with the aerial imagery resulted in a much larger number of mis-matched tie points. This is attributed to the large difference in the imaging resolution and the perspective geometry of the SPOT-5 imagery from the aerial imagery. Since both the satellite and the aerial image samples are georeferenced, large discrepancies in the UTM coordinates of corresponding tie points were filtered out as mismatched tie points. The RMSE in X- and Y-coordinates were computed and a threshold of three times the RMSE value was used for eliminating bad data points. Finally, the georeferencing of the satellite image was refined through a 2D Affine coordinate transformation, as had been done earlier for the GeoEye-1 and the IKONOS-2 imagery.

Based on the success in matching the IKONOS-2 and SPOT-5 satellite imagery with the down-sampled orthophoto, and in order to validate the scale-invariant characteristic of SURF, the Experiment IV was repeated by using the 50-cm GSD orthophoto without any down-sampling. The IKONOS-2 image No. 2418067 of Riyadh area acquired in 2010 (ST04 in Table 4-2) was processed. As before, an area covering 800 x 800 m was used for matching which corresponds with an 800 x 800 pixel size IKONOS-2 image, but a 1600 x 1600 pixel size orthophoto. As shown in Figure 6-27 to Figure 6-32 sufficient numbers of key points were matched without experiencing any matching problem. The results obtained on the check points are given in Table 6-15.

#	Image No	Sensor	Area	Key Points Orthophoto	Key Points Satellite	Tie Points
1	ExpIV-02-1	IKONOS	Agricultural	5,231	1,103	200
2	ExpIV-02-2	IKONOS	Agricultural	5,748	1,303	200
3	ExpIV-02-3	IKONOS	Agricultural	5,168	1,095	200
4	ExpIV-02-4	IKONOS	Urban	5,359	1,472	200
5	ExpIV-02-5	IKONOS	Urban	5,654	1,432	200
6	ExpIV-02-6	IKONOS	Urban	5,538	1,416	200
7	ExpIV-02-7	IKONOS	Rural	4,580	602	200
8	ExpIV-02-8	IKONOS	Rural	5,005	564	200
9	ExpIV-02-9	IKONOS	Rural	5,031	782	200

Table 6-14: Examples of number of Key points and Tie points based on SURF-processing of IKONOS-2 imagery

IKONOS-2 (1-m) Image No. 2418067_0010000 (Riyadh/2010)											
Agricultural				Urban				Rural			
Patch	RMS x (m)	RMS y (m)	Check Points	Patch	RMS x (m)	RMS y (m)	Check Points	Patch	RMS x (m)	RMS y (m)	Check Points
1	0.55	1.46	10	4	1.35	2.44	12	7	0.9	1.12	12
2	0.59	1.69	12	5	0.58	1.24	12	8	1.16	1.18	5
3	1.25	0.7	12	6	0.72	1.06	6	9	1.19	1.76	6
Mean	**0.99**	**1.28**	-	**Mean**	**0.86**	**1.51**	-	**Mean**	**0.91**	**1.3**	
Average of all coordinate RMS values = 1.14 m											

Table 6-15: Check Point discrepancies based on SURF-processing of IKONOS-2 imagery

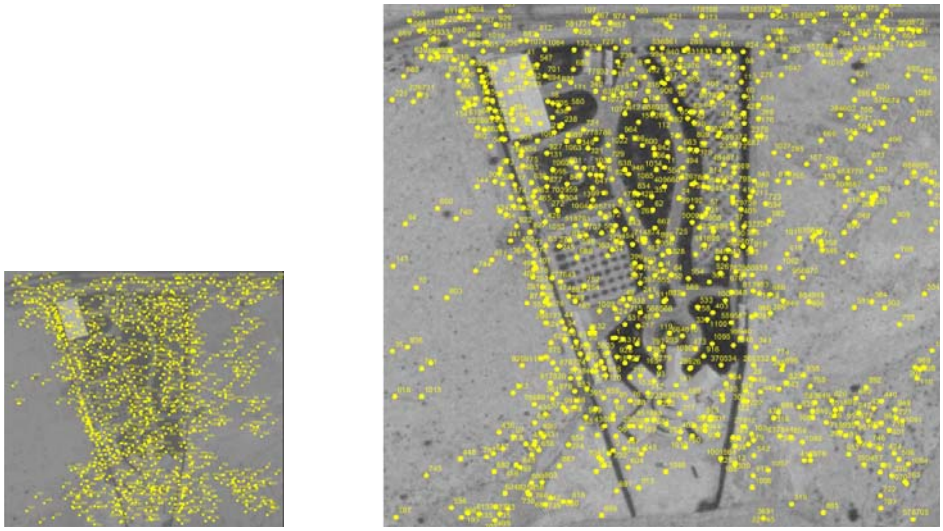

Figure 6-27: Key point distribution in Agricultural Sample 1; IKONOS-2 Imagery (left 1m GSD 800x800 pixels); orthophoto (right 50cm GSD 1600x1600 pixels)

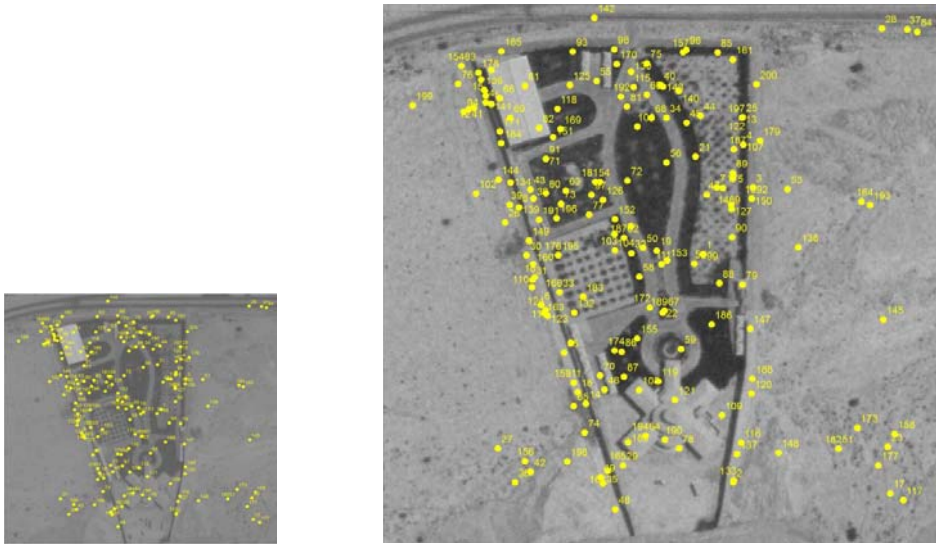

Figure 6-28: Tie point distribution in Agricultural Sample 1; IKONOS-2 Imagery (left 1m GSD 800x800 pixels); orthophoto (right 50cm GSD 1600x1600 pixels)

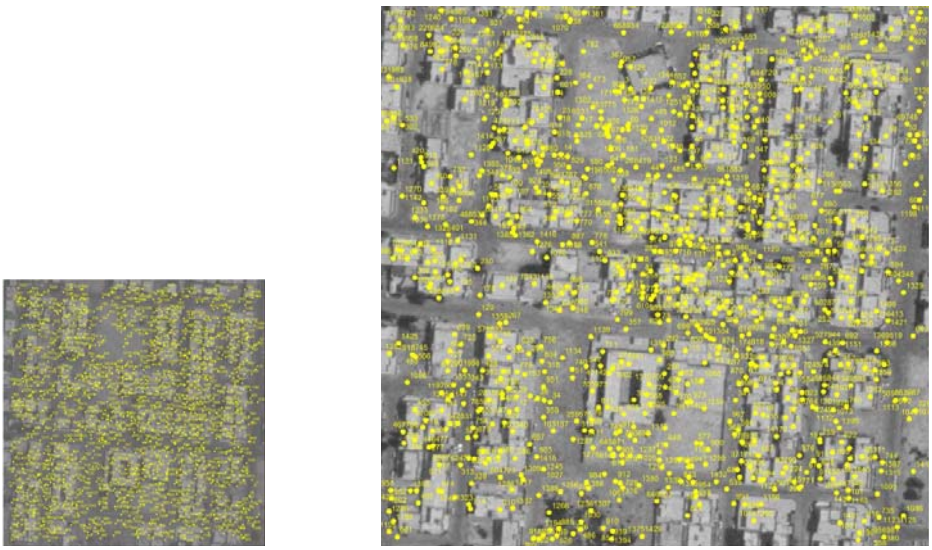

Figure 6-29: Key point distribution in Urban Sample 6; IKONOS-2 Imagery (left 1m GSD 800x800 pixels); orthophoto (right 50cm GSD 1600x1600 pixels)

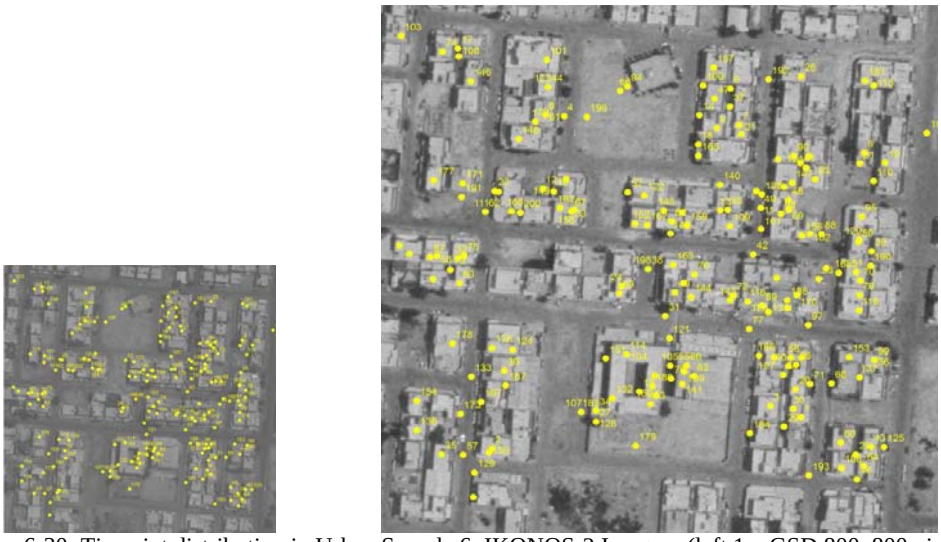

Figure 6-30: Tie point distribution in Urban Sample 6; IKONOS-2 Imagery (left 1m GSD 800x800 pixels); orthophoto (right 50cm GSD 1600x1600 pixels)

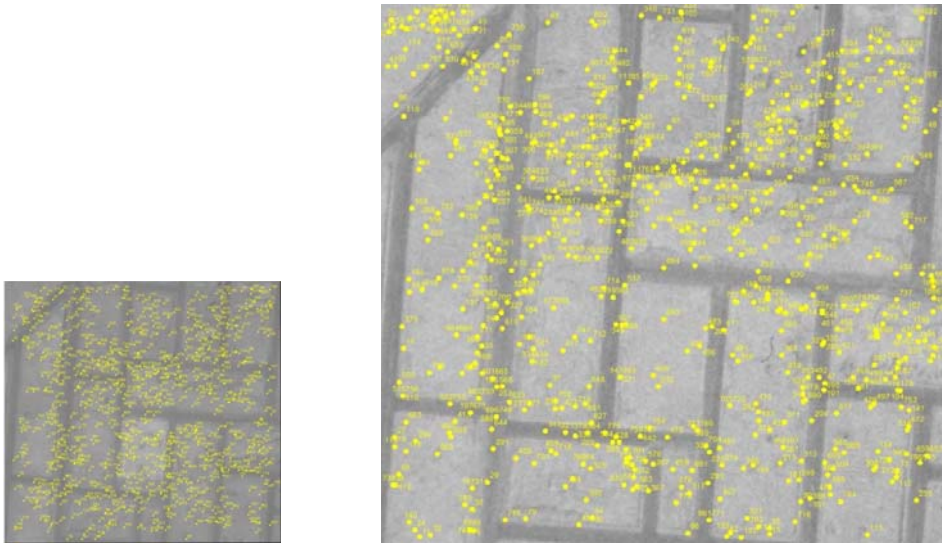

Figure 6-31: Key point distribution in Rural Sample 9; IKONOS-2 Imagery (left 1m GSD 800x800 pixels); orthophoto (right 50cm GSD 1600x1600 pixels)

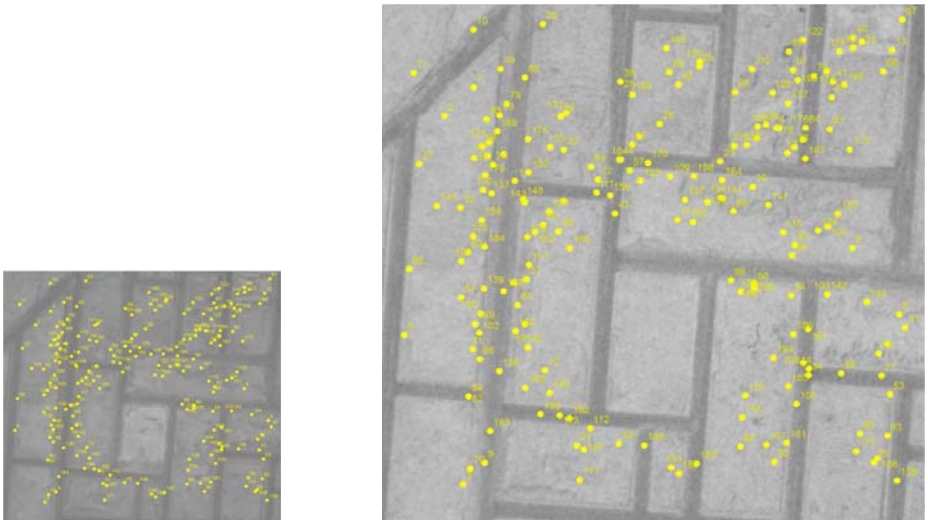

Figure 6-32: Tie point distribution in Rural Sample 9; IKONOS-2 Imagery (left 1m GSD 800x800 pixels); orthophoto (right 50cm GSD 1600x1600 pixels)

The results in Table 6-15 obtained without the down-sampling of orthophoto image to match with the 1-m GSD of IKONOS-2 image are comparable with the results of matching with the down-sampled orthophoto reported in Table 6.9. This convincingly demonstrates that the scale-invariant feature of the SURF algorithm can effectively accommodate a difference in image resolution by a factor of 2. However, there is a limit in the range of scale differences that SURF would accommodate since all efforts made in matchingthe50-cm GSD orthophoto with 2.5 m GSD SPOT-5 imagery (a scale factor of 5) using SURF algorithm were unsuccessful.

6.1.3 Results of Experiment II and III

This experiment was designed to evaluate the geometric accuracy with which common map features such as buildings, boundary walls, fences, roads, parcel boundaries, etc. can be extracted from georeferenced imagery using methods discussed in Experiment I and IV. Such features were first mapped from existing aerial orthophotos of 50-cm GSD and the X- and Y-coordinates of well-identifiable points along these features, such as building or fence corners, etc. (see Figure 5-4) were measured. The same features were then mapped using all the three types of satellite imagery viz., GeoEye-1, IKONOS-2 and SPOT-5 that had earlier been used in Experiments I and IV during this research, and the coordinates of the same feature points were also measured in the georeferenced satellite imagery. The RMS values for the difference in the X- and the Y-coordinate for the same map point are summarized in Table 6-16 below.

The Experiment III was designed to evaluate the ability for updating an existing map database with recently acquired high resolution satellite imagery that had been georeferenced using the approach demonstrated through Experiments I and IV. MOMRA has an on-going program for the production of both line maps and orthophoto maps at 1:10,000 scale that are generated from 1:45,000 scale aerial imagery using digital photogrammetric methods Accordingly, tests were performed for mapping new features to existing maps at scales ranging from 1:2,500 to 1:10,000 as described below.

The first test was performed by using the IKONOS-2 image No. 2411348_0000000 for the Riyadh area acquired in 2008. This was georeferenced using data from orthophotos (1:10,000 scale, 50-cm GSD) generated from 1:45,000 scale aerial imagery acquired in 2007. A comparison of the two images showed several changes that had occurred during this period of only one year. The digital map data for the new features was compiled from the georeferenced IKONOS-2 image as shown in Figure 6-33 (left), and the features were mapped to update the orthophoto shown in Figure 6-33 (right). These features were also added to update the 1:10,000 scale map shown in Figure 6-34. A similar example of updating the existing orthophoto and the map, both at 1:10,000 scale produced from 2007 aerial imagery using 2008 satellite imagery is shown on Figure 6-35 and Figure 6-36.

Satellite Imagery	Area	RMS x (m)	RMS y (m)
GeoEye-1 (50-cm)	Riyadh	0.78	0.59
	Al Muzahimiah	0.77	0.61
	Mean RMSE (m)	0.69	
IKONOS-2 (1-m)	Riyadh	1.32	1.01
	Huraymila	0.95	1.01
	Al Muzahimiah	1.08	1.67
	Mean RMSE (m)	1.17	
SPOT-5 (2.5m)	Riyadh	4.5	5.79
	Huraymila	2.84	1.8
	Al Muzahimiah	5.8	1.85
	Mean RMSE (m)	3.76	

Table 6-16: Summary of geometric mapping accuracy data

Figure 6-33: IKONOS-2 image (2008) and updated orthophoto (2007)

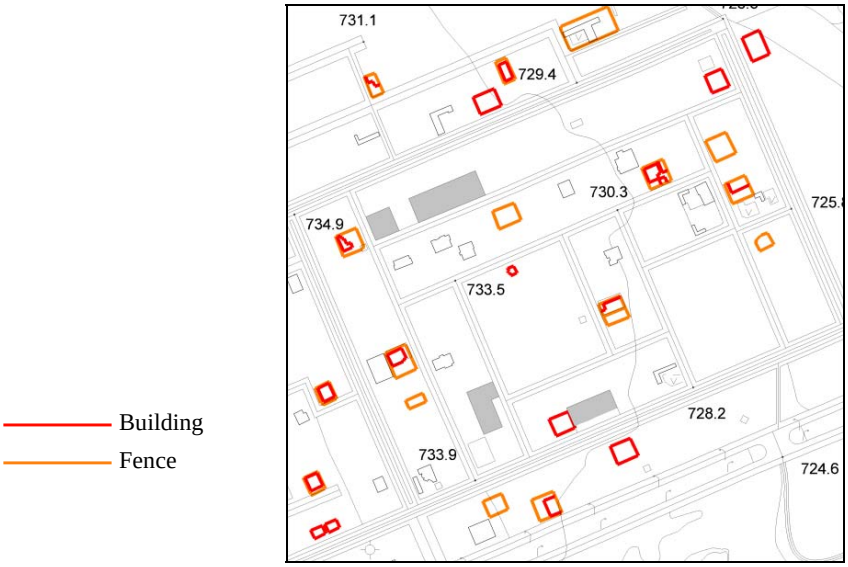

Figure 6-34: Updated existing 1:10,000 scale map (2007)

Figure 6-35: IKONOS-2 image (2008) and updated orthophoto (2007)

Figure 6-36: Updated existing 1:10,000 scale map (2007)

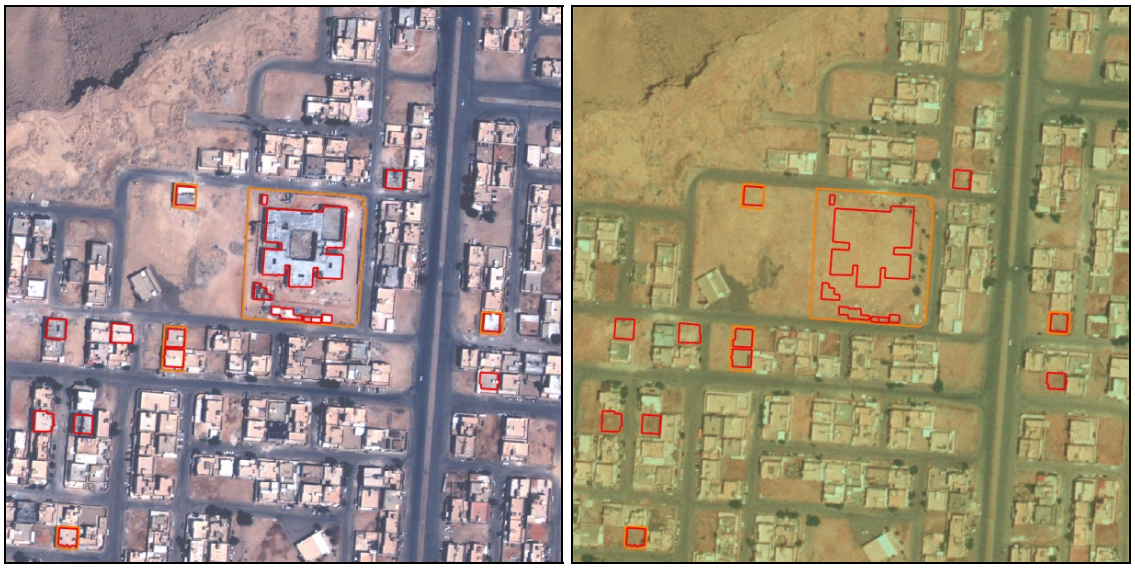

Figure 6-37: GeoEye-1 image (2010) and updated orthophoto (2007)

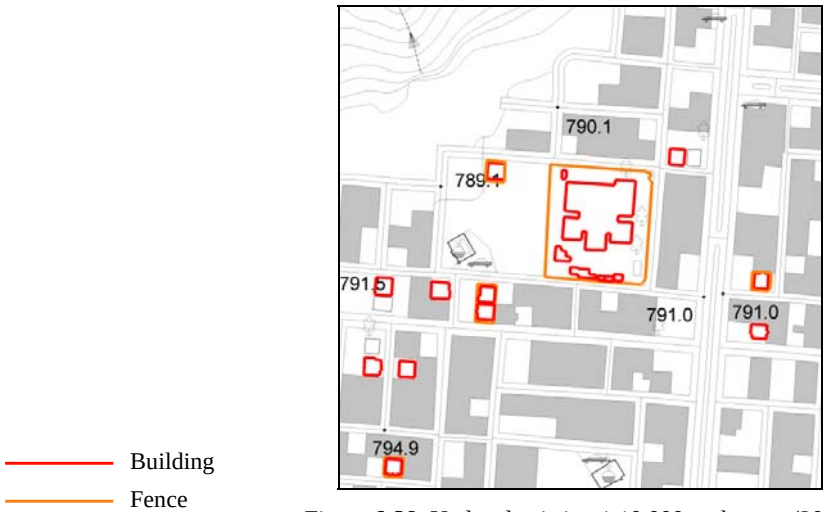

Figure 6-38: Updated existing 1:10,000 scale map (2007)

For comparison, the GeoEye-1 (50-cm) imagery, also of the Riyadh area, acquired in 2010 and georeferenced with an

existing orthophoto of 50-cm GSD generated from 1:45,000 scale aerial imagery flown in 2007, was used to update the 2007 orthophoto as well as the 1:10,000 scale map produced from 2007 aerial imagery. The results are shown in Figure 6-37and Figure 6-38.

Figure 6-39: IKONOS-2 image (2010) and updated orthophoto1:2,500 Scale (2007)

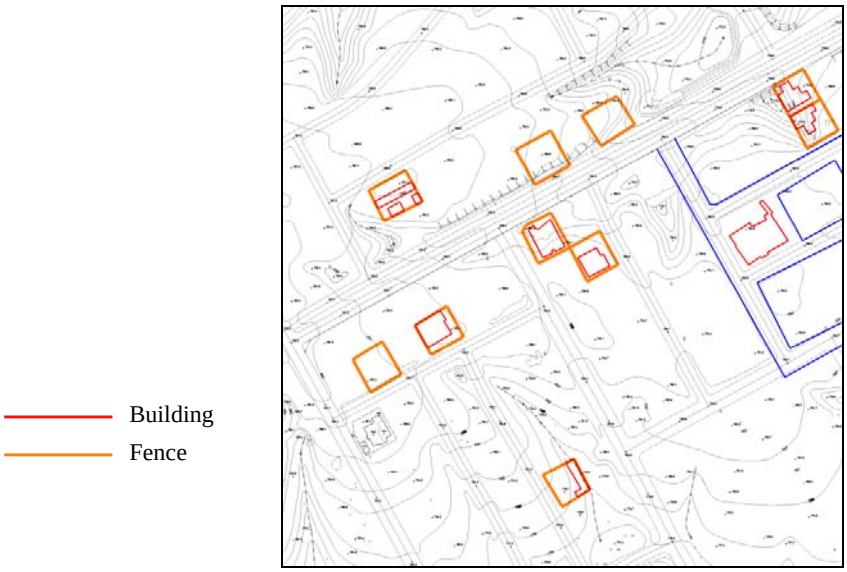

Figure 6-40: 1:2,500 scale map (2007) with updated features from IKONOS-2 (2010)

Even though the results of Experiment II summarized in Table 6-16 would not support the geometric accuracy requirements for HRSI mapping at very large scales, it seemed, nevertheless, of considerable interest to evaluate the result of updating a large scale map using georeferenced high resolution satellite imagery. Both line maps and orthophoto maps were available for the Huraymila area that had been produced from 1:5,500 scale aerial imagery acquired in 2007 in support of the Huraymila Pilot Cadastral Project. Unfortunately, the 50-cm GSD GeoEye-1 imagery was not available for this area; therefore, an IKONOS-2 image acquired in 2010 was used for this map updating test. The change in map data on the IKONOS-2 imagery is shown in Figure 6-39 (left), while the updated existing orthophoto at 1:2,500 scale and the map at 1:2,500 scale are shown in Figure 6-39 (right) and Figure 6-40, respectively.

Besides the updating of the existing map database, another objective of this research was to investigate the use of georeferenced satellite imagery to delineate land parcel boundaries for creating a cadastral fabric in support of the implementation of a Kingdom-wide cadastral registration system. An example showing the delineation of land parcel boundaries (in addition to updating other features) on a georeferenced GeoEye-1 satellite image acquired in 2010 is

illustrated in Figure 6-41 (left). The corresponding mapping of the land parcel boundaries on the existing 1:10,000 scale orthophoto is seen in Figure 6-41 (right)

Figure 6-41: Land parcel boundaries mapped on GeoEye-1 image (2010) and transferred on orthophoto (2007)

Extensive processing of satellite imagery listed in Table 4-2 has been carried out in support of Experiments I through IV and only representative data sets for various experiments and a summary of results have been presented in this Chapter. Complete data and results are included in Appendix-I. The discussion and the analysis of the experimental results are presented in the concluding Chapter.

Chapter 7. Analysis of Results and Conclusion

The results presented in the last Chapter have to be analyzed in order to answer the questions posed in Section 1.4.4, and consequently, to assess how far the objectives of this research have been achieved. Two of the questions, Q1 and Q2 are related to the geometric accuracy of georeferencing and the map data extracted from georeferenced satellite imagery and, therefore, will be discussed together. All the remaining three questions, Q3 through Q5 are related to the approach used towards automating the procedure for the georeferencing of satellite imagery and, therefore will be analyzed together.

7.1 Georeferencing and Mapping Accuracy

The results of Experiment I and II have to be analyzed in relation to the currently used map accuracy standards in MOMRA. The accuracy standards currently used for all photogrammetric map production in MOMRA are given in Table 7-1 (MOMRA, 2007). Only the positional accuracy standards are relevant to this research.

Map Scale for Phtogrammetric Data Compilation	Positional Error (m) Northing (1-σ level)	Positional Error (m) Easting (1-σ level)	Height Error (m) (1-σ level)
1:1,000	0.15	0.15	0.30
1:2,500	0.35	0.35	0.50
1:5,000	0.60	0.60	0.75
1:10,000	1.25	1.25	1.50
1:20,000	2.50	2.50	3.00

Table 7-1: MOMRA Map Accuracy Standards for Features

7.1.1 Discussion of Experiment I Results

Based on the georeferencing accuracy test results summarized for 50-cm resolution GeoEye-1 imagery in Table 6-1, for 1-m resolution IKONOS-2 imagery in Table 6-2 and for 2.5-m resolution SPOT-5 imagery in Table 6-3, the following observations can be made.

It is confirmed what has been widely known that the georeferencing of satellite imagery based solely on the vendor-supplied RPC data suffers from uncertain biases in the X and Y positional data. The results of Test I-A performed over a set of 19 different satellite images show a large variation in coordinate data bias that varies from a low value of 0.85 m for an IKONOS-2 image (ST11) to as high a value as 13.19 m, also for an IKONOS-2 image (ST19). Obviously, such a level of uncertainty about the accuracy in georeferencing would make such imagery unsuitable for extracting any mapping data. Consequently for mapping, it is necessary to supplement the RPC and the DTM data with ground control data for the orthoprojection of the satellite imagery. This approach was followed in carrying out Experiment I-B.

1. The results of the Experiment I-B listed in Table 6-1, Table 6-2 and Table 6-3 represent an outcome based on two different variables. The resolution of the satellite images varies from 50 cm to 2.5 m; the number of GCPs used varies from 5 to 15. Even though several investigations on the georeferencing accuracy of satellite imagery have in the past been based on the use of a very large number of GCPs such as 8 to 32 GCP (Zhang and Fraser, 2012) and 24 to 67 GCPs (Eisenbeiss et al., 2004), the maximum number of GCP in this study was fixed at 15 since the use of a larger dataset for GCP would have serious adverse impact in a map production environment.

In order to isolate the effect of the two variables, the $RMSE_X$ and the $RMSE_Y$ values were averaged for the same resolution imagery according to the number of GCPs used. Such averaged results are tabulated for the GeoEye-1, the IKONOS-2 and the SPOT-5 imagery in Table 6-4, Table 6-5 and Table 6-6 respectively.

2. Based on the data in Table 6-4, Table 6-5and Table 6-6, the following two effects are quite clear:
   (a) The georeferencing accuracy increases with the increasing number of GCP. This is valid for each of the three types of imagery with the different resolution tested. This trend in improving accuracy with the number of GCPs is more clearly visualized in Figure 6-1 and Figure 6-2 for the GeoEye-1 imagery, and in Figure 6-3 and Figure 6-4 for IKONOS-2 imagery. Similar trend in accuracy enhancement with increasing number of GCPs for the SPOT-5 imagery is seen in Figure 6-5. While the effect of adding as few as 5 GCP dramatically improves the georeferencing accuracy, further increase in the accuracy is not linear with the increasing number of GCP.
   (b) The achievable georeferencing accuracy increases with the increasing resolution of the satellite imagery. This is evident from the range from 0.41m to 0.79m for the RMSE of X- and Y-coordinate for the GeoEye-1 imagery. The corresponding range in the coordinate error is from 0.75m to 1.16m for the IKONOS-2 imagery and 1.41m to 1.81mfor the SPOT-5 imagery.

7.1.2 Discussion of Experiment II Results

The Experiment II aimed at investigating the geometric accuracy with which point map features such as building corners, boundary walls and fence corners and similar features can be manually mapped from georeferenced satellite imagery of differing resolution. The results are given in Table 6-13. As expected, the highest geometric accuracy of mapping is achieved by using the highest resolution (50-cm) GeoEye-1 imagery and the mapping accuracy is lowest in the case of 2.5-m SPOT-5 imagery.

It is important that the results of Experiment I and Experiment II discussed above must be interpreted in the context of the quality of the control data used for the experiments. As described in Section 1.4, the objective of this study is to rapidly update the existing map data with recently acquired satellite imagery that can be georeferenced using existing database as control. The following considerations lead to the selection of the existing database of orthophoto imagery which was selected as the most appropriate control database for this study:

- The orthophoto image has 50-cm resolution that matches the highest resolution of GeoEye-1 satellite imagery used in this study.
- The orthophoto database covers all the towns and settlements of Saudi Arabia

The orthophoto imagery has been generated from analog wide-angle aerial imagery of scale 1:45,000, which was scanned at 14 micrometer resolution providing around 60-cm resolution for digital photogrammetric processing of aerial triangulation (AT) blocks. After AT, the controlled imagery was used for the production of line maps as well as orthophoto maps at 1:10,000 scale. During orthoprojection, the imagery was resampled to 50-cm GSD.

In accordance with MOMRA map accuracy standards given in Table 7-1, the control point data measured on the orthophoto can have absolute positional error from 1-m to 1.25-m in planimetry. The results for the mapping accuracy given in Table 6-16, therefore, should be interpreted as the positional accuracy of the mapped features relative to the control data used. The answer to the following Q.1 should be sought in this light:

Q1: What is the largest scale for mapping from HRSI of 0.5 meter GSD? Also, what is the largest scale for mapping from HRSI of 2.5 meter GSD?

The answer would be that the largest scale for mapping from HRSI of 0.5 meter GSD that has been georeferenced using control data extracted from existing 50-cm resolution orthophotos is 1:10,000 or even 1:5,000 if the uncertainty of the reference is taken into account . The above Q.1 does not refer to the 1 meter resolution IKONOS-2 imagery that was also

included in Experiment I and II. Based on the results for IKONOS-2 in Table 6-16, the largest scale for mapping from HRSI of 1 meter resolution that has been georeferenced using control data extracted from existing 50-cm resolution orthophotos is 1:10,000. The result reported in Table 6-16, for 2.5 meter GSD SPOT-5 imagery does not fulfill the map accuracy requirement even for the scale 1:20,000 which is the smallest mapping scale used in MOMRA.

It should, however, be noted that the accuracy of existing orthophoto data as control has primarily influenced the answer to Q.1. When control data with higher accuracy is used, mapping accuracy at the pixel level or even sub-pixel level is achievable (Fraser and Hanley, 2003; Eisenbeiss et al., 2004). Under this scenario, 50-cm GSD GeoEye-1 imagery and 1-m GSD IKONOS-2 imagery may be used for mapping at scales ranging between 1:5,000 and 1:10,000 to meet MOMRA map accuracy standards.

In order to consistently achieve the desired map accuracy, it is necessary to answer the following question Q.2:

Q2: What should be the accuracy, number and spatial distribution of GCPs for the largest scale for mapping from HRSI of 0.5 meter GSD? What should be the accuracy, number and spatial distribution of GCPs for the largest scale for mapping from HRSI of 2.5 meter GSD?

As pointed out earlier, georeferencing accuracy at sub-pixel level has been reported but this has mostly been the case to demonstrate what may be possible under controlled and optimal conditions. In a map production routine environment, it is reasonable to aim at pixel level georeferencing accuracy; this corresponds to an accuracy of 50 cm, 1 m and 2.5 m for GeoEye-1, IKONOS-2 and SPOT-5 imagery, respectively. Therefore, in accordance with the National Spatial Standards for Data Accuracy (NSSDA) currently followed in the United States, that have also been adopted by MOMRA, the control data should be at least three times more precise than the map data, if the control data is to be considered errorless (FGDC, 1998). This corresponds with a positional accuracy in each coordinate for control data not to exceed 15 cm for HRSI of 50-cm GSD, and not to exceed 30 cm for HRSI of 1-m GSD and not to exceed 75 cm for HRSI of 2.5-m GSD.

Unlike the positional accuracy of the control data, it is very difficult to relate the use of a definitive number of GCP with the achievable accuracy of HRSI. Unlike aerial imagery which displays fairly homogenous geometric characteristics, HRSI acquired through push broom line scanners represents perspective projection along the line and parallel projection across; each line having its own set of exterior orientation elements. This may result in somewhat non-systematic image distortions across the scene. This is corroborated by the results observed in Experiment I-B, where the coordinate residuals in the check points do not display any systematic pattern. Consequently, the spatial distribution of the GCP over the satellite image has a more significant impact on the georeferencing accuracy. Based on the results of Experiment I-B, about 10 to 15 GCPs that are evenly distributed along the perimeter and the interior of the image would lead to the optimal level of georeferencing accuracy at pixel level.

Mapping Scale	**Limiting Positioning Error (m)**	**HRSI Resolution GSD (m)**	**Ground Control Points**	
			Number	**Accuracy**
1:5,000	0.60	0.50 - 0.60	15	0.15 - 0.20
1:10,000	1.25	1.00 - 1.25	15	0.30 - 0.45
1:20,000	2.50	1.00 - 1.25	15	0.30 - 0.45

Table 7-2: Proposed Georeferencing Specifications for mapping from HRSI

7.2 Automation in the georeferencing process

The procedure currently used in MOMRA for georeferencing a satellite image is based on the orthoprojection of the satellite image using the vendor-provided RPCs combined with DTM data and by manually identifying and measuring about 5 to 10 ground surveyed control points. Considerable time, labour and cost are involved in the collection of the ground control data. Consequently, the primary interest of this research study is to use the existing orthophoto database information in MOMRA instead of traditional ground control for the georeferencing of the recently acquired satellite imagery using an automated approach in order to speed up the georeferencing process. With this objective, the Experiment IV described in Section 5.4 was designed to use an existing database of 50-cm GSD aerial orthoimagery to fulfill the role of field-surveyed ground control.

The results of Experiment IV reported in Section 6.1.2 are based on the matching of aerial orthoimagery of 50-cm GSD that was acquired during 2007 with the set of satellite imagery listed in Table 7-3 below by using an automated image matching approach based on the SURF algorithm. Therefore, the test results reported in Table 6-8 and Table 6-9 for the GeoEye-1 imagery, in Table 6-11 for the IKONOS-2 imagery and in Table 6-13 for the SPOT-5 imagery are fully representative of the capability of the proposed SURF-based approach for matching multi-scale, multi-sensor and multi-season imagery. In addition, for each type of satellite imagery used, samples of 800 x 800 pixels were extracted to represent a wide range in urban, agricultural and rural landscape.

Satellite Imagery	GSD (m)	Season	Landscape Sample		
			Urban	Agricultural	Rural
GeoEye-1	0.50	Sep-09	3	2	1
GeoEye-1	0.50	Jan-10	5	5	5
IKONOS-2	1.00	Jan-10	5	4	1
SPOT-5	2.50	Jun-10	4	4	1

Table 7-3: Variety of satellite image samples used for SURF-based matching test

Based on the results listed in Table 6-8 through Table 6-13, the following observations may be made about the satellite imagery georeferencing approach demonstrated in Experiment IV:

1. The use of the proposed SURF-based matching of the GeoEye-1, IKONOS-2 and SPOT-5 imagery with 50-cm GSD aerial orthoimagery, followed by a 2D Affine coordinate transformation, can provide georeferencing accuracy that matches, or even exceeds the accuracy achieved through manual selection of control data, as demonstrated in Experiment I-B.

2. GeoEye-1 and IKONOS-2 satellite imagery when georeferenced by using the proposed automated approach can be used for mapping at scale 1:10,000 to meet MOMRA map accuracy standards.

3. In the case of SPOT-5 satellite imagery, the proposed automated georeferencing approach can result in an accuracy that meets MOMRA map accuracy standard for mapping at scale 1:20,000. The RMSE of 2.27 m reported in Table 6-13 is a significant improvement over the corresponding mapping RMSE of 3.76 m resulting from Experiment-II as reported in Table 6-16. This is due to the fact that the map data for the Experiment-II was extracted from a full 60 km x 60 km SPOT-5 image that had been georeferenced by using only 15 points covering such a large area. In comparison, significant improvement in the accuracy was achieved by using only

a 800 x 800 pixel subset of the SPOT-5 image.

4. Based on the testing of 40 different image scenes with the proposed automated georeferencing approach, the last three questions posed in Section 1.4.4, as given below can now be addressed:

Q3: What image matching approach will be optimal for use?

The test results from Experiment-IV have convincingly demonstrated that SURF provides a very effective image matching approach for multi-scale, multi-sensor and multi-season image matching. After the input image files have been identified, the matching proceeds fully automatically without human interaction. For the samples of 800 x 800 pixels tested, the processing time was only 2 to 2.5 minutes on a PC workstation. In comparison, it takes an average of about 4 hours for an average trained operator to select and measure 15 control points on the aerial and the corresponding satellite imagery.

Q4: What 2D transformation model will be most effectively applicable?

The vary nature of the pushbroom scanner geometry results in uneven image distortions in along-track and cross-track directions in satellite imagery. Therefore, the 2D Affine coordinate transformation is best suited model to correct for the resulting distortions. As pointed out in Chapter 3, the use of the vendor-provided RPC data often results in residual systematic errors in the interior and the exterior orientation that often result in biases in X- and Y-coordinates. These are effectively corrected by the two shift parameters that have the dominating influence on the transformation. In fact, it may often be sufficient to simply apply the two shift parameters. In this study, the matching and the 2D Affine transformation steps were combined in a single process.

Q5: What should be the rejection threshold(s) for poorly matched points?

The proposed method of SURF matching permits the use of the distance between the key points as a criterion for the rejection of poorly matched key points. The distance threshold for rejection is specified by the user before initiating the matching process. Setting a large threshold value for the distance, such as for example 15 to 20 pixels, results in a larger number of key points. If the distance threshold is overly constrained, such as 5 pixels, the numbers of key points are greatly reduced and also, may be unevenly distributed in the image. All the data for the Experiment IV was obtained by using a distance threshold of 15 to 20 pixels that often resulted in a large number of matched points from which the best-matched 200 points were automatically selected.

As described earlier, the proposed method for georeferencing the satellite imagery subsequently transforms the satellite image to the aerial orthoimage through a 2D Affine coordinate transformation. This presents another opportunity to filter out poorly matched key points before obtaining the least squares based coordinate transformation solution. The use of a statistical numeric based on the RMSE in the X- and the Y-coordinate of the matched points provides a logical approach to filter out poorly matched points. Under the assumption of a normal distribution of the data errors, all points with X-coordinate or Y-coordinate differences that exceed 3 times the $RMSE_X$ and $RMSE_Y$, respectively, may be rejected. Such a threshold was used for rejecting poorly matched points in this study. However, in the case when many matched points get rejected, it may be advisable to relax this threshold value to 4 times the $RMSE_X$ and $RMSE_Y$, because the number and the distribution of the matched points are critical for obtaining a reliable coordinate transformation solution.

This concludes the analysis of the results of the practical experiments carried out in this research study and based on the above discussion, some relevant conclusions and comments about future prospects are presented in the following section.

7.3 Conclusions and Future Prospects

7.3.1 Conclusions

Like most nation-wide mapping agencies, MOMRA faces the challenge to maintain and deliver map data that meets the very diverse needs of a wide variety of map data users. The conventional map data at scale 1:1,000 demands very high geometric accuracy for engineering and urban design and for providing municipal services by over 220 municipalities spread over 14 regions in Saudi Arabia. In comparison, the aerial orthoimage maps are primarily used as visual tools for engineering and land-use planning at the local and regional levels. For such map data, the currency and the completeness of map data are far more important features than the geometric accuracy. In this context, the line maps and the orthoimage maps produced at scale 1:10,000 are most commonly used for regional planning, while line maps at scale 1:2,500 (as a derived map product from 1:1,000 scale map data) are most often needed for municipal land-use planning. Consequently, the maintenance of map data at these two scales by MOMRA will serve the needs of a large number of national and regional government agencies and the municipalities in Saudi Arabia. Accordingly, any conclusions about the impact of this research study on the enhanced capability of MOMRA for rapidly updating map data with the use of recently acquired high resolution satellite imagery should be drawn in the light of map data needs mentioned above.
Based on the analysis of the data resulting from Experiments I through IV, the following conclusions can be drawn:

1. The existing aerial 50-cm resolution orthoimage database that meets MOMRA standards for map accuracy at 1:10,000 scale can effectively be used as control for georeferencing of recently acquired satellite imagery of 50-cm to 1-m resolution to generate the following map data products that meet MOMRA map accuracy standards:
    - Updated 1:10,000 scale line maps
    - Orthoprojected 50-cm resolution satellite image at 1:10,000 scale as an updated replacement for the existing orthoimage map
2. In order to generate the map products mentioned in item-1 above, coordinate data for 15 or more control points that are well distributed over the image, may be obtained through manual measurements on the existing orthoimage and the new satellite image and combined with the RPC and DTM data for the orthoprojection of the satellite image. About 4 to 5 hours of a trained operator time is required to complete this process.
3. A more efficient alternative for the georeferencing of the new satellite image is to orthoproject the new satellite image based only on the vendor-supplied RPC data and DTM data in order to obtain an approximately georeferenced satellite image. This process can usually be completed within one hour. This approximately georeferenced image is then matched with the corresponding existing orthoimage using the proposed SURF-based matching approach that generates a large number of matched points. These points are subsequently used to transform the satellite image to the orthoimage through a 2D Affine coordinate transformation. The SURF matching and the coordinate transformation processing only takes a few minutes and results in a georeferenced satellite image that meets MOMRA map accuracy standards for 1:10,000 map scale.
4. This research has demonstrated that the georeferencing of a new satellite image can be carried out at a production rate of 5 to 7 satellite images in one day without the need for any field control surveying nor any measurement of image coordinate data by a skilled operator. Hence a viable solution for a semi-automated procedure for orthophoto generation that can be effectively implemented in MOMRA map production environment is now available, in complete fulfillment of the primary objective for this research.

5. Based on the currently available 50-cm resolution orthoimagery that has been generated from 1:45,000 scale aerial imagery, the proposed semi-automated procedure can be used for generating orthophotos that meet the MOMRA accuracy standard for 1:10,000 map scale. However, if orthoimagery of higher positional accuracy becomes available for control, the proposed procedure will be equally applicable for generating orthophoto of correspondingly higher accuracy.

6. There are several uses of map data where the completeness and the validity of the map data is of primary interest while the geometric accuracy is of secondary importance. For example, due to the rapid pace of urbanization in Saudi Arabia, the planning for continuing urban development requires frequent updating of the land-use map data which is most commonly compiled from MOMRA's 1:2,500 scale map database. Such land-use planning can be greatly facilitated if MOMRA can rapidly deliver map data that has been updated using recently acquired satellite imagery such as, for example, shown in Figure 6-33 to Figure 6-38 that captures the changes in the urban infrastructure, The fact that in this case, the new mapped features do not meet MOMRA's geometric map accuracy standards for 1:2,500 scale is not of concern for land-use planning; they represent topologically correct current information.

7.3.2 Future prospects

Recently, MOMRA has made a major change in its specifications for the acquisition of aerial imagery by using digital frame aerial cameras. Since last year, digital aerial imagery of 10-cm GSD has been acquired for the entire urbanized area in Jeddah Region using UltraCam XP digital aerial camera. This has been supplemented with coverage at 20-cm GSD for the remaining rural and mountainous areas of the Region. The 20-cm GSD digital imagery is currently being processed for the production of orthophoto at scale 1:2,500, and orthophoto maps and line maps are being generated from the 10-cm GSD digital aerial imagery.

Based on the experience and insights gained in this research and the resulting data from the practical experiments, it can be confidently concluded that by matching the 50-cm GSD satellite imagery (such as GeoEye-1 or equivalent) with the 1:2,500 scale orthophoto generated from 20-cm GSD UltraCam imagery using the proposed SURF-based matching procedure should provide updated map data that meets MOMRA map accuracy standard for the scale 1:2,500. This will enable MOMRA to rapidly respond to any requests for the delivery of updated map data at scales ranging from 1:2,500 to 1:10,000 that fully meet MOMRA map accuracy standards. It will, of course, be subject to the timely availability of recently acquired satellite imagery of appropriate resolution.

References

Abdel-Aziz and Karara, H. 1971. Direct linear transformation from comparator coordinates into object space coordinates in close-range photogrammetry, Proceedings of the Symposium on Close Range Photogrammetry, American Society of Photogammetry, Falls Church, USA.

Alobeid A., Jacobsen K., Heipke C. and Al Rajhi M. 2011.Building Monitoring with Differentials DSMS.

Alrajhi, M. and Hawarey, M. 2008.Comprehensive geo-spatial data creation for the Kingdom of Saudi Arabia, Proceedings EGU General Assembly 2008.

Baltsavias, E., Li, Z. And Eisenbeiss, H. 2006. DSM Generation and Interior Orientation Determination of IKONOS Images Using a Testfield in Switzerland.Photogrammetrie, Fernerkundung, Geoinformation, 10(1). pp. 41-54.

Bay, H., Tuytelaars, T. and Van Cool, L. 2006. SURF: Speeded up robust features, Proceedings of the European Conference on Computer Vision, 2006: 404-417

Bay, H., Ess, A., Tuytelaars, T. and Van Cool L., 2008. Speeded-Up Robust Features (SURF).Computer Vision and Image Understanding, Vol. 110, No. 3: 346-359.

Brown, M. and Lowe, D. 2002. Invariant features from interest point groups. Proceedings of the 13th British Conference on Computer Vision, 2002: 253-262.

Di, K., Ma, R. and Li, R.X., 2003. Rational functions and potential for rigorous sensor model recovery. PhotogrammetricEngineering and Remote Sensing, 69 (1): 33-41.

Dowman, I. and Dolloff, J.,2000. An evaluation of rational functions for photogrammetric restitution. International Archives of Photogrammetry and Remote Sensing, 29(B3): 254-266.

Dowman, I., Jacobsen, K., Konecny, G. and Sandau, R., 2012. High Resolution Optical Satellite Imagery.Whittles Publishing, Caithness, UK.

Ebner, H., Kornus, W., Ohlhof, T. and Putz, E., 1999.Orientation of MOMS-02/D2 and MOMS-2P/PRIRODA imagery.ISPRS Journal of Photogrammetry and Remote Sensing, 54: 332-341.

Ebner, H. and Müller, F. 1986: Processing of Digital Three Line Imagery Using a Generalized Model for Combined Point Determination, ISPRS Comm.III Symposium in Rovaniemi, 11 pages.

El-Manadili, Y.S. and Novak, K., 1996.Precision rectification of SPOT imagery using the direct linear transformation model.Photogrammetric Engineering and Remote Sensing, 62 (1): 67-72.

FGDC, 1998. Geospatial Positioning Accuracy Standards, Part 3: National Standard for Spatial Data Accuracy. Federal Geographic Data Committee Publication FGDC-STD-007.3-1998

Fonesca, L.M.G. and Manjunath, B.S., 1996. Registration techniques for multisensor remotely sensed imagery. Photogrammetric Engineering & Remote Sensing, Vol. 62, No. 9, pp. 1049-1056.

Fraser, C. and Shao, J., 1996. Exterior orientation determination of MOMS-02 three-line imagery: experiences with the Australian test field data. International Archives of Photogrammetry and Remote Sensing, 31 (Part B3): 207-214.

Fraser, C.S., Hanley, H.B. and Yamakawa, T., 2002.Three-dimensional geopositioningaccuracy of IKONOS imagery.Photogrammetric Record, 17 (99): 465-479.

Fraser, C.S. and Hanley, H.B., 2003. Bias compensation in rational functions for Ikonos satellite imagery.Photogrammetric Engineering and Remote Sensing, 69 (1): 53-57.

Fraser, C.S. and Yamakawa, T., 2004.Insights into the affine model for high-resolution satellite sensor orientation.ISPRS Journal of Photogrammetry and Remote Sensing, 58: 275-288.

Fraser, C.S. and Hanley, H.B., 2005. Bias-compensated RPCs for sensor orientation ofhigh-resolution satellite imagery. Photogrammetric Engineering and RemoteSensing, 71 (8): 909-916.

Fraser, C.S., Dial, G. and Grodecki, J., 2006. Sensor orientation via RPCs. ISPRS Journal of Photogrammetry and Remote Sensing, 60 (3): 182-194.

Ghioca-Robrecht, D.M., Johnston, C.A. and Tulbure, M.G., 2008. Assessing the use of multiseasonQuickBird imagery for mapping invasive species in a Lake Erie coastal marsh, WETLANDS, Vol.28, No. 4: 1028–1039.

Gianinetto, M. 2008. Updating Large Scale Topographic Databases in Italian Urban Areas with SubmeterQuickBird Images, International Journal of Navigation and Observation Volume 2008: 116-124.

Gleyzes, J.-P., Meygret, A., Fratter, C., , C., Baillarin, S., Valorge, C., 2003. SPOT5: System overview and image ground segment. IGARSS 2003, Toulouse, France (on CDROM).

Greve, C.W., Molalander, C.W. and Gordan, D.K. 1992. Image processing on open systems, PE&RS, Vol. 58, No. 1: 85-89.

Grodecki, J. and Dial, G., 2001. IKONOS geometric accuracy.Proceedings of Joint ISPRS Workshop 'High-Resolution Mapping from Space 2001', Hannover, Germany, 19-21 September.

Grodecki, J. and Dial, G., 2003. Block adjustment of high-resolution satellite imagesdescribed by rational polynomials. Photogrammetric Engineering and RemoteSensing, 69 (1): 59-70.

Gugan, D.J. and Dowman, I.J., 1988. Accuracy and completeness of topographic mappingfrom SPOT imagery.Photogrammetric Record, 12 (72): 787-796.

Hoffman, O., Nave, P., Ebner, H. (1982): DPS A, Digital Photogrammetric System for Producing Digital Elevation Models and Orthophotos by Means of Linear Array Scanner Imagery. In: ISPRS Nr. 3, 24. Jg., S. 216-277.

Holland, D.A., Boyd, D.S. and Marshall, P. 2006. Updating topographicmapping in Great Britain using imagery from high-resolution satellite sensors, In ISPRS Nr.3, 60.212-223.

http://www.cnes.fr/web/CNES-en/3236-pleiades.php, accessed date (June, 2011).

http://www.digitalglobe.com/downloads/QuickBird-DS-QB-Web.pdf, accessed date (June, 2011).

http://www.geoeye.com/CorpSite/, accessed date (June, 2011).

http://www.isro.org/satellites/cartosat-2.aspx , accessed date (June, 2011).

http://www.kari.re.kr/data/eng/contents/Space_001.asp?catcode=1010111000&depthno=0 , accessed date (June, 2011).

INPHO, 2008. MATCH-AT User Guide, Stuttgart, Germany

Jacobsen, K., 2006. Calibration of imaging satellite sensors.International Archives of Photogrammetry and Remote Sensing, 36 (Part 1/W41).

Jacobsen, K., 2008. Geometric modelling of linear CCDs and panoramic imagers. In: Li, Z.; Chen, J.; Baltsavias, E.

(Hrsg.): Advances in Photogrammetry, Remote Sensing and Spatial Information Science. London: Taylor and Francis, 145-155.

Jacobsen, K. 2012. Program SIFTCOR: Search for corresponding key points for matching by SIFT, Institute of Photogrammetry and GeoInformation, Leibniz University Hannover.

Jedryczka, R. 1999. Contribution to OEEPE-test on automatic orientationof aerial images, Task A-Semi-Automatic Exterior Orientation Using Existing Vector Map Data, EuropeanOrganization for Experimental Photogrammetric Research,Vol. 36:133–137.

Juan, L. and Gwun, O. 2009. A comparison of SIFT, PCA-SIFT and SURF, International Journal of Image Processing, Vol.3, Issue 4:143-152.

Karjalainen, M. and Kuittinen, R.1999.Contribution to OEEPE-test on automatic orientationof aerial images, Task A-Interactive Exterior Orientation Using Linear Features from Vector Maps, EuropeanOrganization for Experimental Photogrammetric Research,Vol. 36:127–131.

Kim, T. and Dowman, I., 2006. Comparison of two physical sensor models for satellite images: position-rotation model and orbit-attitude model. The Photogrammetric Record, 21 (114): 110-123.

Kocaman, S. And Gruen, A., 2008. Geometric Modeling and Validation of ALOS/PRISM imagery and Products.International Archives of Photogrammetry, Remote Sensing and Spatial Information Sciences, Beijing, China. Vol. XXXVI, Part 3: 12-18.

Koenderink, J.J., 1984. The structure of images.Biological Cybernetics, 50: 363-393.

Kraus, K. 2004. Photogrammetry: Geometry from Images and Laser Scans, Second Edition, Walter de Gruyter, Berlin, Publishers.

Läbe, T., 1999. Contribution to OEEPE-test on automatic orientationof aerial images, Task A- Experiences with AMOR, EuropeanOrganization for Experimental Photogrammetric Research,Vol. 36:119–126.

Li, A.K.Y. and Batchvarova, T. 2008. Topographic mapping and terrain modeling from multi-sensor satellite imagery, International Archives of Photogrammetry, Remote Sensing and Spatial Information Sciences, Beijing, China. Vol. XXXVI, Part 1: 809-814..

Lindeberg, T., 1994. Scale-space theory: A basic tool for analysing structures at different scales. Journal of Applied Statistics, 21(2): 224-270.

Lowe, D.G., 1999. Object recognition from local scale-invariant features. In International Conference on Computer Vision, Corfu, Greece, pp. 1150-1157.

Lowe, D.G., 2004. Distinctive image features from scale-invariant keypoints. International Journal of Computer Vision, 60, 2: 91-110.

Michaelis, P. and Dowman, I., 2004. A rigorous model and DEM generation forSPOT5/HRS.International Archives of Photogrammetry, Remote Sensing and Spatial Information Sciences,35 (Part B1): 410-415.

Mikhail, E.M., Bethel, J.S. and McGlone, J.C., 2001. Introduction to Modern Photogrammetry, John Wiley & Sons, Inc., Publishers, New York, USA.

Misra, P. and Enge, P. 2001. Global Positioning System: Signals, Measurements and Performance. Gunga-Jamuna

Press, Massachusetts, Publishers: 152.

Neubeck, A. and Van Cool, L. 2006. Efficient non-maximum suppression.Proceedings of the 18th International Conference on Pattern Recognition (ICPR-2006):850-855.

OGC, 2004.The OpenGIS abstract specification Topic 7: the Earth imagery case v5.OpenGIS Project Document Number 04-107, Wayland, MA. 93 pages

Oh, Jaehong, C. K. Toth and D. A. Grejner- Brzeinska, 2010, Automatic Geo-referencing of Aerial images using High-resolution Stereo Satellite Images, ASPRS 2010 Annual Conference, San Diego, CA, April 26-30

Okamoto, A., 1992. Space triangulation using affine transformation.International Archives of the Photogrammetry and Remote Sensing, 29 (Part B3): 346-349.

Okamoto, A., Ono, T., Akamatsu, S., Fraser, C.S., Hattori, S. and Hasegawa, H., 1999.Geometric characteristics of alternative triangulation models for satellite imagery.Proceedings of ASPRS Annual Conference, Oregon, USA, 17-21 May.

Pedersen, B.1999. Contribution to OEEPE-test on automatic orientationof aerial images, Task A- Solution from Alborg, EuropeanOrganization for Experimental Photogrammetric Research,Vol. 36:139–144.

Petri, G., 1999: High Resolution Space Imagery, Survey Ireland.

Petrie, G., 2001. The future direction of the SPOT programme.Geoinformatics, pp. 28-31.

Pohl, C. and Van Genederen, J.L., 1998. Multisensor image fusion in remote sensing: concepts, methods and applications. Int. Journal Remote Sensing, Vol. 19, No. 5: 823- 854.

Radhadevi, P.V., Ramachandran, R. and Murali Mohan, A.S.R.K.V., 1998. Restitution of IRS-1C PAN data using an orbit attitude model and minimum control.ISPRS Journal of Photogrammetry and Remote Sensing, 53: 262-271.

Rosnell, T., Honkavaara, E. and Nurminen, K., 2011. On geometric processing of multi-temporal image data collected by light UAV systems. International Archives of the Photogrammetry, Remote Sensing and Spatial Information Sciences, Vol. XXXVIII-1/C22, (Commission I, WG I/V), UAV-g 2011, Conference on Unmanned Aerial Vehicle in Geomatics, Zurich, Switzerland.

Schenk, T., 1999.Digital Photogrammetry, Vol. 1, TerraScience, Publishers, Laurelville, USA.

Seeber, G., 1993. Satellite Geodesy: Foundations, Methods and Applications, Walter de Gruyter, Publishers, Berlin, Germany.

Shen, S.S., 1990. Multisource Data Integration in Remote Sensing, Proceedings of Workshop, Maryland, NASA Conference Publication 3099, pp. 145-149.

Simard, P., Bottou, L., Haffner, P. And LeCun, Y., 1998. Boxlets: A fast convolution algorithm for signal processing and neural networks. In Neural Information Processing Systems, AT&T Labs Research Report, Red Bank, USA .

Tao, V. and Hu, Y., 2002.3D reconstruction methods based on the rational function model. Photogrammetric Engineering and Remote Sensing, 68 (7): 705-714.

Tao, C.V., Hu, Y. and Jiang, W., 2004.Photogrammetric exploitation of IKONOS imageryfor mapping applications.International Journal of Remote Sensing, 25(14): 2833-2853.

Toutin, T. and Cheng, P., 2002.QuickBird - a milestone for high resolution mapping.Earth Observation Magazine, 11 (4):

14-18.

Tung, C.H. 2005. Updating topographic map using SPOT 5 satellite imagery.Proceedings of the Asian Conference on Remote Sensing (ACRS), Hanoi, 46: 133-139.

Viola, P.A. and Jones, M.J. 2001.Rapid object detection using a boosted cascade of simple features.In Conference on Comuter Vision and Pattern Recognition (CVPR) 2001: 511-518.

Wang, Y., 1999. Automated triangulation of linear scanner imagery.Proceedings of JointISPRS Workshop (WG I/1, I/3, IV/4) 'Sensors and mapping from space 1999',Hannover, Germany, 27-30 September.

Weser, T., Rottensteiner, F., Willneff, J., Poon, J. and Fraser, C., 2008. Development and testing of a generic sensor model for high-resolution satellite imagery. Photogrammetric Record, Vol. 21, No. 123, pp. 255-274.

Witkin, A.P., 1983. Scale-space filtering.In International Joint Conference on Artificial Intelligence, Karlsruhe, Germany, pp. 1019-1022.

Wolf, P. and B. Dewitt, 2000. Elements of Photogrammetry with Applications in GIS, Third Edition, , McGraw-Hill, Publishers, New York: 234.

Yamakawa, T. and Fraser, C.S., 2004. The affine projection model for sensor orientation:experiences with high-resolution satellite imagery. International Archives of Photogrammetry and Remote Sensing, 35 (Part B1): 142-147.

Yang, X., 2000.Accuracy of rational funciton approximation in photogrammetry.Proceedings of ASPRS Annual Convention, Washington DC, USA, 22-26 May.

Yang,Y., 2001. Piece-wise linear rational function approximation in digital photogrammetry.Proceedings of ASPRS Annual Conference, St Louis, USA, 23-27 April.

Yuille, A.L. and Poggio, T.A., 1986. Scaling Theorem for Zero Crossings.IEEE Transactions on Pattern Analysis and Machine Intelligence, Vol. PAMI-8, No.1: 15-25.

Zhang, C. and Fraser, C.S., 2012. Interior orientation error modelling and correction for precise georeferencing of satellite imagery.International Archives of Photogrammetry and Remote Sensing, Vol. XXXIX-B1: 285-290.

List of Figures

List of Tables

Acknowledgements

First of all, I would like to express my great appreciation to the Government of the Kingdom of Saudi Arabia, represented by Ministry of Municipal and Rural Affairs (MOMRA) for giving me this opportunity to continue my higher education.

I would like to offer the sincerest gratitude to my supervisor, Professor Christian Heipke, for the guidance, useful comments, remarks and engagement through the learning process of this thesis. A special gratitude I give to Professor Gottfried Konecny, whose suggestions and encouragement motivated me to initiate this research.

I am very grateful to my family, especially my mother, wife and children for the moral support and great patience. Last but not the least; thanks to my colleagues at MOMRA and everyone who had supported me throughout the entire process of investigation and developments leading to this thesis.

Muhamad Nasir A. ALRAJHI

Curriculum vitae

Last name, First name:	ALRAJHI Muhamad Nasir A.
Birth Date:	08 December 1961
Birth Place:	Al Bukayriyah, Saudi Arabia
Nationality:	Saudi Arabian
Marital Status:	Married
Position:	Assistant Deputy Minister for Land and Surveying Ministry of Municipal and Rural Affairs, SAUDI ARABIA

Education Details

- 1985: Bachelor of Science in Civil Engineering, Faculty of Engineering, King Saud University, Riyadh, Saudi Arabia.
- 2008: Master of Science in Gemoetics Engineering, Faculty of Civil Engineering, Kaltur University, Istanbul, Turkey

After graduating, worked for the General Directorate of Surveying and Mapping (GDSM) under the Ministry of Municipal and Rural Affairs (MOMRA), Kingdom of Saudi Arabia and provided professional services, and assumed the responsibility for technical and administrative management of large scale projects to fulfill the need for Aerial Photography, Large Scale Digital Photogrammetric Mapping, Municipal Surveying activities, Multipurpose Cadaster Registration as well as Development of Geographic Information System in MOMRA in support of regional and urban planning activities. Steered the General Directorate of Surveying and Mapping as Director General for over 15 years during which state-of-the-art geomatic technologies were successfully implemented, which culminated in the ISO certification and has made GDSM an eminent civilian survey authority of the Kingdom.

Currently serving as the Assistant Deputy Minister for Land and Surveying in MOMRA with administrative and executive responsibilities and playing key role in modernization and updating of the Geospatial Information Infrastructure.

Member of the Advisory Committee of the Department of Civil Engineering, King Saud University, Saudi Arabia, and also member of several Professional Organizations including AGU, FIG, ISO TC211, ASPRS, ISPRS, EAGE, European Academy of Sciences and Saudi GIS National Committee.

Wissenschaftliche Arbeiten der Fachrichtung Geodäsie und Geoinformatik der Leibniz Universität Hannover

(Eine vollständige Liste der Wiss. Arb. ist beim Geodätischen Institut, Nienburger Str. 1, 30167 Hannover erhältlich.)

Nr. 280	KOCH, Christian:	Extraction of Mercury's tidal signal and libration amplitude from synthetic laser altimeter data sets (Diss. 2009)
Nr. 281	GITLEIN, Olga:	Absolutgravimetrische Bestimmung der Fennoskandischen Landhebung mit dem FG5-220 (Diss. 2009)
Nr. 282	ELING, Dirk:	Terrestrisches Laserscanning für die Bauwerksüberwachung (Diss. 2009)
Nr. 283	DOLD, Christoph:	Ebenenbasierte Verfahren für die automatische Registrierung terrestrischer Laserscans (Diss. 2010)
Nr. 284	RIPPERDA, Nora:	Rekonstruktion von Fassadenstrukturen mittels formaler Grammatiken und Reversible Jump Markov Chain Monte Carlo Sampling (Diss. 2010)
Nr. 285	KATTERFELD Christiane:	Interoperables Geodaten-basiertes E-Learning (Diss. 2010)
Nr. 286	JARECKI, Focke:	Spurkreuzungspunktdifferenzen zur Validierung satellitengradiometrischer Messungen (Diss. 2010)
Nr. 287	SCHRAMM, Matthias:	Unüberwachte lineare spektrale Entmischung mit Anwendungen für Baumdichteabschätzungen in semiariden Regionen Afrikas (Diss. 2010)
Nr. 288	ALSAYEL, Mohammed Y.:	Towards Standardizing International Boundary Determination and Quality Consequences on surveying and Mapping (Diss. 2010)
Nr. 289	TAVAKKOLI S., Seyed Mohammad:	Multi-Temporal Classification of Crops Using ENVISAT ASAR Data (Diss. 2011)
Nr. 290	VENNEGEERTS, Harald:	Objektraumgestützte kinematische Georeferenzierung für Mobile-Mapping-Systeme (Diss. 2011)
Nr. 291	BULATOV, Dimitri:	Textured 3D reconstruction of urban terrain from UAV-borne video sequences (Diss. 2011)
Nr. 292	GROTE, Anne:	Automatic road network extraction in suburban areas from aerial images (Diss. 2011)
Nr. 293	ALOBEID, Abdalla:	Assessment of Matching Algorithms for Urban DSM Generation from Very High Resolution Satellite Stereo Images (Diss. 2011)
Nr. 294	FANG, Xing:	Weighted Total Least Squares Solutions for Applications in Geodesy (Diss. 2011)
Nr. 295	WEGNER, Jan Dirk:	Detection and height estimation of buildings from SAR and optical images using conditional random fields (Diss. 2011)
Nr. 296	GÖPFERT, Jens :	Snakes for Adapting GIS Road and River Objects to Airborne Laser Scanning Data (Diss. 2011)
Nr. 297	MUHLE, Daniel:	Gegenseitige Orientierung von Mehrkamerasystemen mit nicht überlappendem Sichtfeld (Diss. 2011)
Nr. 298	SIRIBA, David Nyangau:	Conflation of Provisional Cadastral and Topographical Datasets (Diss. 2012)
Nr. 299	HELMHOLZ, Petra:	Verifikation von Ackerland- und Grünlandobjekten eines topographischen Datensatzes mit monotemporalen Bildern (Diss. 2012)
Nr. 300	DENG, Zhiguo:	GPS Meteorology with Single Frequency Receivers (Diss. 2012)
Nr. 301	ZEIßLER, Maik:	Zur Ermittlung von Bodenrichtwerten bei fehlenden Kaufpreisen unbebauter Grundstücke (Diss. 2012)
Nr. 302	PAFFENHOLZ, Jens-André:	Direct geo-referencing of 3D point clouds with 3D positioning sensors (Diss. 2012)
Nr. 303	WEINBACH, Ulrich:	Feasibility and impact of receiver clock modeling in precise GPS data analysis (Diss. 2012)
Nr. 304	HEIKER, Andrea:	Mutual validation of Earth orientation parameters, geophysical excitation functions and second degree gravity field coefficients (Diss. 2012)
Nr. 305	VOIGT, Christian:	Astrogeodätische Lotabweichungen zur Validierung von Schwerefeldmodellen (Diss. 2013)
Nr. 306	THIELE: Antje:	3D Building Reconstruction From High Resolution Multi-Aspect Interferometric Synthetic Aperture RADAR Data
Nr. 307	ALRAJHI, Muhamad Nasir A	A Semi-Automated Procedure for Orthophto Generation from High Resolution Satellite Imagery

Die Arbeiten werden im Rahmen des wissenschaftlichen Schriftenaustausches verteilt und sind nicht im Buchhandel erhältlich.

Der Erwerb ist zu einem Stückpreis von € 25,00 bei den herausgebenden Instituten möglich.